

Clemson University

TigerPrints

All Dissertations

Dissertations

12-2022

Permanently-Installed Distributed Pressure Sensors for Downhole Applications

Xuran Zhu
xuranz@g.clemson.edu

Follow this and additional works at: https://tigerprints.clemson.edu/all_dissertations



Part of the [Electrical and Electronics Commons](#)

Recommended Citation

Zhu, Xuran, "Permanently-Installed Distributed Pressure Sensors for Downhole Applications" (2022). *All Dissertations*. 3202.

https://tigerprints.clemson.edu/all_dissertations/3202

This Dissertation is brought to you for free and open access by the Dissertations at TigerPrints. It has been accepted for inclusion in All Dissertations by an authorized administrator of TigerPrints. For more information, please contact kokeefe@clemson.edu.

PERMANENTLY-INSTALLED DISTRIBUTED PRESSURE SENSORS FOR
DOWNHOLE APPLICATIONS

A Dissertation
Presented to
the Graduate School of
Clemson University

In Partial Fulfillment
of the Requirements for the Degree
Doctor of Philosophy
Electrical Engineering

by
Xuran Zhu
December 2022

Accepted by:
Dr. Hai Xiao, Committee Chair
Dr. Fei Peng
Dr. Pingshan Wang
Dr. Lin Zhu

ABSTRACT

Technology advancements (e.g., hydraulic fracturing and horizontal drilling) to recover unconventional oil and gas (UOG) resources are critical in maintaining future U.S. oil and gas production levels. Permanently installed distributed downhole pressure sensors could monitor fracture propagation, assess the effectiveness of hydraulic fracturing, and optimize hydraulic fracturing placement so that overall UOG recovery efficiency can be increased. However, the harsh environment (high temperatures, high pressures, strong vibration, and presence of brine, mud, debris, hydrate, and various gases), the long data telemetry distance, and the requirements of reliability and service lifetime make the downhole monitoring a very challenging task. To combat these challenges, this thesis presents three sensing systems for downhole pressure monitoring.

First, A microwave-photonic low-coherence interferometry (MPLCI) system is proposed for optical fiber based distributed sensing. The system can be used to interrogate the intrinsic Fabry–Pérot interferometers (IFPIs) based distributed downhole pressure sensors. Assisted by an unbalanced Michelson interferometer (MI), a low-coherence laser source is used to interrogate IFPIs along with an optical fiber for a dark zone-free (or spatially continuous) distributed measurement. By combining the advantages of microwaves and photonics, the MPLCI system can synergistically achieve high sensitivity and high spatial resolution.

Second, to solve the packaging and drift problems in optical fiber sensors, an all-digital sensing method based on an electrical encoder is developed for downhole pressure monitoring. The key innovation of the all-digital sensor concept is the built-in nonelectric

analog-to-digital converter (ADC), which eliminates the need for downhole electronics for signal conditioning and telemetry in conventional electrical downhole sensors. As such, the sensors are more robust, less expensive, and have less drift in comparison with the existing sensors. Because the sensor outputs are digital in nature, the developed sensors can be remotely logged over a long distance, and many sensors can be digitally multiplexed for distributed sensing using a single surface instrument. The all-digital pressure sensors and their surface instrument were designed, engineered, fabricated, and calibrated. The integrated sensing system was tested/validated at both laboratory and research wellbores.

Third, to solve the hysteresis problem induced by the electrical encoder, a non-contact optical encoder based all-digital pressure sensor for downhole applications is proposed. The proposed sensor combines the advantages of both optical fiber and all-digital sensing method. The noncontact-type encoder, which is composed of an encoding pad and an all-glass optical fiber sensing head. A glass additive and subtractive manufacturing (ASM) system was used to embed the multi-channel optical fibers into a bulk-fused silica glass substrate with high positioning accuracy and good thermal stability even at elevated temperatures. The optical fiber only serves as the telemetry channel to directly transmit the data in digital format, such that the system has long-distance telemetry capability as well as low drift. The proposed pressure sensor was manufactured and experimentally verified to have a high SNR, linear pressure response, and good long-term stability. In addition, a mathematical model to study the relationships between the sensor's performances and design parameters was established.

DEDICATION

This dissertation is dedicated to my family.

ACKNOWLEDGMENTS

I would like to express my deepest appreciation to my advisor Dr. Hai Xiao, who has sincerely treated me well and made himself as an example of how to be a better person, how to do valuable research, and how to efficiently present your works. I also want to thank my academic committee members, Dr. Fei Peng, Dr. Pingshan Wang and Dr. Lin Zhu, to provide guidance on my dissertation and my research. Thanks to all my peers and friends, Dr. Liwei Hua, Dr. Qi Zhang, Yongji Wu, Dr. Yizhen Chen, Dr. Jincheng Lei, Dr. Jianan Tang, Xinyu Jiao, Ningxuan Wen, Jin Yang, Jacob Garland, Nicholas Tomlinson, Dock Houston, Dustin Gravley, Dr. Runar Nygaard, and Na Yuan for their helps in my research and daily life. Lastly, I would like to have special thanks to my parents, Liping Zhu and Xiaofang Chen, and my wife, Xiting Wang, for their endless love and companion.

TABLE OF CONTENTS

	Page
TITLE PAGE	i
ABSTRACT.....	ii
DEDICATION	iv
ACKNOWLEDGMENTS	v
LIST OF TABLES	viii
LIST OF FIGURES	ix
CHAPTER	
I. INTRODUCTION	1
Challenges of downhole pressure monitoring in UOG field.....	1
Existing techniques for downhole pressure sensing	9
Motivations and objectives	15
Organizations of the dissertation	17
II. MICROWAVE PHOTONICS INTERFEROMETRY (MPI) FOR DISTRIBUTED FIBER OPTIC SENSING.....	19
Introduction.....	19
Operational principle	22
Experiments	25
III. ALL-DIGITAL DOWNHOLE PRESSURE SENSOR BASED ON AN ELECTRICAL ENCODER.....	32
Introduction of all-digital sensing method.....	32
All-digital downhole pressure sensor design overview.....	36
Module developments	37
Laboratory test of the fully assembled downhole pressure sensor	78

Field test of downhole pressure sensor at research wellbore.....	81
IV. GLASS ADDITIVE AND SUBTRACTIVE MANUFACTURING OF A FIBER OPTIC ROTARY ENCODER FOR DOWNHOLE PRESSURE SENSING.....	86
Introduction.....	86
Operational principle	88
Sensor Manufacturing	91
Experiments	96
Discussion	100
V. CONCLUSION.....	106
Conclusion	106
Future work.....	107
Innovations and contributions.....	107
APPENDICES	110
A: Publication list	111
REFERENCES	113

LIST OF TABLES

Table		Page
1.1	Preferred downhole pressure sensor specifications	9
4.1	Processing parameters for additive and subtractive manufacturing	92

LIST OF FIGURES

Figure	Page
1.1 U.S. energy consumption by fuel [1].	1
1.2 Products made possible by oil and nature gas [2].	2
1.3 Conventional and unconventional oil and gas productions [4].	3
1.4 Horizontal drilling and hydraulic fracturing used in UOG productions.	4
1.5 Downhole pressure gauge from Schlumbergers.	10
1.6 Downhole pressure gauge from Quartzdyne.	11
1.7 Schematic of the (a) EFPI pressure sensor and (b) its multiplexing with FBG for temperature compensation [31].	13
1.8 Schematic of FBG based downhole pressure sensor [32].	13
1.9 (a) cross-section view of the PCF. (b) Sagnac interferometer was used to interrogate the PCF pressure sensor. (c) Testing results at different pressure [33].	15
2.1 Schematic of the MPLCI system. Lc, coherent length of the light; BPF, bandpass filter; PC, polarization controller; EOM, Electro-optic modulator; EDFA, Erbium-doped fiber amplifier; PD, photodetector; VNA, vector network analyzer.	22
2.2 (a) Experiment setup of quantitative strain measurement and the reconstructed time-domain signal with an applied strain of $0.565 \mu\epsilon$. (b) The normalized peak intensities of ten pulses were extracted with respect to the applied strains.	26

List of Figures (Continued)

Figure		Page
2.3	(a) Experiment setup of cantilever beam distributed strain measurement. (b) Measurement (black dots) and theoretical simulation (colored mesh grid) results of strains along the cantilever beam with respect to the vertical deflection and axial location. (c) Zoomed-in view of the data from the first sensor (located at the range from 1 cm to 11 cm), in which orange line is the line fitting results of the measure strain data (blue dots).....	28
3.1	Comparison between the existing approach and all-digital sensing method for downhole monitoring.	33
3.2	Principle of the all-digital downhole pressure sensor.	34
3.3	3D design model of the all-digital pressure sensor.	36
3.4	Different types of pressure transducer. (a) C-type (single coil) Bourdon tube. (b) Metal bellow tube. (c) Helical coil Bourdon tube.....	38
3.5	Test of the sensor resolution. (a) Picture of the experiment setup, (b) Rotation angle of the helical coil Bourdon tube at different applied pressures.	39
3.6	Long-term stability of the helical coil Bourdon tube. (a) Pictures of the experiment setup. (b) Test results indicate that the drift is well within $\pm 1\%$ over the duration of 410 hours.	40
3.7	Picture of the coil at (a) 0 psi and (b) 6000 psi. No cross-section shape deformation at the transition section. No abnormal bending at 6000 psi.....	42
3.8	Test results of third version of Bourdon tube.	42
3.9	Two types of Bourdon tubes with four coils (a) and three coils (b). (c) Top view. A set screw was used to seal off the tube. (d) Cross section view.....	43

List of Figures (Continued)

Figure	Page
3.10 Solidworks models of (a) the housing, (b) the gear box, and (c) the connection between the Bourdon tube and the gear box.	44
3.11 3D plots of the housing and shaft in Design I . The housing and shaft are made of stainless steel. The overall length of the sensor is 137 mm. The upper part of the housing is used for fixing the eight pads. The zoom-in view shows the temporary and permanent fixing points. The rectangular notches on the walls are used for alignment. The lower part of the housing is used to provide additional support to the shaft. The two bearings prevent the shaft from swaying. The shaft will be connected with the pressure transducer. The eight rectangular slots on the shaft are used to fix the pin holders.	47
3.12 3D plots of the digital encoding pad and pad holder in Design I . The pad is made by a ceramic printed circuit board (PCB). The pad holder is made of stainless steel. The pad is assembled by pushing and sliding into the two notches of the pad holder (shown in the zoom-in view). The outlet of the notch will be then filled by high temperature epoxy. The assembled pad is shown in the right of the figure. The two holes on the pad are the signal and ground ports.	48
3.13 (a) the top view of pin holder and (b) bottom view of the pin holder assembled with the pin. The three small cylinders on the pin holder are used to locate and weld the pin.	49
3.14 3D models of the all-digital sensor after assembly. (a) Detailed view of housing and pad holder. (b) Detailed view of shaft and pin holder. (c) Dimension comparison between the sensor and a baseball.	50

List of Figures (Continued)

Figure	Page
3.15 CAD design file of digital encoding pad from bit 1 to bit 8. The encoding region occupies 300 degrees. The shadowed area is the conductor.	51
3.16 The relationship between pad and pin. The pin contacts the pad in both the encoding region (signal region) and the ground region. When the pin is sliding through the surface of a pad, the digital states change between “1” (open circuit) and “0” (short circuit).	51
3.17 (a) 3D and (b) 2D design files of contacting pins. Three bending positions have been marked out using red dashed lines. The height of pins after bending influences the contacting force when the pin is assembled with the pad. The zoom-in view and cross-section views show the detailed design of the contacting points. There is a small bump at each contact points to decrease the contact area.	53
3.18 The pad and pad holder in Design II. The pad is composed of stainless steel and high-temperature epoxy or ceramic glue. A mold is required to shape the epoxy. The two protrusions on the top and bottom will be welded with the pad holder. Laser machining is then used to cut the connections (two red lines). The encoding region is on the pad, and the ground region is on the pad holder.	54
3.19 The assembled housing, lid, and shaft in Design III. The lid is assembled by the inner threads on the top of the housing. Two bearings are used to stabilize the shaft. The extended part of the housing in the previous designs has been deleted. The overall height of the sensor is 109 mm. The diameter remains the same as that of the previous designs.	56

List of Figures (Continued)

Figure	Page
3.20 (a) The ground pin is assembled within the notch of the housing and contacts with the shaft. The pad is assembled with the shaft by a rectangular plug. (b) The stacked relationships between pins and pads have changed. Signal wires are soldered with pins. The yellow area on the pin holder is the thermal isolation material, such as the ceramic. It is used to protect the pin holder from high temperatures during the soldering process.	57
3.21 3D model of pin holder. The main body of the pin holder is made of Teflon. The four screws are made of steel and assembled by the threads. As in Design I , the four screws will be used to connect the pin holder to the housing.....	57
3.22 3D model of fully assembled all-digital sensor from Design III. The rotation stage connected to the shaft is used for alignment of the pads and pins.....	58
3.23 (a) Encoding pad fabricated using stainless steel and high-temp epoxy FH8732. (b) The pad was tested at 250 °C for four hours then cooled down to room temperature. No cracks were found in the dried epoxy after the high temperature test.....	60
3.24 Pictures of fabricated (a) signal pin and (b) ground pin and.....	60
3.25 Microscope images of the contact pins before (a) and after (b) polishing.....	61
3.26 (a) A contact pin connected with an electrical wire using high-temperature solder and fixed on a Teflon plate by three screws. (b) Pins contacted their corresponding encoding pads.....	62
3.27 Experiment setup to test the digitizer.....	63
3.28 The dimension of the 8th-bit encoding pad.	64

List of Figures (Continued)

Figure	Page
3.29 Test results of the 8th-bit channel with a bias angle of (a) 0.3° and (b) 0.15°	65
3.30 (a) Test results of the 7th-bit channel. (b) Two extreme cases when the centers of pad and pin are not aligned. Opad is the rotation center of the pad, and Opin is the rotation center of the pin.	66
3.31 Calibration of the digitizer. (a) Picture of the experiment setup, (b) Digitizer outputs as a function of the rotation angle.	67
3.32 Long-term stability test of the digitizer. (a), (b) and (c) pictures of the test setup showing the digitizer placed inside an environmental chamber; (d) Contacting resistances between contact pins and encoding pads of the 8-bit digitizer as a function of time.	69
3.33 (a) Solidworks design model of the multiplexing module. (b) Fully assembled multiplexing module. (c) Details of the contacting pins. (d) Details of the encoding patterns. (e) Details of the milter gears and the ratcheting gear.	70
3.34 Wiring of downhole pressure sensors.	71
3.35 Working principle of multiplexing module.	73
3.36 Pictures of the inside (a) and outside (b) of the developed surface instrument to drive the multiplexing module.	73
3.37 Graphic user interface (GUI) of the control software.	75
3.38 Picture of five multiplexing modules interrogated by the portable instrument.	75
3.39 Circuit schematic of the surface sensor reading instrument.	76

List of Figures (Continued)

Figure	Page
3.40	Picture of the surface sensor reading instrument. 77
3.41	SNR test results of instrument. 77
3.42	Arc welding among beam, shaft, and the encoding pad. 78
3.43	The assembled downhole sensor..... 78
3.44	In-lab sensor test setup at OU. 79
3.45	(a) All-digital sensor assembled with housing and testing chamber lid. (b) Top view of the testing chamber..... 80
3.46	In-lab pressure testing results at different temperatures. 81
3.47	The all-digital sensor and reference sensor were connected to their cables. 81
3.48	(a) The all-digital sensor was attached to the suck rods by three band clamps. (b) and covered by waterproofed tape. (c) The reference sensor was attached to the suck rods by four band clamps and (d) covered by the waterproofed tape. (e) Two cables were fixed to the sucker rods using zip-ties. (f) A production tubing was placed on the last rod..... 83
3.49	Tubing cap with the cable pass through..... 83
3.50	Surface sensor reading instruments setup. 84
3.51	Testing data when all-digital sensor was lowering downhole..... 84

List of Figures (Continued)

Figure	Page
4.1 Operational principle of optical encoder based downhole pressure sensor. A Bourdon tube transduces the pressure to the rotation angle. The optical encoder transform the rotation angle into binary code. The black region on the encoding pad represents the low reflectivity region, while the white region has high reflectivity. Enlarged figure on the right: Optical path at fiber tip. The fiber end was polished to have an inclination angle of θ_1	89
4.2 Glass additive and subtractive manufacturing system.	91
4.3 Procedure of packaging the sensing fiber into a bulk fused silica glass.	92
4.4 SEM images of the polished cross-section viewed 3D printed all-glass fiber head. (a) Overview. (b) Connection between the substate and the glass paste. (c) interface between the dummy fiber and the sensing fiber.	94
4.5 Side view of the polished all-glass sensing head.	95
4.6 (a) Polished stainless-steel disc coded using picosecond laser. (b) SEM image of the blackened region.	96
4.7 SNR test results. The optical fiber sensor head was scanning through four evenly distributed blackened region.	97
4.8 (a) Assembled pressure sensor. (b) Alignment between the optical fiber head and the encoding pad. (c) Pressure response test results.	98
4.9 Pressure sensor test at 250°C for 400 hours.	99

List of Figures (Continued)

Figure	Page
4.10 (a) Schematic of the encoding pad. (b) Initial alignment state. The fiber tip (blue solid line) is aligned to the encoding pad at point A. (b) Testing state. When the fiber tip rotates to point B, a misalignment angle of ϕ_e is generated. Φ , angles of the full encoded region; $d\phi$, angles of a single bit; ri , inner radius of the encoding pad; ro , outer radius of the encoding pad; Wc , bit channel width; Wb , minimum arc length of a single bit; Of , rotation center and coordinate origin; Op , encoding pad center; θ , initial alignment angle between fiber head and encoding pad; ϕ , rotation angle; ef , the maximum misaligned distance at fiber tips; ep , the misaligned distance between the rotation center and encoding pad center.	101
4.11 Relationship between encoding pad outer radius, ro , and the number of encoded bits, n , at $(ep+ef)Se$ equals to 2 μm , 10 μm , 20 μm , and 40 μm	104

CHAPTER ONE

INTRODUCTION

1.1 Challenges of downhole pressure monitoring in UOG field

1.1.1 The importance of oil and gas industry

Oil and natural gas are major industries in the energy market and play an influential role in the global economy as the world's primary fuel sources. Based on the U.S. Energy Information Administration's (EIA's) 2021 annual energy outlook (Figure 1.1), petroleum and natural gas contributed to about 70% of total energy consumption in 2021. Although the renewable energy is growing fast, oil and nature gas will still be the most-consumed sources of energy in the United States through 2050.

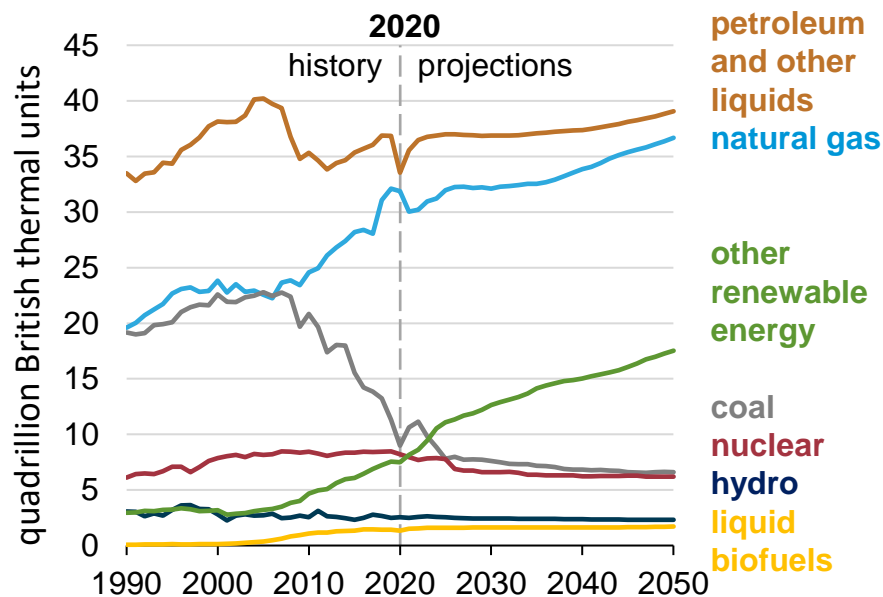


Figure 1.1 U.S. energy consumption by fuel [1].

In addition to be used as the fuel sources, byproducts from oil refining are also used in produce everyday products such as credit cards, toothpaste and eyeglasses.



Figure 1.2 Products made possible by oil and nature gas [2].

1.1.2 Unconventional oil and gas (UOG) production and downhole pressure sensing

The upstream segment, including exploration and production, is the one of the most important portions in the oil and gas industry. It requires state-of-the-art technologies to increasing productivity and suppressing the cost. Based on the different types of source and production difficulties, the oil and nature gas can be categorized as conventional oil and gas (COG) and unconventional oil and gas (UOG). Conventional oil is a category that includes crude oil and natural gas and its condensates. Unconventional oil consists of a wider variety of liquid sources including oil sands, extra heavy oil, gas to liquids and other liquids. In general, conventional oil is easier and cheaper to produce than unconventional oil [3]. Figure 1.3 is a conceptual illustration of different types of oil and gas wells. A vertical well is producing from a conventional oil and gas deposit

(right). Also shown are wells producing from unconventional formations: a vertical coalbed methane well (second from right); a horizontal well producing from a shale formation (center); and a well producing from a tight sand formation (left).

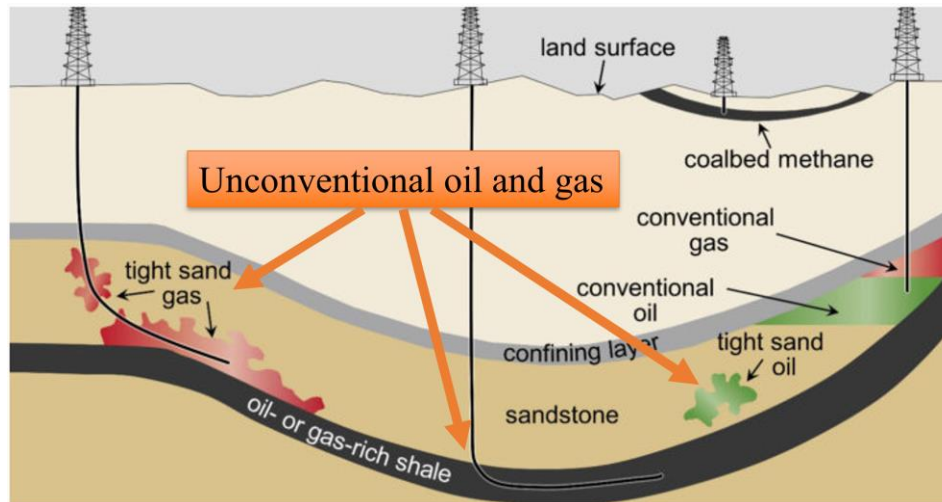


Figure 1.3 Conventional and unconventional oil and gas productions [4].

Industry and governments across the globe are investing in UOG sources due to the increasing scarcity of COG reserves. Based on the EIA's 2021 Annual Energy Outlook, UOG resources are projected to contribute 64.5% (73.7%) of total U.S. oil production and 86.5% (92.3%) of total U.S. natural gas production in 2020 (estimated in 2050). Over the past decade, UOG development has dramatically increased US production of oil and natural gas. From 2007 to 2016, the U.S. production of crude oil increased dramatically by 75%, while natural gas production increased by 39% [5]. Such increases in both oil and natural gas production are primarily due to technological advancements in extended-lateral horizontal drilling and multistage high-volume hydraulic fracturing [6].

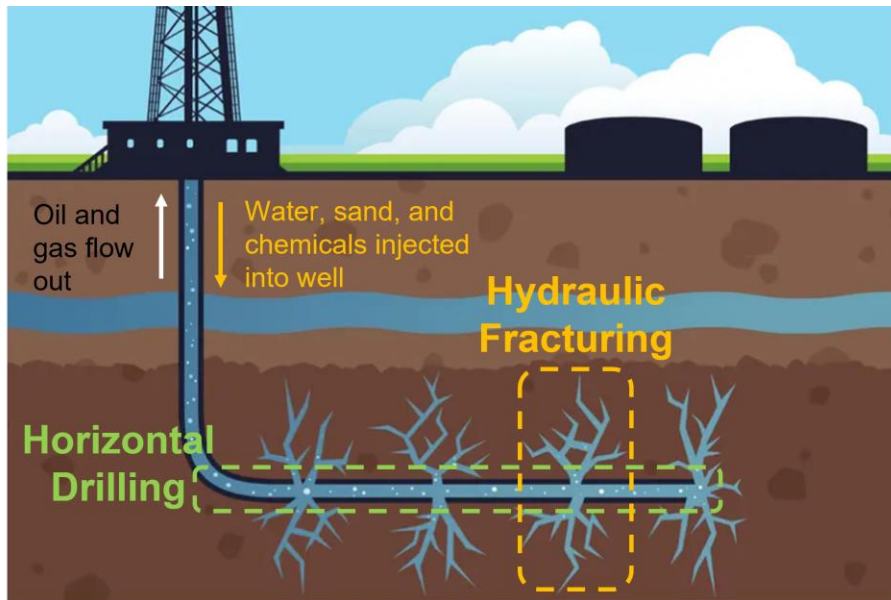


Figure 1.4 Horizontal drilling and hydraulic fracturing used in UOG productions.

Figure 1.4 demonstrate the horizontal drilling and hydraulic fracturing used in UOG productions. Horizontal drilling is a horizontal or angled deviation from the vertical section of a wellbore. When a well has been drilled to the depth of the targeted oil or gas reservoir, hole curvature is developed to access the zone of interest [7]. Horizontal wells are designed to drastically increase production by establishing better contact with the productive layer of a reservoir [7]. Hydraulic fracturing is the process of injecting millions of gallons of water, proppant (e.g., granules of sand, ceramic, etc.), and chemicals at high pressure into a formation to create fractures and produce hydrocarbons [7]. During fracturing, the proppant fills the fractures to keep them from resealing, which allows the hydrocarbons to flow into the wellbore and be produced [7].

1.1.3 Importance of downhole pressure sensing

UOG developments are extremely cost sensitive and marginally economical in many instances. The recovery efficiency of UOG is despairingly low, perhaps 20% in gas-rich shale reservoirs and less than 10% in liquid-rich plays [8]. Due to the lack of knowledge, information, technological and economical limitations, the full potential of US UOG resources has yet to be realized. Technology advancements to recover UOG resources are critical in maintaining future US oil and gas production levels.

One of the uncertainties in all hydraulic fracturing operations is determining where hydraulic fracture placement along the wellbore should be located, if the fractures should space evenly or focus in target zones with special geological and geomechanical characteristics, for instance, the zone with a certain log reading interval or a certain brittleness index [9]–[11]. Permanently-installed distributed downhole pressure sensors would provide valuable information on fracture propagation and assessment of the overall effectiveness hydraulic fracturing [12]–[14]. Having the ability to measure the pressure at each fracture stage along the wellbore can provide invaluable information to increase the effectiveness of a fracture. Besides, the continuous downhole pressure measurement will also enable the big data analytics and machine learning applications to inform decision making and improve the ultimate recovery of UOG [15], [16], such as to locate the areas where less production has occurred and to identify the potential re-fracturing targets.

Besides being used in UOG field, the downhole pressure monitoring is also very important in geothermal applications (e.g., the enhanced geothermal system (EGS)). The

EGS concept is to extract heat by creating a subsurface fracture system to which water can be added through injection wells. Rocks are permeable due to minute fractures and pore spaces between mineral grains. Injected water is heated by contact with the rock and returns to the surface through production wells. The heated water can be then used for electricity productions. Pressure information is necessary to generate a full geophysical map to improve operation efficiency and increase well lifetime [17].

1.1.4 Challenges faced by downhole pressure sensing

Permanently installed distributed pressure monitoring in the downhole environment is critical for improving ultimate recovery of UOG, however, the downhole environment poses great challenges to the development of low-cost viable distributed pressure sensing technologies. These technological and economical challenges have prevented the wide use of distributed pressure monitoring in downhole for UOG recoveries. The signals produced by current pressure transducers are analog in nature and very weak. As a result, the signal needs to be conditioned (e.g., amplified, filtered, modulated, processed) and/or digitized using downhole electronics before the signal can be transmitted over a long distance to the surface. The downhole electronics present some major issues to the performance and cost, including

1. Drift of electronic pressure sensors: The sources of drift in the pressure sensors include (1) the transducer shift, (2) the circuit drift, and (3) the drift of the mechanical structure. In general, the mechanical drift is negligible because of the matured materials, processes and practices in design, material/component selection and construction. The transducer and circuits drifts are the major contributions. The drift of the quartz resonator

pressure sensor is typically smaller than that of the piezoresistive pressure sensor, because a reference quartz is usually co-packaged with the quartz sensor for compensation. Si-based integrated circuits are rated 125°C for military applications, and SiC-based high temperature electronics are pushing towards 250°C. There is limited availability of high temperature rated components from semiconductor manufacturers [18], [19], and their performance (e.g., drift and noise level), especially for the analog functions such as amplification and filtering, degrades/drifts as the temperature increases.

2. Complicated data telemetry: Even with downhole signal conditioning electronics, the signals generated by the pressure sensors need to be transmitted from downhole to the surface using specialized telemetry, such as the mud pulse telemetry, the vibration wave transmission through tubing or casing, and the carrier or load modulation based wire/cable communication [20]–[22]. These specialized telemetry techniques are complicated, expensive and affordable only to high productivity wells.

3. Lack of multiplexing capability: In current configurations, each pressure sensor requires not only on-spot electronics but also a close-by telemetry unit for data transmission. Neither can they be conveniently multiplexed (e.g., connected in series using a single cable) nor flexibly deployed for distributed monitoring.

4. High cost of existing pressure monitoring: A typical dual pressure and temperature gauge used for oil and gas operations costs approximately \$10,000 - \$20,000 (not counting the expensive data telemetry system), because of the high-end electronics and rigorous packaging required, and the long well-protected signal transmission lines [23]. If multiple pressure sensors are used (thus, multiple telemetry units and multiple

cables are needed) to map the pressure distribution along the wellbore, the system cost quickly becomes prohibitive for UOG developments.

Fiber optic pressure sensors are getting attractions due to its passive nature (thus no downhole electronics and data telemetry is needed). However, their long-term reliability, stability and survivability are yet to be proven in downhole, especially when considering the strong vibrations and heavy mechanical stresses caused by hydraulic fracturing, and they are often too costly to be widely deployed in UOG fields.

1.1.5 Downhole pressure sensor requirements in UOG fields

Downhole monitoring has been one of the most challenging tasks faced by the sensor research and development community. The challenges are largely imposed by the harsh conditions in the reservoir and along the borehole (e.g., high temperatures, high pressures, strong vibration, and presence of brine, mud, debris, hydrate and various gases), the long distance of data transmission to the surface, and the required reliability and long service lifetime.

Based on information obtained from literatures and datasets [24], an estimated sensor specifications that are applicable to a majority of unconventional shale formations is listed in Table 1.1. Here, I only provide a rough range of sensor's performance requirements in UOG fields. The specific requirements may vary for different shale formations and for different applications. For example, the geothermal reservoirs may require the measurement temperatures up to 550-600 °C at depth of 4-5 km [25].

Table 1.1 Preferred downhole pressure sensor specifications in UOG fields.

Pressure	10,000-35,000 psi
Operating temperature	150-250°C
Long term pressure stability	0.2% Full Scale/year
Multiplexing capability	10 multiplexed sensors
Max sensing distance	20 km
Dimensions diameter	2 in.
Cost	<\$100/node

1.2 Existing techniques for downhole pressure sensing

Two general types of sensing technologies have been extensively researched, including the discrete electronic sensors and the distributed fiber optic sensors.

1.2.1 Electronics downhole pressure sensor

The two most popular electronic sensors are the piezoresistive and piezoelectric pressure transducers. The piezoresistive transducer operates based on the mechanical stress induced electrical resistance change of a material, typically silicon on insulator (SOI) [26]–[28]. The resistance change is commonly measured by an active Whinstone resistive bridge and an on-spot amplifier. The piezoelectric pressure sensor (quartz sensor) is based on the principle of pressure induced resonance frequency changes, which also needs an on-spot circuit to boost the signal level [29], [30]. The typical structure is a thick-walled hollow cylinder with closed ends. A thickness-shear-mode disc resonator divides the central portion of the hollow cylinder. Fluid pressure on the exterior hydrostatically compresses the quartz cylinder, producing internal compressive stress in the resonator. The vibrating frequency of the sensor changes in response to this stress.

Some commercially available downhole electrical pressure sensors are listed below. As shown in Figure 1.5, The Metris Extreme HPHT permanent PT gauge from Schlumbergers Inc. has a measurement temperature of up to 400°F and a measurement pressure of up to 30,000 psi. Figure 1.6 shows the quartz pressure transducer for downhole applications from Quartzdyne. It has a pressure range of 0 - 35,000 psi and an operating temperature range of -40° to 225°C. The standard MWD system from Compass Directoinal Guidance Inc. has an operating temperature of up to 175°C and a measurement pressure of up to 20,000 psi.



Figure 1.5 Downhole pressure gauge from Schlumbergers.

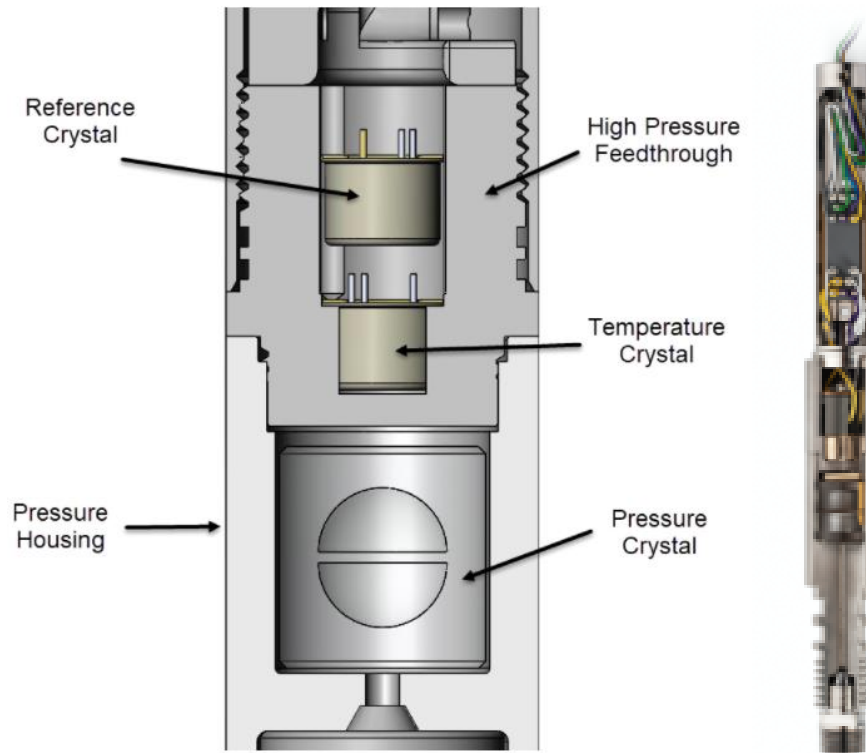


Figure 1.6 Downhole pressure gauge from Quartzdyne.

The commercially available electronic sensor typically includes four functional elements: transducer, signal conditioning circuit and data telemetry unit, signal transmission cable, and surface electronics. The transducer signal is intrinsically weak and analog in nature, and it cannot be directly transmitted over the long noisy cable. An on-spot circuit must be used to amplify/condition/digitize the transducer signal in order to transmit the signal to the surface. However, the added circuits (e.g., A/D convertor and pre-amplifier) in the downhole conditions degrades over time at high operating temperature. As such, the existing electronic pressure sensors need to overcome two major challenges, which are the drift over time at high temperatures and the high cost associated with the hermetic package and data transmission.

1.2.2 Fiber optic downhole pressure sensor

The fiber optic sensor has many unique features, including high sensitivity, high operating temperature (passive operation so that it does not need downhole electronics), high operating pressure, small size and light weight, long reaching distance (low loss), capable of multiplexed operation, and EMI immunity. These features make the fiber optic sensor a competitive candidate for downhole sensing. And extensive studies have been conducted to develop the fiber optic downhole sensors.

The most popular configuration of fiber optic downhole sensors involves the use of various time-domain techniques to realize truly distributed sensing [31]. Continuous temperature profile along the entire length of an optical fiber can be mapped with decent accuracy by several mechanisms including Rayleigh scattering, Raman scattering and Brillouin scattering [32]. These systems are commercially available for distributed temperature, strain and acoustic measurement in downhole. However, the commonly used fiber itself is sensitive to temperature and strain only so that fiber optic pressure measurements rely on discrete optical fiber components such as a Fabry-Perot interferometer (FPI) or a fiber Bragg grating (FGB). By attaching those optical fiber components to a pressure sensitive transducer, the strain changes measured by the optical fiber sensors can be mapped to the pressure information.

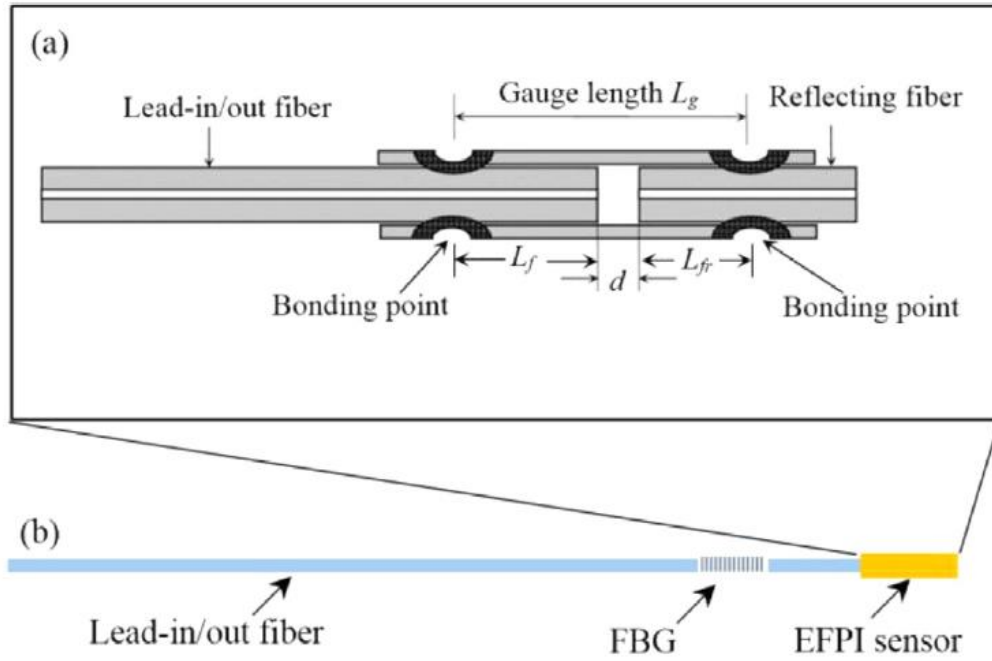


Figure 1.7 Schematic of the (a) EFPI pressure sensor and (b) its multiplexing with FBG for temperature compensation [33].

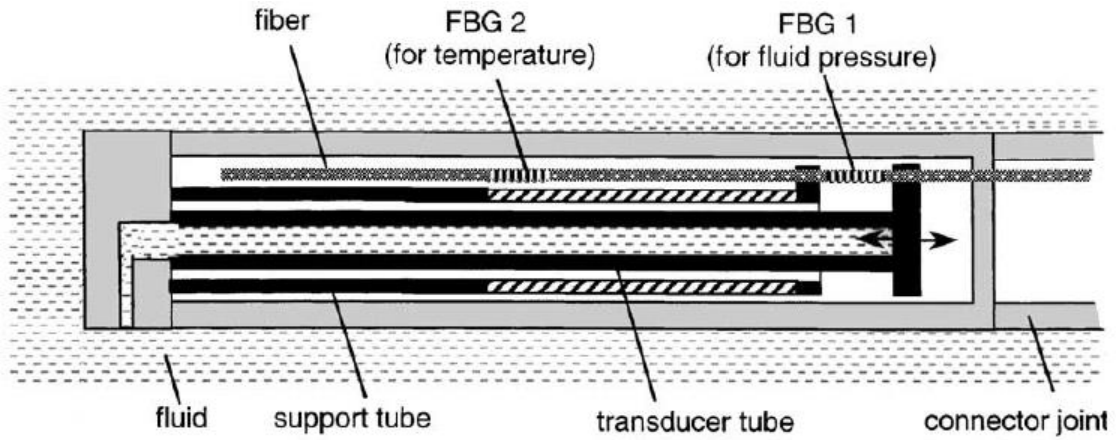


Figure 1.8 Schematic of FBG based downhole pressure sensor [34].

Xinlei et al. proposed an extrinsic FPI for downhole pressure sensing [33]. The schematic of the sensor is shown in Figure 1.7. As the pressure changes, the cavity length of the EFPI will change accordingly. So that the pressure information can be obtained by

demodulate the EFPI's cavity length. The EFPI was formed by inserting two fibers into a capillary tube. The fibers and the capillary tube were bonded with a CO₂ laser beam. The sensor was tested to have an accuracy of 0.05% full scale and a hysteresis of 0.01% full scale in the dynamic range of 72 Mpa. The highest testing temperature is about 280°C. The sensor has high accuracy and high operating temperature. However, it's difficult to multiplexing many EFPI sensors along one sensing fiber.

Figure 1.8 shows a schematic of FBG based downhole pressure sensor [34]. When the fluid pressure changes, the transducer tube will pull the FGB. By detecting the spectrum shift of the FBG, the fluid pressure can be measured. The proposed sensor has an accuracy of 0.04% FS, pressure measured up to 100 MPa, and an operating temperature of 230 °C. The FBG based pressure sensor can be configured as a discrete distributed sensing system.

In addition to PFI and FBG based pressure sensor, photonic crystal fiber (PCF) is another promising technique for downhole pressure sensing [35]–[37]. PCF sensor is less sensitive to the environmental temperature change compared to the PFI or FBG sensors. Besides, the PCF itself is pressure sensitive. So, it does not need to attach to mechanical pressure transducer. The working principle of the PCF sensor is based on measuring the changes of birefringence effects. The PCF has high birefringence effect, which means the refractive index of the two orthogonal polarization directions are different. As the outside pressure changes the shape of the fiber, the refractive index will also change. Typically, a Sagnac interferometer (SI) is used to detect the birefringence variations. Figure 1.9 shows an example of the PCF based pressure sensor [35]. The sensor has an accuracy of 0.002%

Full Scale, measurement pressure of up to 50 MPa, and measurement temperature of up to 250°C. However, the PCF sensor is hard to be multiplexed. And it is more expensive than the PFI or FBG based sensors.

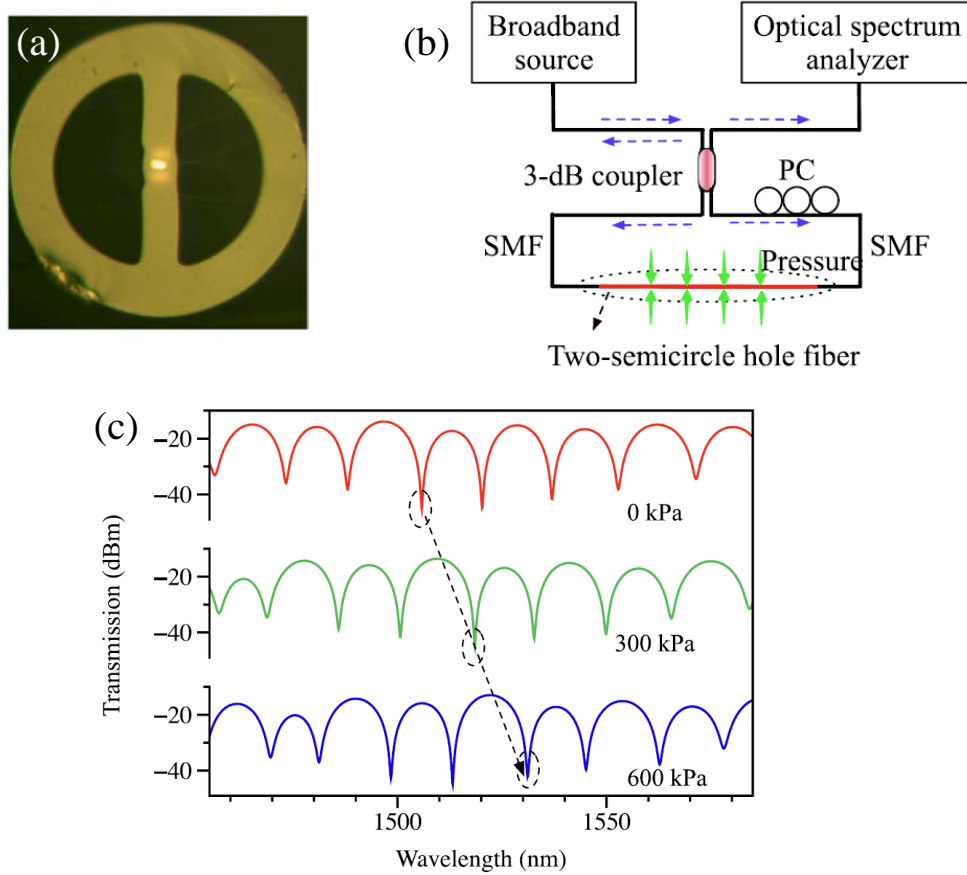


Figure 1.9 (a) cross-section view of the PCF. (b) Sagnac interferometer was used to interrogate the PCF pressure sensor. (c) Testing results at different pressure [35].

1.3 Motivations and Objectives

1.3.1 Motivations

Inspired by the configuration of FBG based downhole pressure sensor (as showing in Figure 1.8), intrinsic-FPI sensors attached to different pressure transducer can

be used for distributed downhole pressure monitoring. The IFPI sensor can be composed of broadband weak reflectors along the fiber, which makes it more cost efficient than the FBG sensors. Moreover, hundreds of weak reflectors can be fabricated along the sensing fiber to form a IFPI sensing arrays for long distance high density distributed sensing. However, conventional sensor interrogation systems (e.g., optical time domain reflectometry and optical frequency domain reflectometry) are not suitable to detect the distributed IFPI sensor array with small interval and long reaching distance. A new distributed sensor interrogation system will be developed based on microwave-photonic interferometry. The proposed system can achieve high sensitivity, high spatial resolution, and high sensing distance at the same time.

To solve the packaging and the long-term drift problems existed in the optical fiber sensing system, the all-digital sensing method based on an electrical encoder is proposed and developed for distributed downhole pressure sensing. Unlike the conventional electrical downhole sensors, the all-digital sensor does not have any downhole electronics (e.g., ADC, amplifier or data telemetry). It uses a mechanical digitizer to passively convert the physical quantities to binary digital states (e.g., electrical conductive and electrical nonconductive). Because the digital signal has higher signal to noise ratio compared to the analog signal, these digital states can be easily interrogated by the surface instrument over long distance.

One important challenge of the developing the electrical encoder is the hysteresis induced by the contact-type encoder. As a result, a non-contact-type optical encoder based all-digital sensing system is developed for downhole pressure sensing. This system

takes advantages of both optical fiber and all-digital sensing. A laser additive and subtractive manufacturing system is used to fabricate all glass optical fiber sensing head. The sensing head is used to detect the digital states of the pressure digitizer. Optical fiber only serves as the telemetry channel, but not the sensing unit. As such, the sensing distance of the downhole sensor is extended and the costly and heavy electrical cable is eliminated.

1.3.2 Objectives

The main objective of this thesis is to develop and validate new low-cost pressure sensing technologies for in situ distributed downhole pressure monitoring. The developed sensors should have high pressure measurement range, high working temperature, good vibration resistivity, low cost, small drift, long reading distance, compact size and can be multiplexed for distributed sensing using a single surface instrument. The specific objectives are:

- (1) Develop the microwave-photonic low-coherence interferometry (MPLCI) system to interrogate the densely distributed IFPI sensors over long distance with high sensitivity and high spatial resolution.
- (2) Develop the all-digital sensing method and validate the system based on an electrical encoder.
- (3) Develop an optical encoder based all-digital sensing system, which take advantages of both optical fiber and all-digital sensing method.

1.4 Organizations of the dissertation

This dissertation is organized into five chapters.

Chapter one: Technology advancements to recover UOG resources are critical in maintaining future U.S. oil and gas production levels. However, existing downhole pressure sensing systems can not fulfill the requirements of UOG pressure monitoring.

Chapter two: A microwave-photonic low-coherence interferometry (MPLCI) system is proposed for fully distributed optical fiber sensing. The proposed system can be used to interrogate the distributed IFPI sensors with high sensitivity, high spatial resolution and long reaching distance. The mathematic model is established, and demonstration experiments is conducted.

Chapter three: The principle of all-digital sensing will be first introduced. The design, fabrication, and testing of each individual modules inside the all-digital downhole pressure sensor will be described. These modules include the helical coil Bourdon tube, the gearbox, the digitizer, the multiplexing module, and the surface instrument. The fully assembled sensor will be tested at both laboratory and research wellbore environments to demonstrate the developed downhole sensing system.

Chapter four: A fiber optic rotary encoder-based pressure sensor for downhole applications is presented. The glass additive and subtractive manufacturing (ASM) techniques are used to embed the multi-channel optical fibers into a bulk-fused silica glass substrate. The experiment setup and testing results will be introduced. In addition, a mathematical model to study the relationships between the sensor's performances and fabrication requirements is established.

Chapter five: The major contributions of the thesis and the future work plan will be summarized.

CHAPTER TWO

MICROWAVE PHOTONICS INTERFEROMETRY (MPI) FOR DISTRIBUTED FIBER OPTIC SENSING

2.1 Introduction

Various distributed fiber sensing technologies have been studied to achieve the combined features of high spatial resolution, high measurement sensitivity, long-span coverage, and spatial continuity (i.e., dark zone free).

Optical time domain reflectometry (OTDR) is one of the most common configurations for distributed fiber sensing over a long-range. The measurement range of OTDR has been extended to 175 km with meter-level spatial resolution [38]. In general, high measurement resolution at meter level can be achieved by a phase-sensitive OTDR system that uses a coherent source. A strain resolution of 47.5 $\mu\epsilon$ at a spatial resolution of 2 m has been demonstrated via wavelength-scanning in a coherent OTDR [39]. However, the tradeoff between signal-to-noise ratio (SNR) and pulse width limits the spatial resolution of the OTDR based methods at meter level. Several methods have been proposed to improve the spatial resolution, such as pulse coding phase-OTDR [40] and phase-OTDR with frequency-swept pulse [41]. A photon-counting OTDR system was recently developed [42], which accomplished 15 dB dynamic range and centimeter-level resolution over a range of up to 12 km. However, the measurement time was increased to 20 minutes, and dark zones were embedded between consecutive monitoring sections because of the single-photon detector's afterpulse effect.

Optical frequency domain reflectometry (OFDR) is widely used for high spatial resolution monitoring of fiber links. For example, a 0.1 mm spatial resolution over a 200 m fiber has been achieved by phase-OFDR [43]. However, the measurement range of an OFDR system is typically restricted within several hundred meters because of the limited coherent length of the laser source. Numerous techniques have been proposed to overcome the restriction of the measurement range. In Ref. [44], a spatial resolution of 0.8 m and a strain resolution of $245.6 \text{ } \mu\epsilon/\sqrt{\text{Hz}}$ along a sensing fiber of 9.8 km were realized by time-gated digital OFDR. In Ref. [45], phase-OFDR with inner-pulse division and rotating-vector-sum were reported. A spatial resolution of 12 cm and a strain resolution of $1 \text{ } \mu\epsilon/\sqrt{\text{Hz}}$ was achieved at a measurement range of 960 m. Thus, it is still a great challenge to achieve centimeter-level spatial resolution over a kilometer-level measurement range with high sensitivity.

The microwave-photonic technique provides another perspective to solve the problem. In an incoherent OFDR (I-OFDR) system, a broadband laser, which is intensity-modulated by the microwave signal, is used to interrogate the fiber sensors. The sensors can be demultiplexed by scanning the frequency of the modulated signal. I-OFDR has the advantages of high spatial resolution, long measurement range, and high SNR [46]. Theoretically, a spatial resolution of 10 cm over the range of 5 km can be achieved with a microwave scanning range of 2 GHz and a scanning step of 20 kHz [47]. To achieve high sensitivity, I-OFDR has also been implemented to interrogate cascaded fiber Bragg gratings (FBGs) [48], [49], where a tunable laser was used to obtain the spectra of FBGs.

Discrete in-fiber reflectors have been used to construct in-fiber FPI arrays for fully distributed sensing [50]. These in-fiber FPIs have been interrogated using the incoherent optical carrier based microwave-photonic interferometry (MPI) technique to achieve long-range and high spatial resolution distributed sensing [51]. Later, a coherent-length-gated MPI technique was proposed to improve the sensitivity [52], [53]. By detecting the phase change through optical interference, nε-level sensitivity can be achieved. However, to discriminate the cascaded IFPIs and avoid the crosstalk among interferometers, dark zones (low-sensitivity regions) need to be inserted between adjacent IFPIs, and the coherent length of the laser source also needs to be carefully controlled, which increases the system complexity.

Low-coherence interferometry (LCI) is initially used for remote absolute distance measurement [54], in which a local receiving interferometer (LRI) is connected in-line with the remote sensing interferometer. The optical path difference (OPD) of the LRI (length difference between two arms of the interferometer) is adjusted to match that of the sensing interferometer within the coherence length of the laser source, such that the interference occurs at the output of the LRI. A local Michelson interferometer (MI) is utilized as the LRI to construct the MPLCI system, by which the dark zones along the sensing fiber are eliminated, and the requirement for laser source is also relieved.

Although the proposed system uses similar components as the I-OFDR system, such as a vector network analyzer (VNA) and an electro-optic modulator (EOM), there are fundamental differences between the I-OFDR and the MPLCI systems. Most importantly, the MPLCI system belongs to coherent sensing and operates based on

optical interferometry. The strain change is detected by resolving the optical phase change of the IFPIs.

2.2 Operational principle

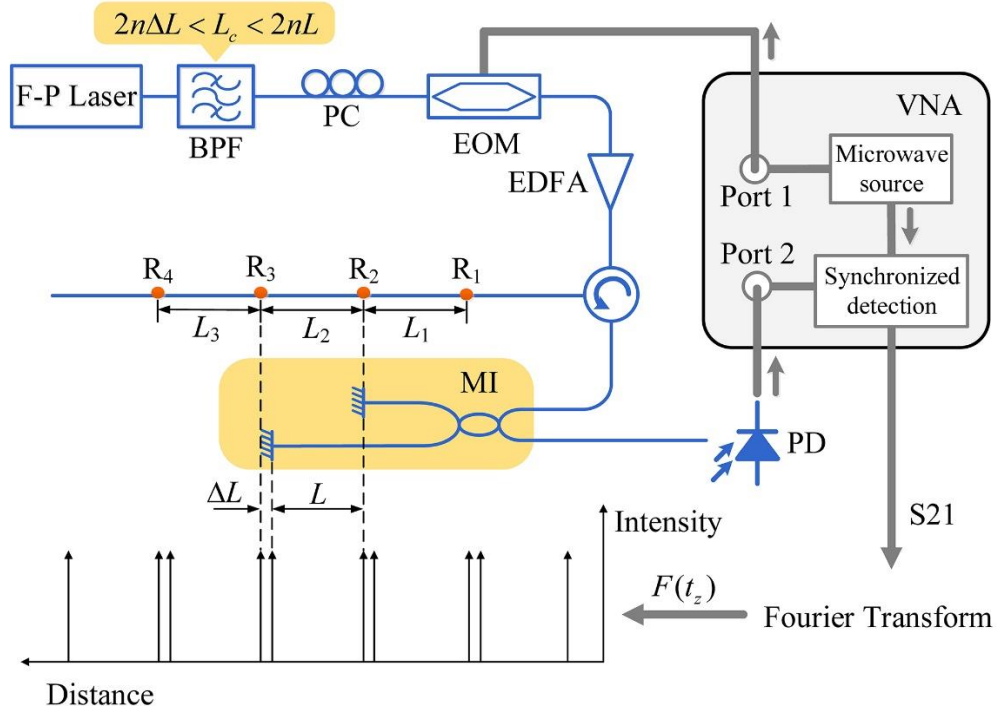


Figure 2.1 Schematic of the MPLCI system. L_c , coherent length of the light; BPF, bandpass filter; PC, polarization controller; EOM, Electro-optic modulator; EDFA, Erbium-doped fiber amplifier; PD, photodetector; VNA, vector network analyzer.

The schematic of the MPLCI system is shown in Figure 2.1. A single longitude mode of the F-P laser (HP81554) is selected out by a 1 nm bandpass filter (BPF). The output light has a center wavelength of 1543 nm and a full width at half maximum (FWHM) of 1.5 GHz. The coherence length of the output light is estimated as 6 cm. The microwave signal is intensity-modulated on the light via an EOM, which has a bandwidth of 10 GHz. An in-line polarization controller (PC) is used to optimize the modulation

depth of the EOM, which is connected to port 1 of a VNA (Agilent E8364B). The microwave-modulated light is first amplified by an erbium-doped fiber amplifier (EDFA), and then launches into the sensing fiber. The sensor array is formed by weak reflectors with reflectivity around -30 dB, which are fabricated using femtosecond laser micromachining [55], [56]. Cascaded FPIs are formed by adjacent reflectors (e.g., R1 and R2) with similar cavity length. The reflected lights are then coupled into the MI, which is made of a coupler and two Faraday rotation mirrors (FRM). The MI is well confined and stabilized in a black box using epoxy to minimize environmental vibrations' influence. The cavity lengths of FPIs (L_1, L_2, L_3 , etc.) are designed to match the OPD of MI (L), and ΔL represents the maximum matching deviation. The coherent length of the light is larger than $2n\Delta L$ and much smaller than $2nL$, where n is the refractive index of the fiber. As such, the interference occurs between each pair of lightwaves: one passes through the reflector ($i-1$) and the long arm of MI; the other passes through the reflector i and the short arm of MI. The output light is detected by a high-speed photodetector, which has a bandwidth of 10 GHz, and then connected to the port 2 of the VNA. Synchronized detection, which compares the amplitude and phase difference between the source signal and received signal, is implemented to obtain the complex frequency response S_{21} [52], which can be expressed as

$$\begin{aligned}
S_{21}(\Omega) = & \frac{M}{2} \sum_{i=1}^N A_i^2 \left(e^{-j \frac{Z_{s,i} n \Omega}{c}} + e^{-j \frac{Z_{l,i} n \Omega}{c}} \right) \\
& + \frac{M}{2} \sum_{i=2}^N A_i A_{i-1} \cos(\phi_{s,i}(\omega) - \phi_{l,i-1}(\omega)) \left(e^{-j \frac{Z_{s,i} n \Omega}{c}} + e^{-j \frac{Z_{l,i-1} n \Omega}{c}} \right),
\end{aligned} \tag{2.1}$$

where M is the modulation depth of the EOM, Ω is the microwave frequency, ω is the optical frequency, c is the speed of light in vacuum, $Z_{s(l),i}$ represents the path that travels through the short (long) arm of MI and the reflector i , A_i is the amplitude of the light that is reflected by reflector i , and ϕ is the optical phase delay. By applying a complex Fourier transform, the time-domain signal can be reconstructed as

$$F(t_z) = \sum_{i=1}^N \left[I_{s,i} \delta(t_z - \frac{nZ_{s,i}}{c}) + I_{l,i} \delta(t_z - \frac{nZ_{l,i}}{c}) \right], \quad (2.2)$$

where t_z is the time variable, $\delta(t_z - nZ_{s(l),i}/c)$ represents the pulses with different time delay and $I_{s(l),i}$ is the pulse intensity. The width of transformed time-domain pulses cannot approach to zero because of the finite microwave scanning bandwidth. Since the pulses at the location of $nZ_{s,i}/c$ and $nZ_{l,i-1}/c$ will be merged, there are $N+1$ pulses shown in the time domain. The intensity of the k th pulse is given by

$$I_k = \frac{M}{2} \begin{cases} A_1^2, k=1 \\ A_k^2 + A_{k-1}^2 + 2A_k A_{k-1} \cos \left[\frac{2n\omega}{c} (\Delta L_{k-1} + L_{k-1} \varepsilon) \right], k \in [2, N], \\ A_N^2, k=N+1 \end{cases} \quad (2.3)$$

where $\Delta L_{k-1} = L_{k-1} - L$ and ε is the applied strain. As shown in Equation (2.3), the intensity of the first and last pulses are not affected by the gauge length variation. For the remaining $(N-1)$ pulses, their intensities not only depend on the reflectivity of in-fiber reflectors, but also depend on the optical phase difference introduced by the applied strain. The intensity of the k th pulse, where $k \in [2, N]$, changes sinusoidally as the function of the strains between $(k-1)$ th and k th reflectors.

Therefore, by detecting the pulses' relative intensity change, the gauge length variation can be obtained.

According to Equation (2.3), the interference phase sensitivities to the optical frequency and strain are

$$\begin{aligned}\left.\frac{d\phi}{d\omega}\right|_{\varepsilon=0} &= \frac{2n}{c}\Delta L, \\ \frac{d\phi}{d\varepsilon} &= \frac{2n}{c}\omega L,\end{aligned}\tag{2.4}$$

respectively. Compared with a simple FPI, which has a cavity length of L , the strain sensitivity is the same ($2n\omega L/c$) for both interferometers, whereas the optical frequency sensitivities are different ($2n\Delta L\omega/c$ for LCI and $2nL\omega/c$ for a simple FPI). Because the matching deviation ΔL is much smaller than the cavity length L , the MPLCI system is less sensitive to light source wavelength drifting.

2.3 Experiments

Two experiments were designed and conducted to demonstrate the MPLCI system. First, the mathematical model was verified by a quantitative strain measurement experiment using motorized linear translation stages. All the sensors were applied with the same strains by dragging the fiber at one end. Subsequently, a cantilever beam was used to test the distributed sensing capability of the proposed system. In both experiments, the frequency scanning range of VNA was set between 0.1 and 5.1 GHz with 6401 sampling points and an intermediate frequency bandwidth (IFBW) of 5 kHz. The measurement cycle time was about 1.35 s.

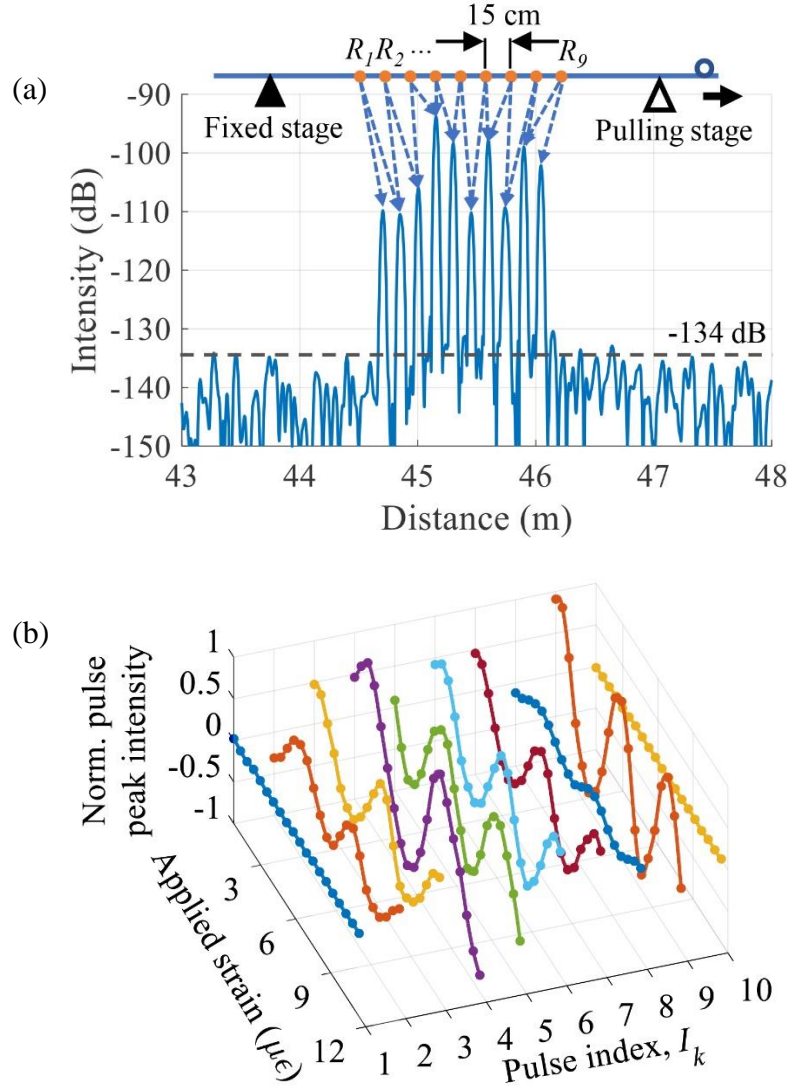


Figure 2.2 (a) Experiment setup of quantitative strain measurement and the reconstructed time-domain signal with an applied strain of $0.565 \mu\epsilon$. (b) The normalized peak intensities of ten pulses were extracted with respect to the applied strains.

The setup of the first experiment is shown in Figure 2.2(a). Nine reflectors were fabricated on a single-mode fiber (SMF) to form the sensor array. The cavity lengths of FPIs along the fiber and the OPD of MI were about 15 cm. The sensor array was fixed on two motorized linear translation stages (PM 500, Newport) using all purposes glue. The

distance between the two fixing points was 1.77 m. Axial strains of $0.565 \mu\epsilon$ per step were applied to the cascaded sensors by moving one stage at $1 \mu\text{m}$ per step. A total strain of $11.3 \mu\epsilon$ was applied to the sensors during the whole measurement.

Using complex Fourier transform, the spatial (time) domain signal $F(t_z)$ was reconstructed (as shown in Figure 2.2(a)). With the assistance of the MI, ten pulses were formed by nine weak reflectors, which can be clearly resolved at different locations. The time-domain signal had a noise floor of 134 dB. The eight pulses in the middle had a maximum $\text{SNR}_{\text{pulse}}$ of 40 dB and a minimum $\text{SNR}_{\text{pulse}}$ of 24 dB. By extracting and normalizing each pulse's peak intensity under different applied strains, we plotted Figure 2.2(b) (each curve was zero centered and divided by the peak value of the ninth curve, $7.18 \mu\text{U}$). The first and the last pulses did not experience noticeable intensity changes, while the intensity of the remaining pulses changed sinusoidally to the applied strains. I_k experienced different peak-to-peak values and biases for different k , which were caused by the different amplitudes of the reflected light, A_k , for different weak reflectors. The initial phases were also different because of the different matching derivations ΔL_{k-1} . The SNR of each LCI was calculated by dividing the noise power from the power of sinusoidal function ($20\log_{10}(I_{k,\text{rms}})-134$) [57]. The eighth sensor (ninth pulse) had the largest SNR_{LCI} of 28 dB, and the seventh sensor (eighth pulse) had the lowest SNR_{LCI} of 11 dB. The SNR_{LCI} can be further optimized by decreasing the VNA's IFBW, increasing the number of averaging times, or increasing the reflectivity of the weak reflectors.

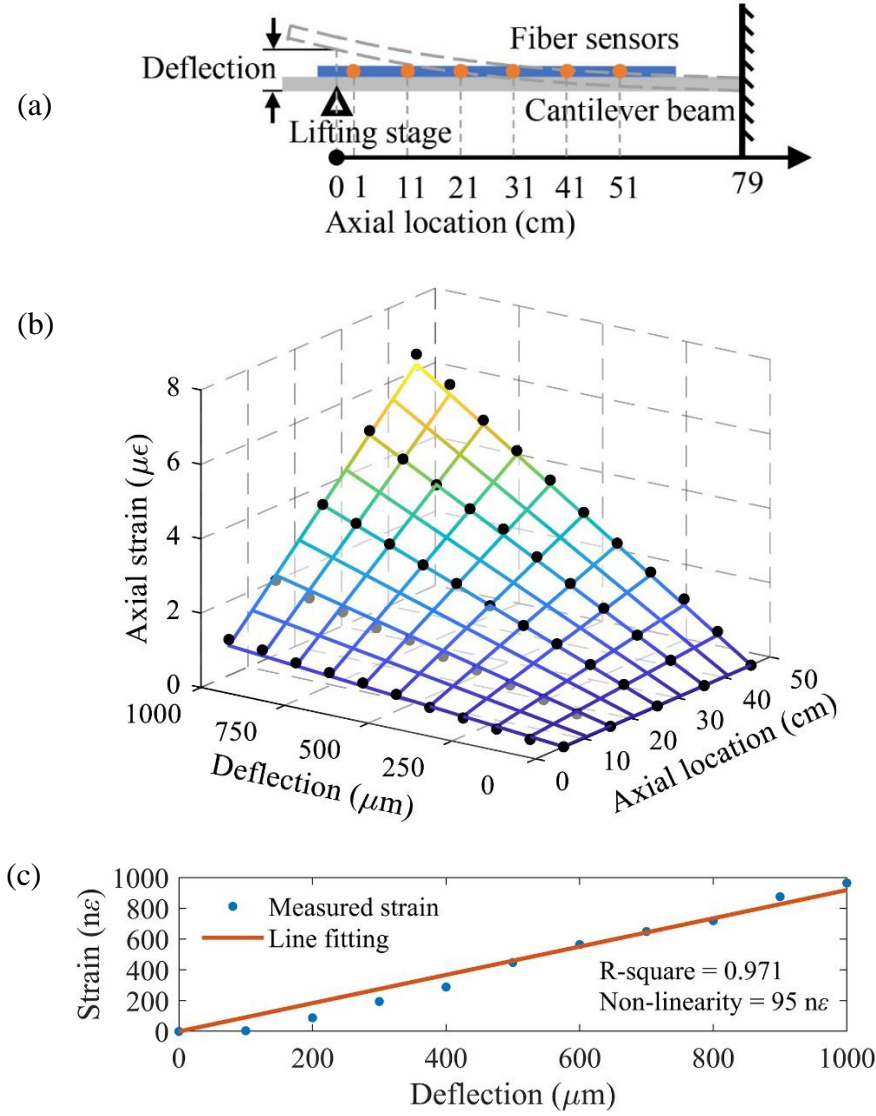


Figure 2.3 (a) Experiment setup of cantilever beam distributed strain measurement. (b)

Measurement (black dots) and theoretical simulation (colored mesh grid) results of strains along the cantilever beam with respect to the vertical deflection and axial location.

(c) Zoomed-in view of the data from the first sensor (located at the range from 1 cm to 11 cm), in which orange line is the line fitting results of the measure strain data (blue dots).

The second experiment was designed to test the distributed sensing capability of the proposed system. As shown in Figure 2.3(a), six reflectors along the fiber formed 5

FPIs. The separation distance between reflectors was decreased from 15 cm to 10 cm for an improved spatial resolution (the OPD of MI was also 10 cm). The sensing fiber was epoxied on the surface of an aluminum cantilever beam with length, width, and thickness of 914.4 mm, 38.1 mm, and 3.175 mm, respectively. One side of the beam was clamped in a vice, and the other side was vertically lifted by a micro-actuator with a step of 100 μm . A total deflection of 1000 μm was created throughout the measurement. The distance from the micro-actuator to the clamp and from the micro-actuator to the first reflector was 79 cm and 1 cm, respectively. As the cantilever beam was vertically deflected, the amounts of axial strain detected by the distributed fiber sensors were different. The mathematical model of the cantilever beam used to calculate the strain distribution was [58]

$$\varepsilon = \frac{3h}{2l^3} \delta x, \quad (2.5)$$

where h is the thickness of the beam, l is the distance between the micro-actuator and the clamp, δ is the vertical deflection distance, and x is the axial location which orients at the micro-actuator towards the clamp. Since the strains are linearly distributed along the axial direction, the measured strain should be equal to the theoretical values calculated at each sensor's center.

The interference phases of IFPIs were measured using the chirp effect of EOM to perform the quadrature-phase demodulation [53]. Specifically, by tuning the bias of EOM, a phase difference of $\pi/2$ is applied to the real and imaginary parts of the complex time-domain pulses ($\cos(2n\omega(\Delta L + L\varepsilon)/c + \pi/4)$) and $\cos(2n\omega(\Delta L + L\varepsilon)/c - \pi/4)$. Therefore, a standard quadrature-phase demodulation

method can be used to resolve the interference phase ($2n\omega(\Delta L + L\varepsilon)/c$) and the applied strains. The measured values (black dots) and simulated results (colored mesh grid) with respect to the deflection and axial location were shown in Figure 2.3(b). The strain increased at the location that was closer to the clamped end of the beam. The strain also increased at the same location as the deflection increased. The measurement data showed the same trend as the mathematical model predictions. The small deviations between them could be caused by some unavoidable system errors. For example, the sensing fiber was not fully attached to the surface of the cantilever beam with uniformly distributed internal stress, and the vice did not tightly fix the beam. Figure 2.3(c) shows the zoomed-in view of the data from the first sensor (located at the range from 1 cm to 11 cm). The orange line was the line fitting results of the measured data (blue dots) with an R-square value of 97.1%, a root-mean-square error (RMSE) of 59 nε, and a non-linearity of 95 nε (maximum deviation between measured data and fitted line). As such, the resolution of the fiber sensor was estimated to be better than 100 nε. Compared with a similar experiment conducted using the incoherent MPI system [51], the MPLCI system has improved the sensitivity by three orders of magnitude (from sub-mε to sub-με).

The performance limitation of the proposed system is far beyond what has been achieved in this preliminary setup. According to Equation (2.4), the strain sensitivity is proportional to the cavity length L , indicating that nε sensitivity is achievable by implementing a 1 m-length-gauge. At the expense of increasing the measurement time, the spatial resolution and measurement range also can be further improved. With 100,000 frequency scanning points, a spatial resolution of 10 cm over the range of 5 km can be

achieved with a microwave scanning range of 2 GHz and a scanning step of 20 kHz. In addition, the method of low coherence interferometry (LCI) can be easily extended to demodulate other cascaded interferometers for fully distributed sensing.

CHAPTER THREE

ALL-DIGITAL DOWNHOLE PRESSURE SENSOR BASED ON AN ELECTRICAL ENCODER

3.1 Introduction of all-digital sensing method

3.1.1 Motivations

In the previous chapter, a fiber optic fully distributed sensing system with high sensitivity and high spatial resolution is developed. In general, the fiber optic downhole sensors do not need on-site electronics placed in the downhole environment. The hermetically packaged optical fiber itself acts as both the distributed sensing element and the signal transmission medium [59]. These microsensors passively and linearly transduce the temperature/pressure to optical signals that are transmitted to the interrogation instrumentation on the surface. They have high pressure sensitivity and high operation temperature. However, these fiber optic pressure sensors are fragile, difficult to package, and have shown large drift when used in downhole environments over extended periods of time. Also, these systems are too costly to be utilized for UOG recoveries. On the other hand, the electronics components inside the existing electrical downhole sensors, for on-spot signal conditioning and downhole data telemetry, has created the technical and economic barriers to widely use distributed pressure data for improved the recoveries of UOG.

The all-digital sensing method that completely eliminates the needs for downhole electronics, but still produces a signal of excellent quality in harsh environment and can be remotely interrogated over a long distance. Figure 3.1 illustrates the all-digital sensing

concept in comparison with the existing approaches. The most important components of the all-digital sensor are the built-in nonelectronic amplification and the nonelectronic analog to digital converter (i.e., the mechanical ADC).

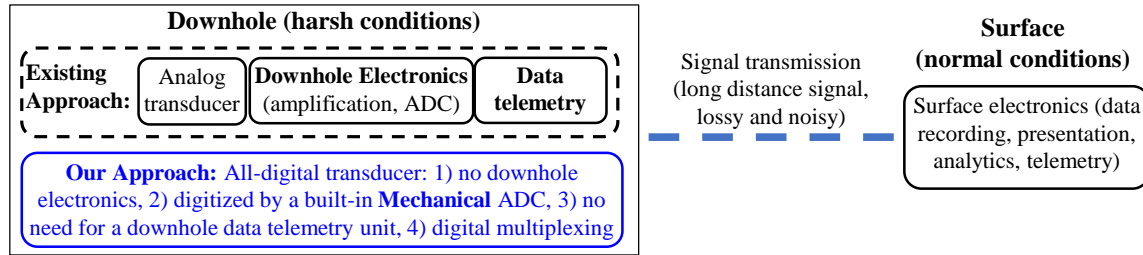


Figure 3.1 Comparison between the existing approach and all-digital sensing method for downhole monitoring.

The digital representation of the data has the advantage of being able to transmit over a long distance with much improved fidelity. This is easily understandable when considering the unprecedented voice and data communication capability of a small modern digital cellphone comparing with an old analog wireless phone. Some existing sensors use an electronic ADC to convert the analogy signals into a digital (1/0) format. One possible solution to the problem is to use a downhole mechanical ADC, instead of an electronic ADC, to convert the transducer signal into a digital format. The mechanical ADC has a much better stability to operate reliably in the high temperature downhole environment. Without the downhole electronics, the new all-digital sensors are more robust and cheaper compared with existing sensors. Because the outputs are digital in nature, the sensors can be remotely logged over a long distance, and many sensors can be digitally multiplexed for distributed sensing using a single surface instrument. These

technical innovations may provide an affordable solution for improved recoveries of UOG.

3.1.2 Operational principle of all-digital sensing method

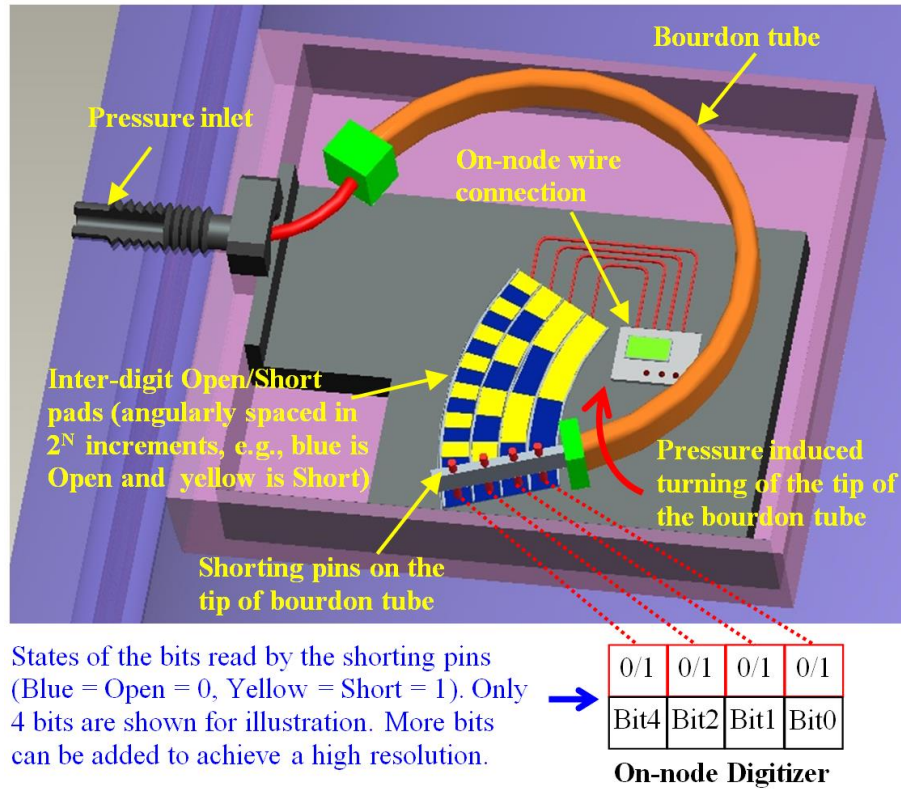


Figure 3.2 Principle of the all-digital downhole pressure sensor.

Figure 3.2 shows an example design of the proposed all-digital downhole pressure sensor for the purpose of illustration. To survive the harsh downhole conditions, a bourdon tube is chosen as the sensing element because of its built-in amplification of the pressure signal and the proven robustness over the history of pressure sensor development. When exposed to the downhole pressure, the bourdon tube produces a movement at its tip that is proportional to the liquid (or gas) pressure. The innovation of the proposed sensor is the all-digital readout of the amount of tube tip turning by the

built-in mechanical digitizer at the tip of the coil. The digitization is realized by the combination of the inter-digit pads and the shorting needles mounted on the tip of the bourdon tube. The inter-digit pads have N channels and their angular spacings are arranged in the form of $2N$ increments. When the shorting pin mounted at the coil tip is touching the blue portion, the state is “Open”, representing a digital “0”. When the pin moves to touch the yellow portion, the state changes to “Short”, representing a digital “1”. As such, the amount of tube tip turning is digitized according to the $2N$ format. The angular position of the bourdon tube is determined by the combined digital states (0 or 1) of the N channels.

3.1.3 Advantages of all-digital pressure downhole sensors

Compared to the existing state-of-the-art techniques, the proposed all-digital sensing platform has a number of unique features that are particularly advantageous for distributed pressure monitoring in very cost sensitive UOG fields. These unique advantages include:

- (1) High-temperature and high-pressure capability to survive and operate in the downhole conditions permitted by the simple and reliable sensor structure and high temperature materials (e.g., the bourdon tube and the mechanical digitizer).
- (2) Low-cost implementation warranted by the built-in mechanical digitization mechanism and elimination of downhole electronics for signal conditioning.
- (3) The unique multiplexing capability (by cascading many sensors along a single cable) enabled by the digital nature of the sensor.

(4) Reliable digital signal transmission over a long distance from downhole to the surface without using downhole telemetry electronics. When connected with a cable, the Short and Open states can be easily detected over a long distance.

(5) In addition to pressure measurement, the all-digital platform can be flexibly designed/modified to measure other downhole parameters such as temperature and acoustic.

3.2 All-digital downhole pressure sensor design overview

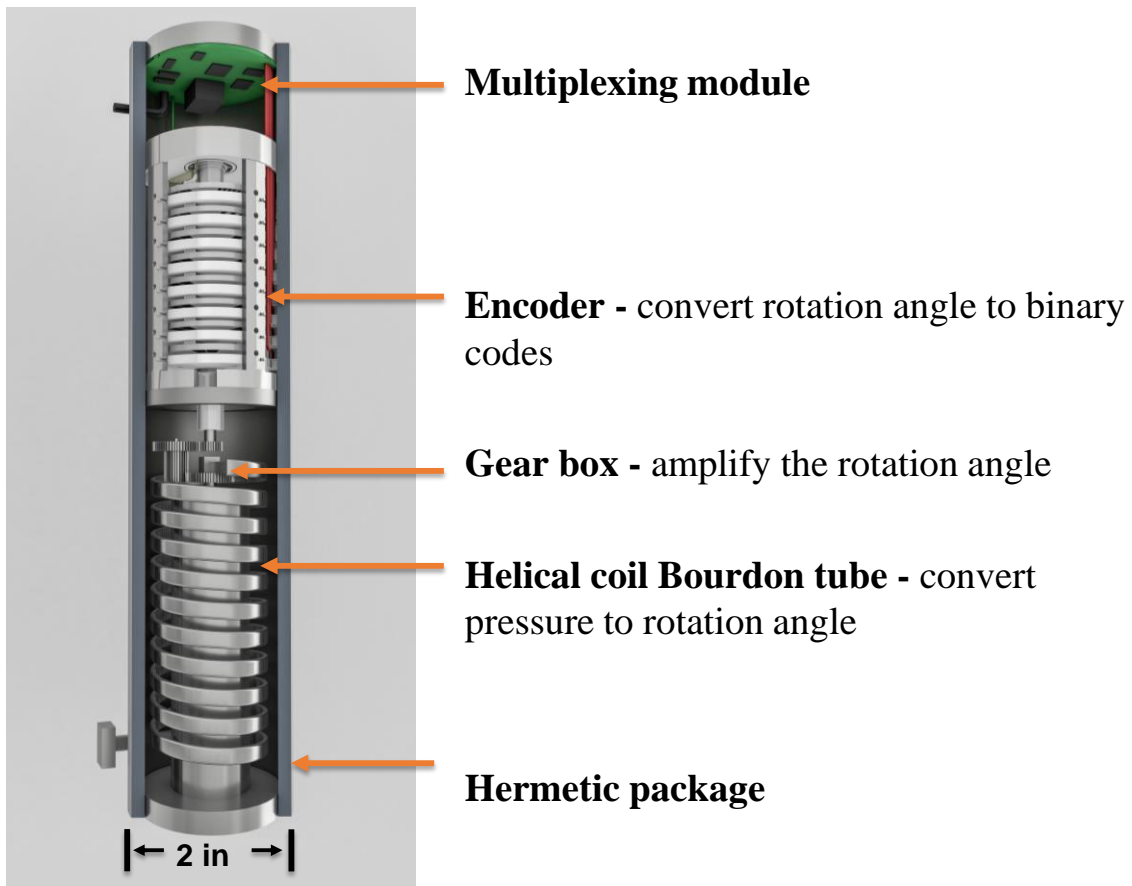


Figure 3.3 3D design model of the all-digital pressure sensor.

Figure 3.3 shows the design model of the prototype pressure sensor, which is composed of five main components: a data telemetry module, digitizer, gear set, helical coil Bourdon tube, and hermetic package. The sensor couples the outside pressure through the pressure inlet. The helical coil Bourdon tube converts the applied pressure to rotation angles. An optional gear set can be used to amplify the rotation angle. The digitizer, which acts as a rotary encoder, encodes the rotation angle as digital states. The data telemetry module on the top detects and transmits the digital states. The sensor has a diameter of about 2 inches. The sensor is designed to be separated as different modules. Each module has its own functions. The replacement or upgrading of one module won't influence others. And the new module can be easily connected to the un-upgraded ones by using the standardized interface connectors. In the following section, the developments of each individual module will be described.

3.3 Module developments

3.3.1 Helical coil Bourdon tube



(a)



(b)



(c)

Figure 3.4 Different types of pressure transducer. (a) C-type (single coil) Bourdon tube.

(b) Metal bellow tube. (c) Helical coil Bourdon tube.

Figure 3.4(a) shows a commercially available Bourdon tube. This C-type Bourdon tube has good reliability and low cost. However, its pressure sensitivity is relatively low and its radius dimension is too large for downhole applications. Figure 3.4(b) shows a metal bellow tube. It has a small radius dimension, but it is difficult to fabricate for high pressure measurements. Figure 3.4(c) shows the design of a helical coil Bourdon tube. It can be seen as multi coil C-type Bourdon tube. So, it has a much higher pressure sensitivity than C-type Bourdon tube. And radius dimension can be minimized to meet the downhole application requirements.

The helical coil Bourdon tube was fabricated from a 304 stainless-steel tubing. The tubing was first flattened into an elliptical cross-section shape and then wrapped around a cylindrical rod. The first prototype sensor was made by a tubing with an outer diameter of 13/32 inches and a wall thickness of 0.068 inches.

As shown in Figure 3.5(a), the helical coil Bourdon tube was tested using a deadweight tester. The applied pressure was varied from 500 psi to 4000 psi at an increment step of 500psi. At each pressure, a digital camera was used to record and compute the rotation angle of the coil. An extension pointer was connected at the end of the Bourdon tube to enlarge the rotating movements. The measuring process was repeated seven times. The average angle rotations and their standard deviations (σ) at different applied pressures were shown in Figure 3.5(b). The maximum standard deviation was found to be $\sigma_{\max} = 0.047$ degree.

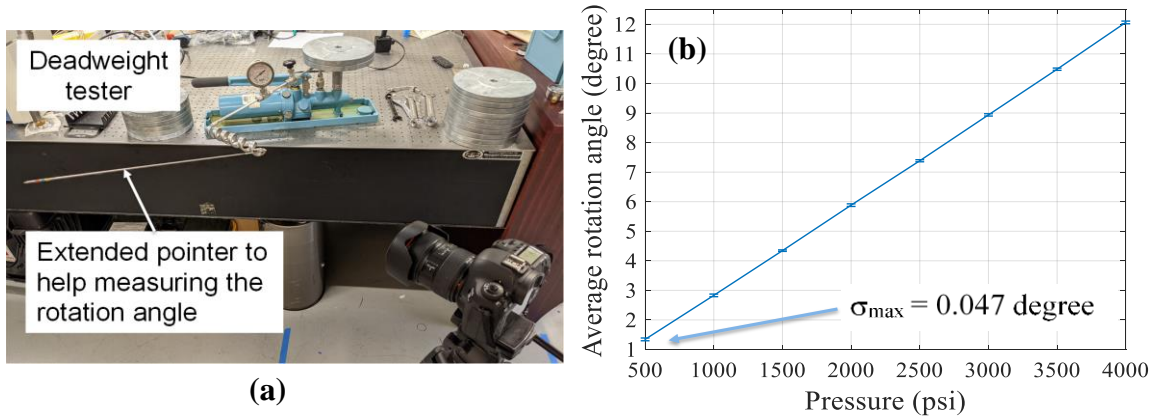
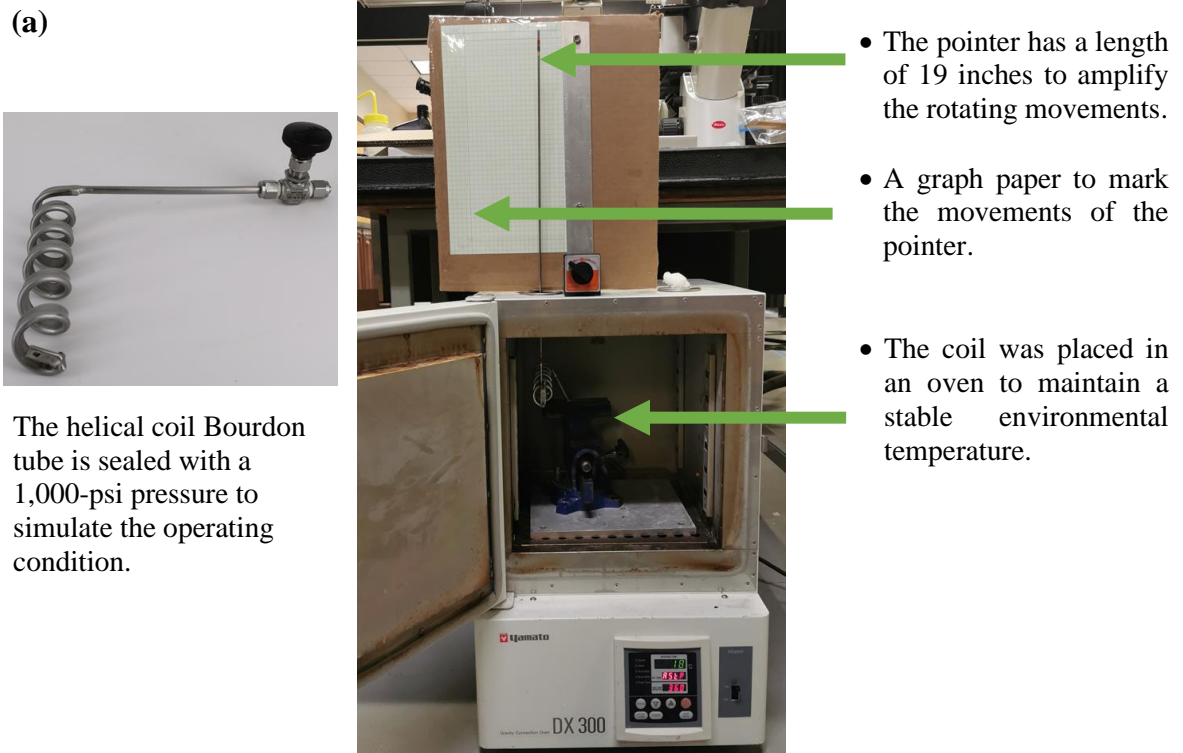


Figure 3.5 Test of the sensor resolution. (a) Picture of the experiment setup, (b) Rotation angle of the helical coil Bourdon tube at different applied pressures.



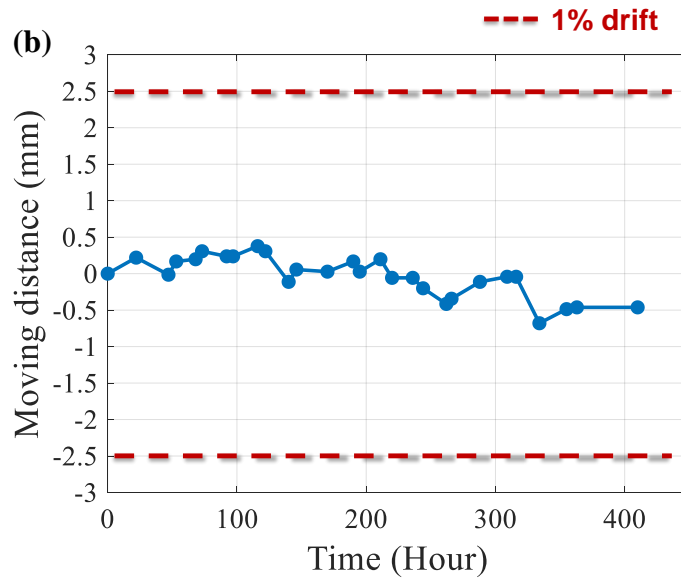


Figure 3.6 Long-term stability of the helical coil Bourdon tube. (a) Pictures of the experiment setup. (b) Test results indicate that the drift is well within $\pm 1\%$ over the duration of 410 hours.

The long-term stability of the helical coil Bourdon tube has been tested. Figure 3.6(a) shows the pictures of the experimental setup, where a helical coil Bourdon tube is sealed with a pressure of 1000 psi and placed inside an oven. The temperature of the oven is set to be 40°C . The Bourdon tube is connected to a long pointer (19 inches in length) to amplify the rotating movements. A graph paper is used to mark the movement of the pointer so that the pointer's position can be easily recorded by a digital camera. Figure 3.6(b) shows the test results, where the pointer movement is plotted as function of time (about 410 test hours in total). The 1% drift lines are marked in Figure 3.6(b) for easy visualization. In this particular experiment setup, 1% corresponds to 2.5mm of the pointer movement. The moving distance of the pointer is about $\pm 0.5\text{mm}$ (or $\pm 0.2\%$).

Second version of Bourdon tubes using a different dimension of tubing was

fabricated to optimize pressure sensitivities. The fabricated coil using a 1/4 inches tubing with a wall thickness of 0.035 inches is shown in Figure 3.7 (a). The end of the coil was smoothly transformed to a straight tubing, which is then connected with a standard Swagelok tubing connector. Before testing, the coil was placed in a temperature chamber to release the residue stress. The applied pressure for both coils was increase from 0 psi to 6000 psi with 500 psi steps, and then released back down to 0 psi. At each applied pressure, the rotation angle of the coil was measured by a camera.

The test results are shown in Figure 3.8. Before the 3rd test, we had already applied 6000 psi pressure to the coil. The rotation angle shift at 0 psi was 0.1 degree, which is very close to the angle measurement resolution. The test results confirmed that the heat treatment and repeatedly testing the coil at high pressure could help release the residue stress. Hence, the repeatability of the coil was increased.

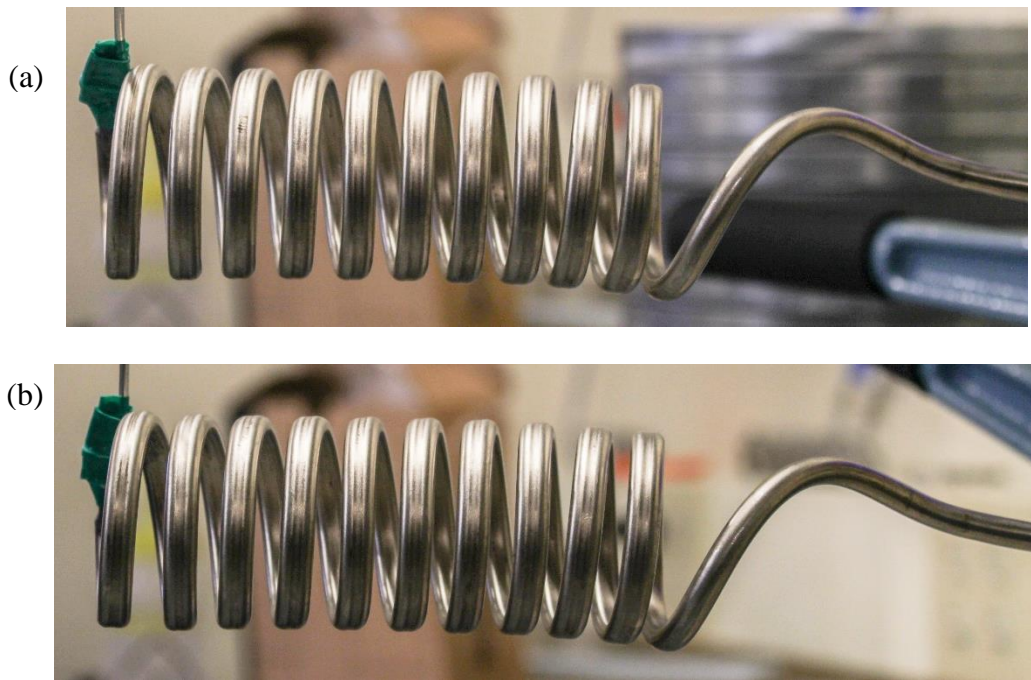


Figure 3.7 Picture of the coil at (a) 0 psi and (b) 6000 psi. No cross-section shape

deformation at the transition section. No abnormal bending at 6000 psi.

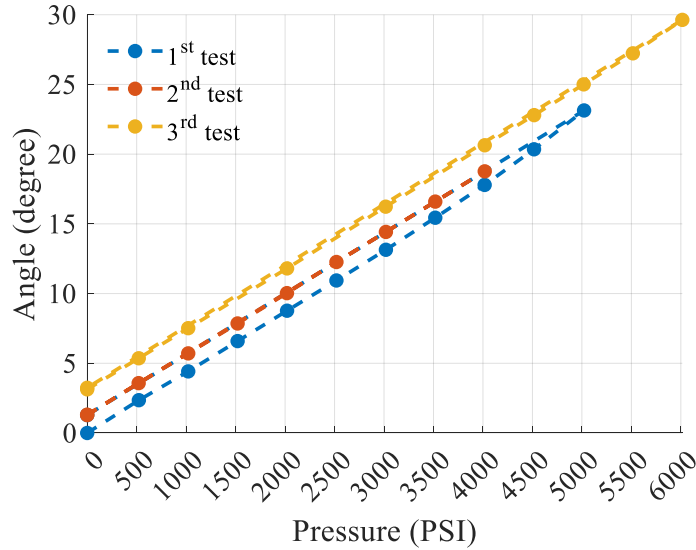


Figure 3.8 Test results of third version of Bourdon tube.

The third version of the Bourdon tube was fabricated to optimize the inter-module connection structures and minimize the sensor's hysteresis. Because the friction force of digitizer will prevent the Bourdon tube from rotating, the measurement hysteresis is generated when the drive force provided by the Bourdon tube is smaller than the friction force. Based on the ANSYS simulation and mathematic model of the Bourdon tube, increasing the tube OD and wall thickness could increase the driving force under the same pressure variations. As such, it is desired to use the tubing with a larger OD. However, increasing the tubing OD makes it harder to fabricate the coiled tube. By testing different tubing dimensions, e.g., OD of 3/8", 1/2", 5/8", and 3/4" and wall thicknesses of 0.035", 0.049", and 0.065", we found that the tubing with an OD of 5/8" and a wall thickness of 0.049" worked the best. Figure 3.9 shows the pictures of the fabricated Bourdon tube. The

tube was cold bent with two connectors welded on both ends. The two welded connectors ensure the rotation center of the Bourdon tube is aligned to the center of the gearbox. Bourdon tubes with three and four coils were fabricated to obtain different measurement ranges.

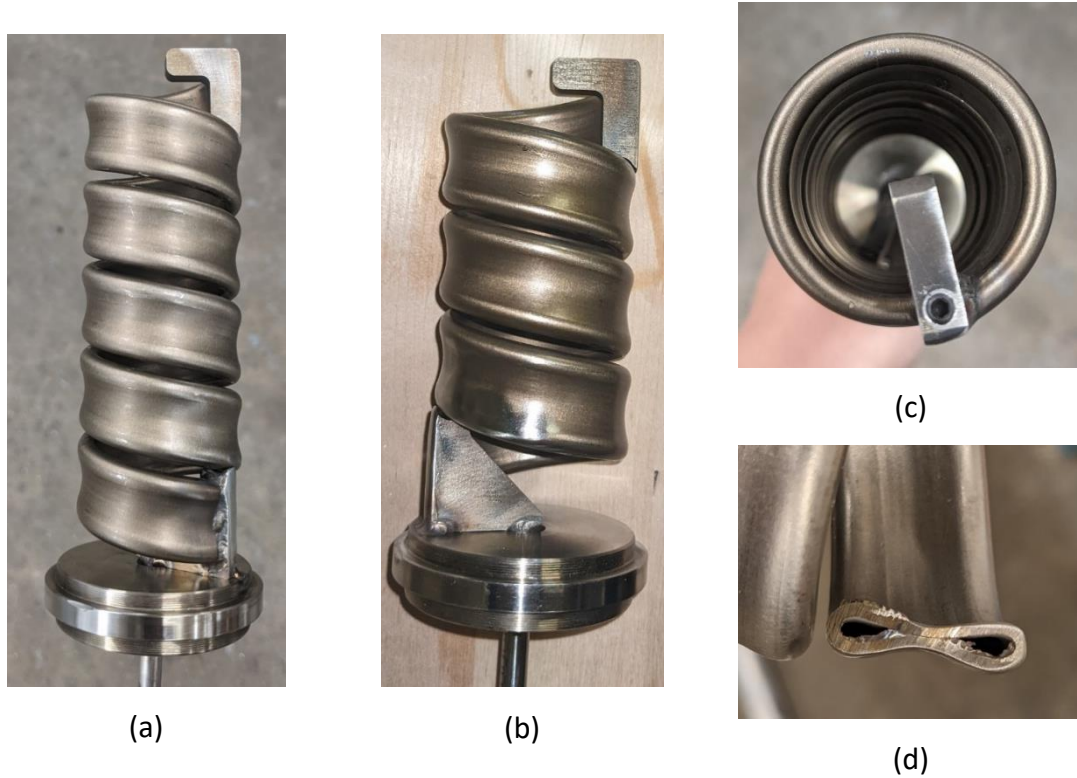


Figure 3.9 Two types of Bourdon tubes with four coils (a) and three coils (b). (c) Top view. A set screw was used to seal off the tube. (d) Cross section view.

3.3.2 Gear box module

To achieve high precision and short fabrication time, the design is mainly based on commercially available products, such as the gearbox (colored in purple, Nordex GEX-R3-4), shaft coupler, and standoffs. As shown in Figure 5(b), two stainless steel discs were added to hold the spring. Gearboxes with three different gear ratios, 15.27:1, 9.93:1 and

6:1, were purchased to satisfy different sensitivity and measurement range requirements. The gearbox is tightly fit to the slot fabricated on the bottom plate. Two shaft couplers are used to transmit the rotation angle from the Bourdon tube to the digitizer. An “L” shaped beam is used to connect the tail of the Bourdon tube to the center shaft.

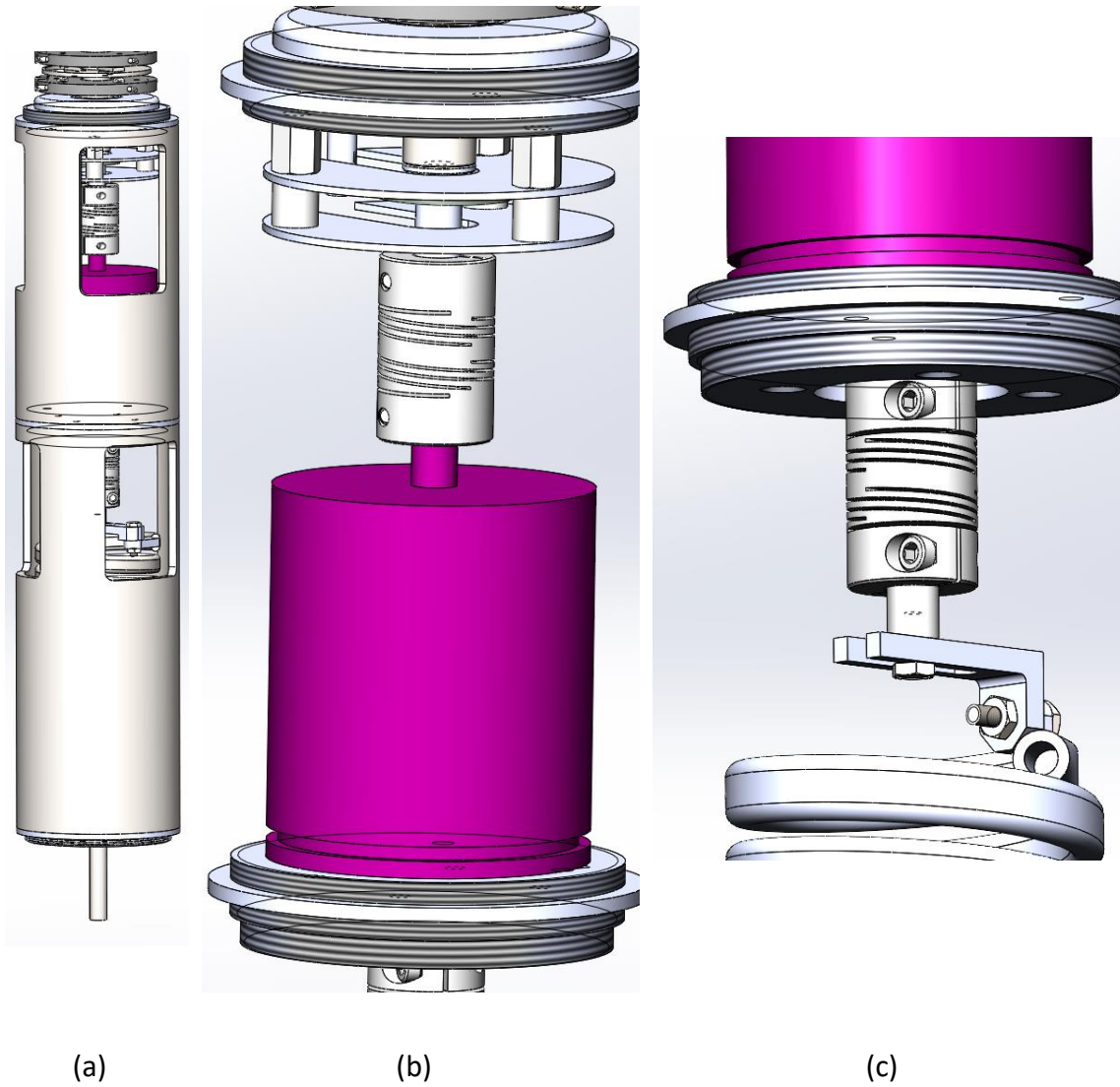


Figure 3.10 Solidworks models of (a) the housing, (b) the gear box, and (c) the connection between the Bourdon tube and the gear box.

3.3.3 Rotary encoder

Rather than encoding 8-bit channel into one pad (the conceptual design shown in Figure 3.2), the new design encodes 1-bit channel into each pad. The 8 encoding pads were vertically assembled. With the increased height, the diameter of the sensor can be decreased. The other advantage of this design is the extended encoding area. Therefore, the reliability of digital state readings can be increased, and the sensor will be less sensitive to environmental variations. This section will be constructed as follows. Firstly, the causes of erroneous digital states readings of are analyzed. Second, based on the results of erroneous reading analyses, three specific designs are detailed described. The strengths and drawbacks of each design are discussed. Third, the fabrication and assembly of each component will be introduced. Fourth, the angle resolution and long-term stability of the assembled encoder will tested.

3.3.3.1 Analysis for erroneous digital states readings

There are two essential components of the digitizer: the rotating part (shaft) and the fixed part (housing). The digital encoding pads and contact pins need to be attached separately to the shaft and housing. The relative movements between the two parts can be expressed as digital states. As such, we have two options to realize the design.

- 1) Set pads as the fixed parts and pins as the rotating parts. (Designs I and II)
- 2) Set pads as the rotating parts and pins as the fixed parts. (Design III)

The bottom line for the all-digital sensor design is to suppress the rate of erroneous digital state readings. As for the application of downhole pressure sensing, erroneous readings could be caused by any of four major factors:

1. 250°C operation temperature. High environment temperature restricts the choice of materials. A material with high temperature resistance can be used, such as stainless steel, high-temperature solder, and high-temperature epoxy. Furthermore, high operation temperature is usually accompanied with large temperature vibrations. Unexpected cracks or gaps may show up at the interface of the two materials with different thermal expansion coefficients (TEC). A large joint area between different materials should be avoided.
2. Vibrations. Welding or soldering should be used as the major connecting method.
3. Precise alignment among pads and contact pins. Since the N-bit digital channels are separated into N different pads, the positions of different pads need to be synchronized. At the same time, the contact pins also need to be aligned with their pads. Although the width and length of each bit channel is extended compared with the conventional design, it is still a challenge to avoid misalignment.
4. Reliable electrical connections. The pad and pin need to maintain high conductivity for a long time. They should be wearable and resistant to oxidation.

3.3.3.2 Design I: pin (rotation part) + pad (ceramic PCB)

The basic components of the all-digital sensor, which include the housing, shaft, pad holder, pad, pin holder, and pin, are shown in Figure 3.11, 3.12, and 3.13.

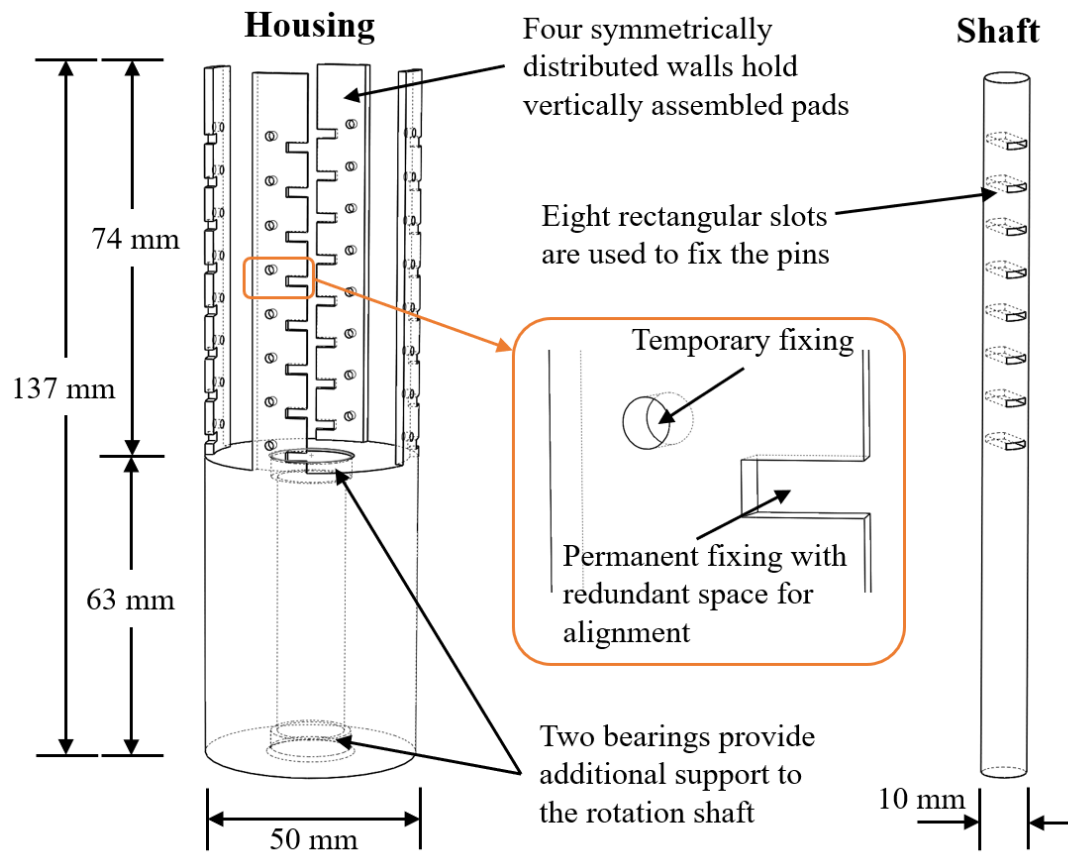


Figure 3.11 3D plots of the housing and shaft in Design I. The housing and shaft are made of stainless steel. The overall length of the sensor is 137 mm. The upper part of the housing is used for fixing the eight pads. The zoom-in view shows the temporary and permanent fixing points. The rectangular notches on the walls are used for alignment. The lower part of the housing is used to provide additional support to the shaft. The two bearings prevent the shaft from swaying. The shaft will be connected with the pressure transducer. The eight rectangular slots on the shaft are used to fix the pin holders.

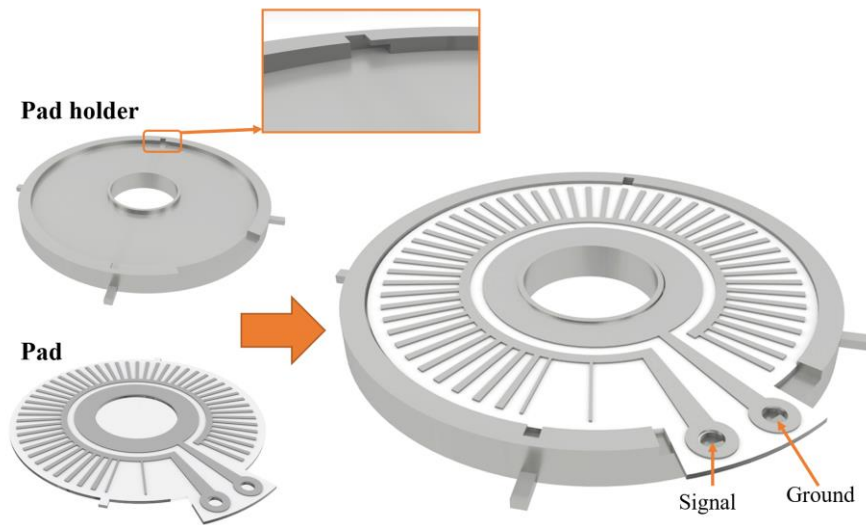


Figure 3.12 3D plots of the digital encoding pad and pad holder in Design I. The pad is made by a ceramic printed circuit board (PCB). The pad holder is made of stainless steel.

The pad is assembled by pushing and sliding into the two notches of the pad holder (shown in the zoom-in view). The outlet of the notch will be then filled by high temperature epoxy. The assembled pad is shown in the right of the figure. The two holes on the pad are the signal and ground ports.

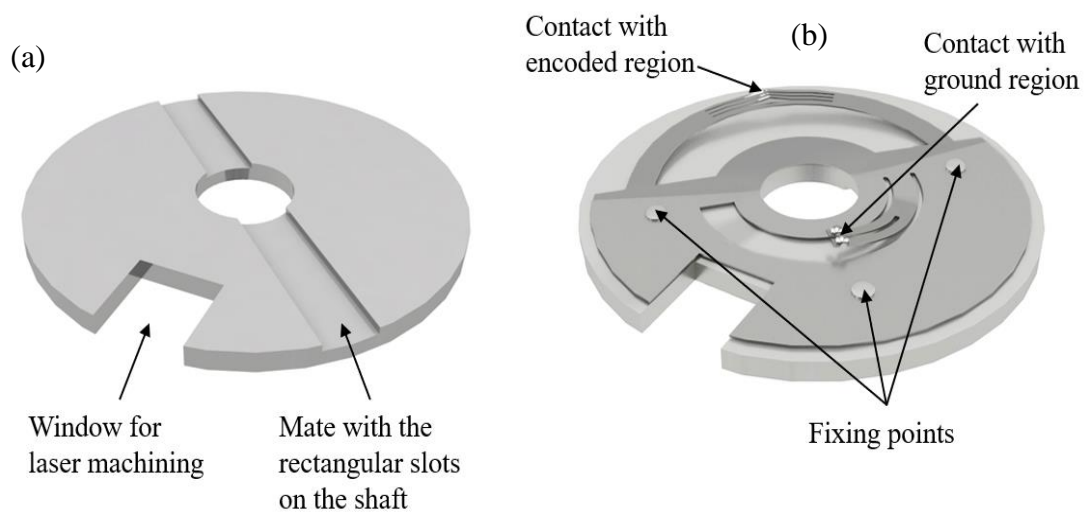


Figure 3.13 (a) the top view of pin holder and (b) bottom view of the pin holder assembled with the pin. The three small cylinders on the pin holder are used to locate and weld the pin.

As shown in Figure 3.14(a), the pad holder is assembled to the housing by the four bottom legs. After the pad holder has been tuned to the right position, it will be welded with the housing. The pin holder is assembled to the shaft by a rectangular plug. Figure 3.14(b) shows the results after the assembly. The plugs will be then welded with the shaft. Figure 3.14(c) is the full view of the all-digital sensor. The dimensions of the sensor are about 50 mm in diameter and 137 mm in height.

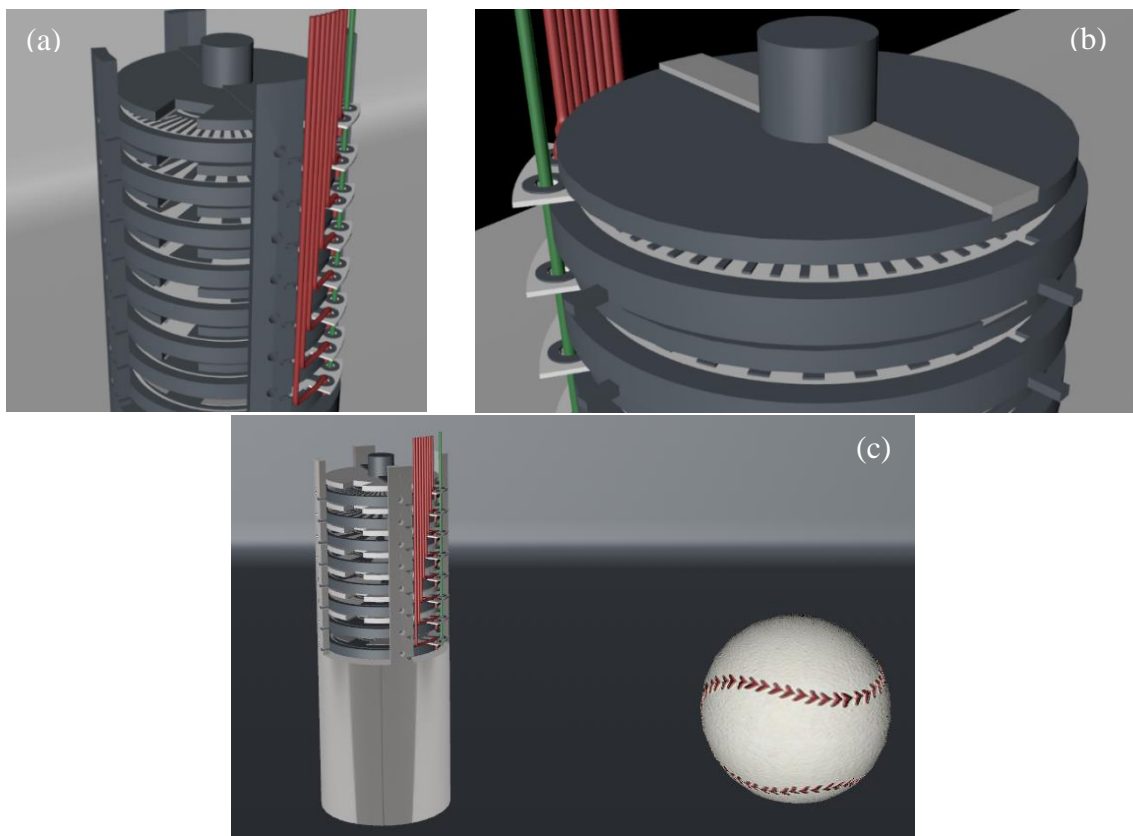


Figure 3.14 3D models of the all-digital sensor after assembly. (a) Detailed view of housing and pad holder. (b) Detailed view of shaft and pin holder. (c) Dimension comparison between the sensor and a baseball.

Alignment of the pad and pin is achieved by tuning the positions of the pad holder. As shown in Fig. 3, the redundant space of the permanent fixing point allows the pad holder to rotate within the range of ± 2 degrees. There is no adjustment mechanism in the horizontal direction, because the width of the encoding area is much larger than the width of the contact pins. The design also provides the opportunity to modify the pad via laser micromachining. As such, the alignment accuracy can be greatly increased.

Encoding pad design: The digital encoding pad used in Design I is a ceramic PCB. The CAD design file is shown in Figure 3.15. The two protrusions on the top and bottom are used for pad location and fixation with the pad holder. The ground region is in the inner ring, while the encoding region is in the outer ring. The digital numbers from 0 to 200 are encoded to achieve the resolution requirement of 0.5%. One digital number corresponds to the angle of 1.5 degrees. In practice, the width of the contact area between the pin and the pad is not infinitely small. If the conductive and non-conductive areas were evenly distributed, the area of “0” and “1” digital states would be different. As such, the conductive area is designed to be 0.3 degrees smaller than the non-conductive area. The advantages of using a ceramic PCB-based pad include high operation temperature, oxidation resistance, and capability for laser machining. In addition, the encoding region and ground region are electrically isolated by the ceramic substrate. There are no interconnections among different pads.

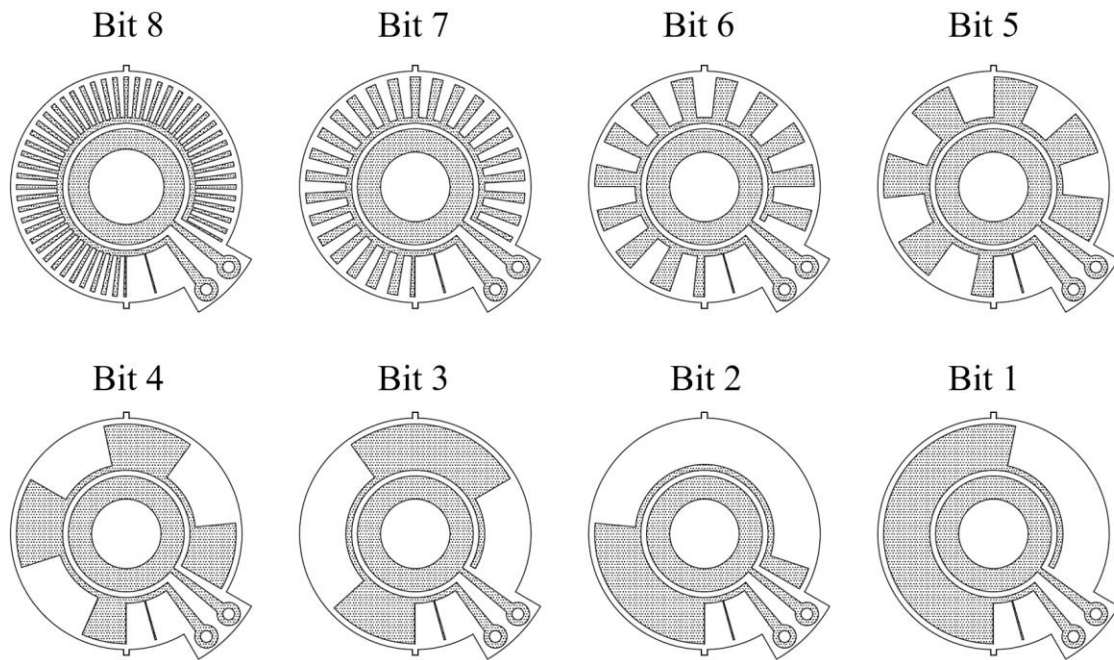


Figure 3.15 CAD design file of digital encoding pad from bit 1 to bit 8. The encoding region occupies 300 degrees. The shadowed area is the conductor.

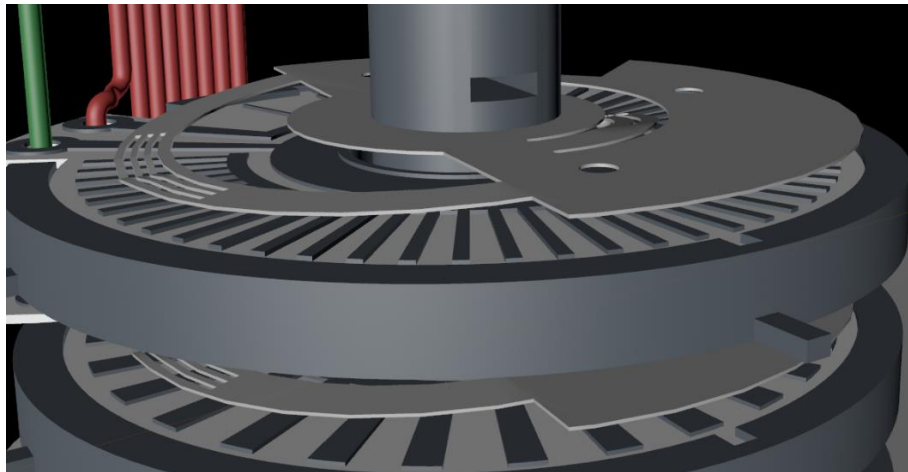


Figure 3.16 The relationship between pad and pin. The pin contacts the pad in both the encoding region (signal region) and the ground region. When the pin is sliding through the surface of a pad, the digital states change between “1” (open circuit) and “0” (short circuit).

The relationship between the pad and the pin is shown in Figure 3.16. The pin contacts the pad in both the encoding region (signal region) and the ground region. When the pin is sliding through the surface of a pad, the digital states change between “1” (open circuit) and “0” (short circuit). The contact pin can be seen as a bridge between the encoding and ground regions. It plays an important role in establishing reliable electrical connections. If the contacting force between the pad and the pin were too large, the contact points of the pin could be flattened after a long period of wear. If the contacting force were too small, the contact between the pin and the pad could be unstable during vibrations. In both cases, the probability of obtaining erroneous digital state readings would be increased. In addition, the pin also needs to have oxidation resistance at high temperature (250°C) to maintain high conductivity. It is important for achieving reliable readings over a long period.

Contact pin design: Figure 3.17(a) and (b) are the pin’s design files. Two sets of pins are designed to read the encoding region and ground region of the pad, respectively. As shown in the zoom-in view of Fig. 9(a), a small bump at each contact point decreases the contact area, thus allowing the pad and pin to be aligned more accurately. The red dashed lines marked in both Figure 3.17(a) and (b) indicate the positions and directions to bend the pin. The height of the pin after bending determines its elasticity. The material used to fabricate the pin is beryllium bronze with a thickness of 0.2 mm. It has the features of high conductivity, high oxidation resistance and high abrasion resistance, making it very suitable for the applications of electrical brushes or contact pins.

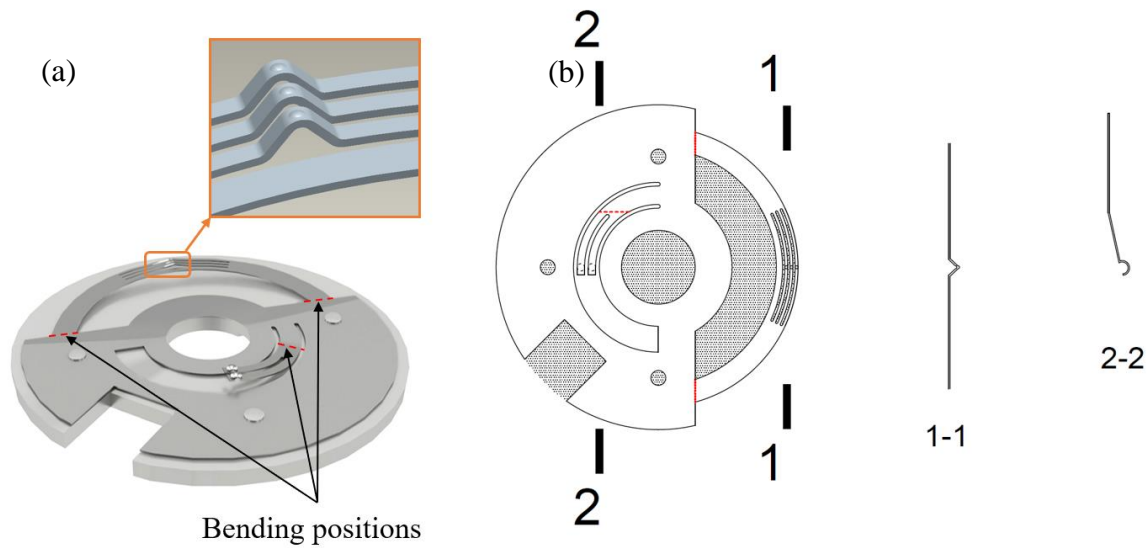


Figure 3.17 (a) 3D and (b) 2D design files of contacting pins. Three bending positions have been marked out using red dashed lines. The height of pins after bending influences the contacting force when the pin is assembled with the pad. The zoom-in view and cross-section views show the detailed design of the contacting points. There is a small bump at each contact points to decrease the contact area.

Drawbacks of Design I: The conductor of the pad is made of copper. Although we can coat gold on the surface of the copper, it is still easy to wear off. In addition, the surface of ceramic PCB is not flat enough. The conductor will be higher than the ceramic substrate by about 0.035 mm. This could cause the pin to get stuck during rotations, and the uneven surface would accelerate the wearing of the metal. Another problem of a ceramic PCB-based pad is its cost, which is much higher than that of a stainless steel-based pad. Therefore, Design II, which uses stainless steel to replace the ceramic PCB, has been proposed.

3.3.3.3 Design II: pin (rotation part) + pad (stainless steel)

In Design II, the pad and pad holder have been redesigned. As shown in Figure 3.18, the conductor of the pad is made of stainless steel, while the isolator is made of high-temperature epoxy or ceramic glue. A mold is required to shape the epoxy. The two protrusions on the top and bottom will be welded with the pad holder. Laser machining is then used to cut the connections (two red lines). The encoding region is on the pad, while the ground region is on the pad holder. As such, the two regions are electrically isolated by the epoxy. When the pin touches the conductor (isolator), the signal and ground ports will be short-circuited (open-circuited), respectively.

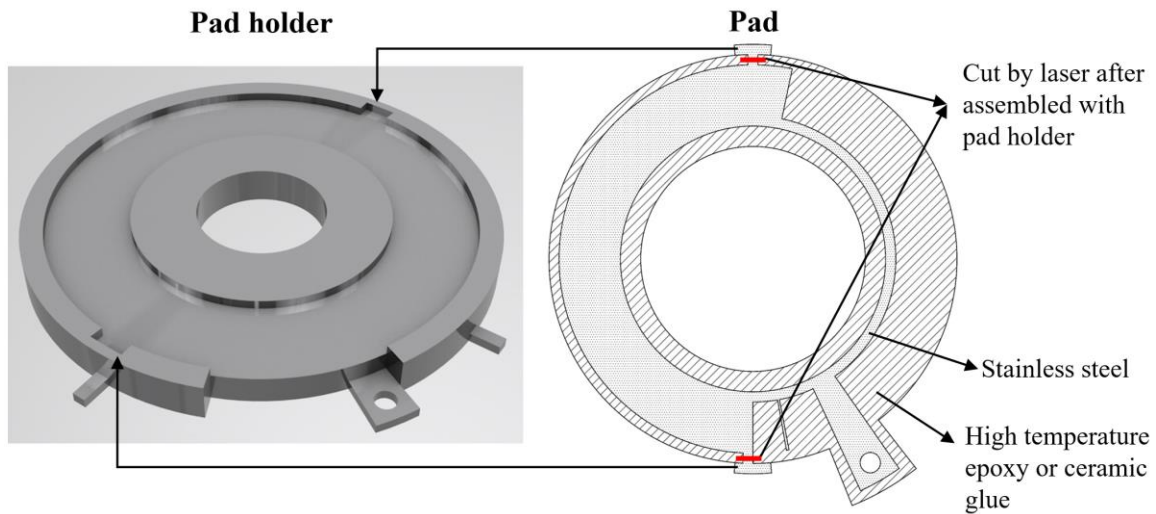


Figure 3.18 The pad and pad holder in Design II. The pad is composed of stainless steel and high-temperature epoxy or ceramic glue. A mold is required to shape the epoxy. The two protrusions on the top and bottom will be welded with the pad holder. Laser machining is then used to cut the connections (two red lines). The encoding region is on the pad, and the ground region is on the pad holder.

Drawbacks of Design II: The fabrication process of the pad is difficult to operate.

The epoxy has to fully cover the bottom, inner, and outer sides of the stainless steel. If the stainless steel were to touch the pad holder, it would prevent the reader from getting the correct digital states. In addition, the larger the area of the joint interface, the higher the probability of generating cracks or gaps. The relative position between the pad and pad holder becomes unstable under vibration. As such, the risk of obtaining erroneous readings is increased.

3.3.3.4 Design III: pad (rotation part) + pin (separated ground pin)

Several changes have been made in the third design to solve the problems in the previous designs.

- 1) As shown in Figure 3.19, a lid has been added at the top of the housing. A bearing will be assembled at the center of the lid. As such, the extended part of the housing to stabilize the shaft can be deleted. The overall height of the sensor can be decreased to 109 mm.
- 2) As shown in Figure 3.20, pads become rotating parts, which are connected to the shaft. Pins will be fixed with the housing. Meanwhile, signal wires will be soldered with pins.
- 3) As shown in Figure 3.20(a), the pins to contact the ground region have been separated out. The ground pin is placed on the top of the housing and contacts the shaft.
- 4) As shown in Figure 3.21, Teflon becomes the material for the pin holder. It provides electrical isolation between the signal and ground wires.

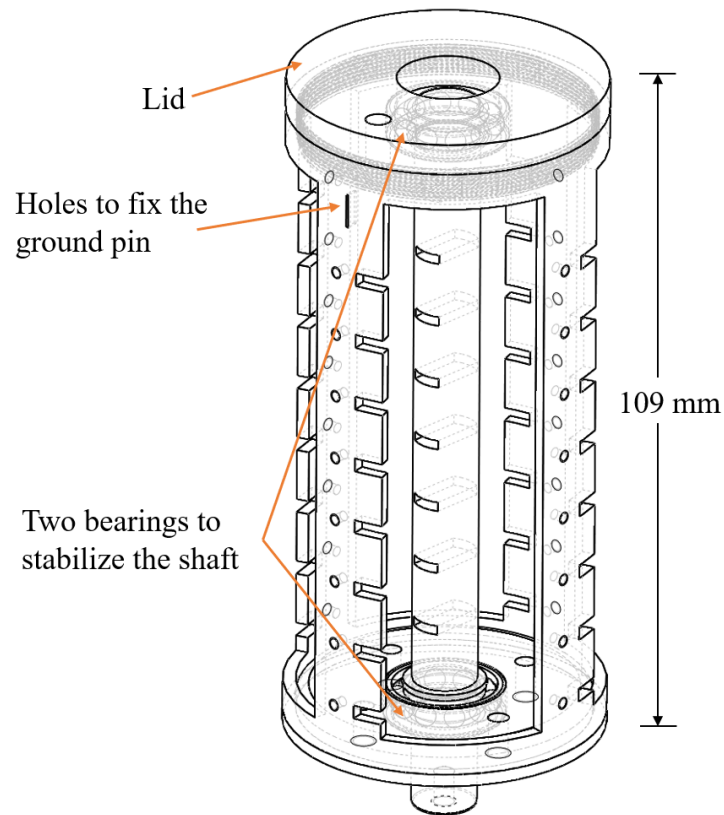


Figure 3.19 The assembled housing, lid, and shaft in Design III. The lid is assembled by the inner threads on the top of the housing. Two bearings are used to stabilize the shaft. The extended part of the housing in the previous designs has been deleted. The overall height of the sensor is 109 mm. The diameter remains the same as that of the previous designs.

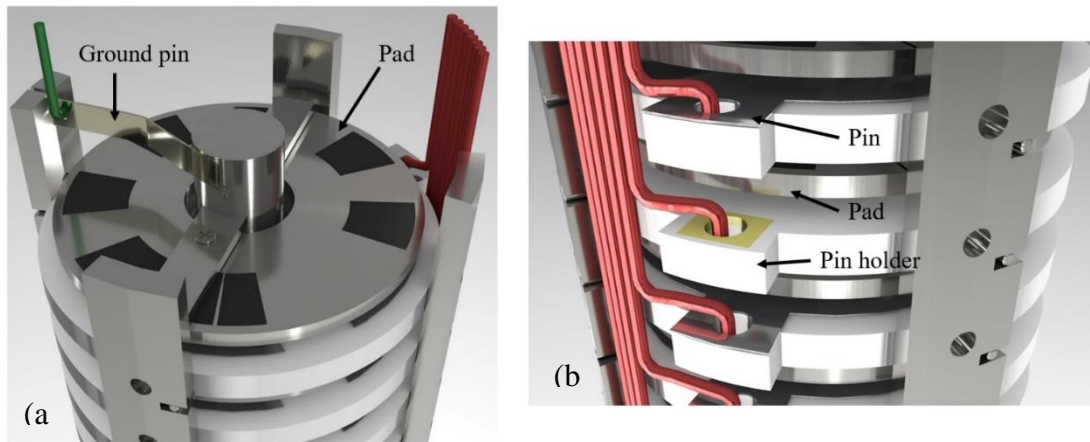


Figure 3.20 (a) The ground pin is assembled within the notch of the housing and contacts with the shaft. The pad is assembled with the shaft by a rectangular plug. (b) The stacked relationships between pins and pads have changed. Signal wires are soldered with pins. The yellow area on the pin holder is the thermal isolation material, such as the ceramic. It is used to protect the pin holder from high temperatures during the soldering process.

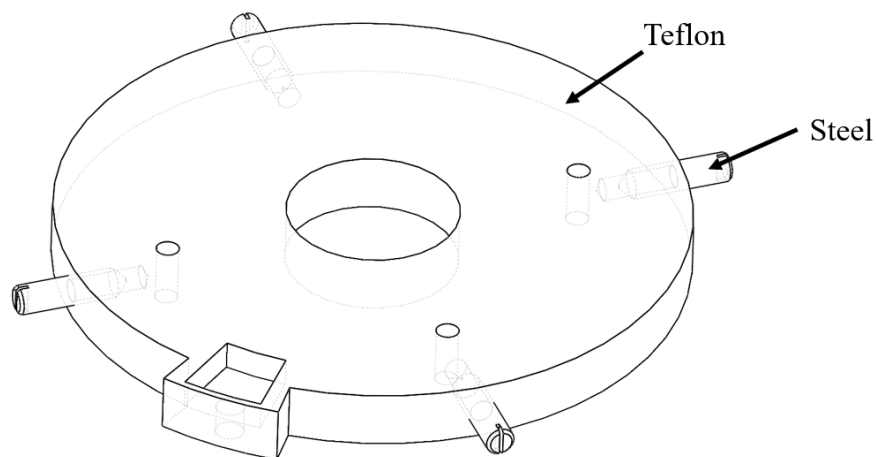


Figure 3.21 3D model of pin holder. The main body of the pin holder is made of Teflon. The four screws are made of steel and assembled by the threads. As in Design I, the four screws will be used to connect the pin holder to the housing.

Figure 3.22 shows the fully assembled all-digital sensor, in which a rotation stage has been connected at the bottom of the sensor. By using the stage to control the rotation angles, the pads and pins can be aligned. The assembly process has been software simulated and recorded in a video, which can be accessed by the following link:

[https://drive.google.com/file/d/1EXaqx2NWPc-](https://drive.google.com/file/d/1EXaqx2NWPc-3DZD67FfHkdhCK0C2E3up/view?usp=sharing)

[3DZD67FfHkdhCK0C2E3up/view?usp=sharing](https://drive.google.com/file/d/1EXaqx2NWPc-3DZD67FfHkdhCK0C2E3up/view?usp=sharing) Fig. 15 shows the fabricated pins. The other parts in Design III are still under fabrication.



Figure 3.22 3D model of fully assembled all-digital sensor from Design III. The rotation stage connected to the shaft is used for alignment of the pads and pins.

3.3.3.5 Fabrication of encoding pad

The encoding pad is composed of conducted and insulated areas, which are used to generate different digital states (“1” and “0”). One major requirement for the encoding pad

is its surface should be as flat as possible so that frictional wearing is minimized when the pin is sliding along the pad. I used stainless-steel as conductors because it has high corrosion resistance. As for the insulator, there should be no holes on the surface. The material should have a high operation temperature (larger than 250 °C). Plus, the thermal expansion coefficient (TEC) of the insulator should match the stainless-steel's TEC.

A high-temp epoxy (FH8732) was used to fabricate the encoding pad. The CTE of FH8732 matched well with the stainless steel. It has an operating temperature of up to 260 °C. Figure 6(b) shows the fabricated encoding pad after testing at 250 °C for four hours. There are no large air bubbles shown on the surface of the epoxy. The bonding between stainless steel and epoxy was also found very stable. The basic procedures of fabricating the encoding pad are described below. 1. Clean the stainless-steel pad and thaw the epoxy at room temperature for 15 mins. 2. Fill the epoxy in the silicone mold and push the stainless-steel pad to the bottom of the mold. 3. Vacuum pump the epoxy for 15 mins and cure the epoxy at a temperature chamber. 4. Polish off the extra epoxy. 5. Use drill to remove the epoxy inside the threaded holes. 5. Fine polish the surface of the encoding pad using silicon carbide sandpaper of up to 1200 grit.



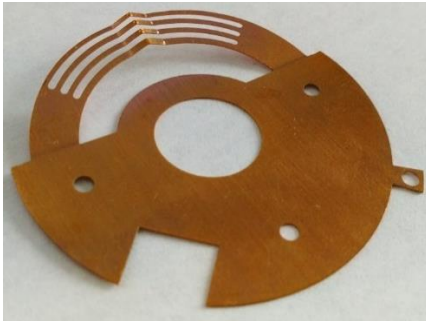
(a)



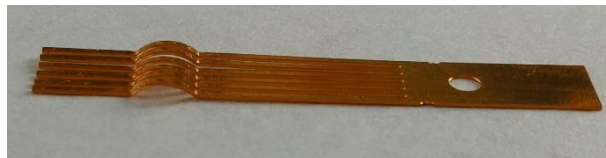
(b)

Figure 3.23 (a) Encoding pad fabricated using stainless steel and high-temp epoxy FH8732. (b) The pad was tested at 250 °C for four hours then cooled down to room temperature. No cracks were found in the dried epoxy after the high temperature test.

3.3.3.6 Fabrication of contact pins



(a)



(b)

Figure 3.24 Pictures of fabricated (a) signal pin and (b) ground pin and.

The contact pins are made of beryllium bronze. Figure 3.24 shows the picture of the fabricated ground pin and signal pin. To reduce the friction force of the digitizer, The contact pins were fine polished using a hand-hold polisher. Figure 3.25 shows the microscope images of the contact pin before and after polishing.

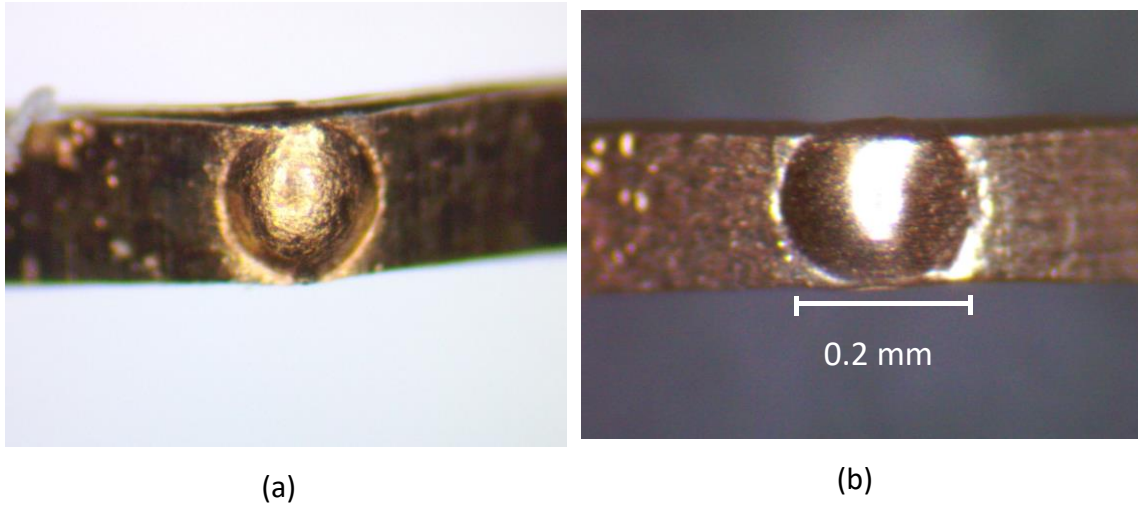


Figure 3.25 Microscope images of the contact pins before (a) and after (b) polishing.

Figure 3.26(a) shows the contact pin was soldered with a high temperature electrical wire using high-temperature solder and then fixed on the Teflon plate by three screws. The melting point of the high-temperature solder is higher than 250°C . A clip was applied to provide additional fixations for the electrical wire. Figure 3.26(b) shows three pins contacted with their corresponding encoding pads to interrogate the digital states. A multipurpose grease with a service temperature of 260°C was also applied between pads and pins to reduce the friction forces.

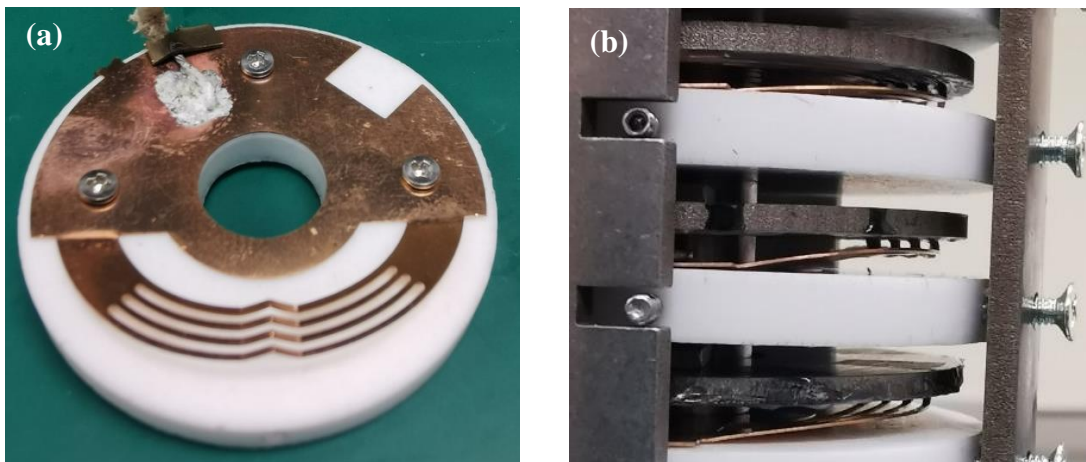


Figure 3.26 (a) A contact pin connected with an electrical wire using high-temperature solder and fixed on a Teflon plate by three screws. (b) Pins contacted their corresponding encoding pads.

3.3.3.7 The alignment of the digitizer

There are two targets in the alignment process. 1. The initial states (angles) of different bit channels should be the same. 2. The contact pin and encoding pad should be aligned to have the same rotation center. The biggest challenge for the sensor alignment is that we can not visually observe the pin and pad's relative position because of the stacked structure. Therefore, we proposed an approach to calculate the misalignment direction from the digital state reading results.

The experiment setup is shown in Figure 3.27. A motorized rotation stage and a motor controller were used to provide a reference rotation angle. The digitizer's shaft was connected with the rotation stage, and the outer frame was clipped by two screws attached to the optical table. A total of nine wires (one for ground and eight for encoded channels) were connected to the interrogation module, which was used to continuously read the 8-bit digital numbers. The interrogation module comprised a pull-up circuit and a microcontroller (STM32). During the test, the rotation stage was controlled to have a constant rotation speed of 2 degrees per second, and the microcontroller was also controlled to have a constant reading speed of 10 times per second. If the digitizer was well aligned, we could obtain a similar number of readings at each digital state, and the digital states should have a linear relationship with the reference rotation angle. By comparing the difference between actual reading results and the ideal case, we can figure out the

misalignment direction between each channel's pin and pad.

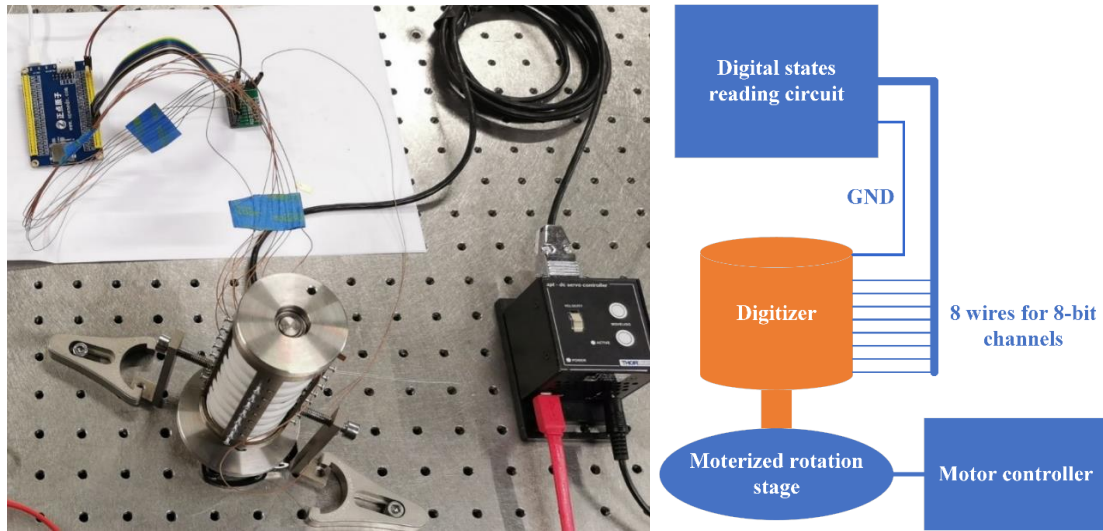


Figure 3.27 Experiment setup to test the digitizer.

We will take the 7th bit and 8th bit (least significant bit, LSB) as examples to demonstrate the proposed method. Figure 3.28 shows the dimension of the 8th-bit encoding pad. The enlarged picture shows the index of conductors (C_i) and insulators (I_i), respectively. There was a total of 200 digits encoded within the angle of 300 degrees. One digit took 1.5 degrees. Because the contacting width between pad and pin can not be zero, we applied a bias angle of 0.3 degrees to compensate for this effect. As such, one digit of the conductor takes 1.2 degrees, and one digit of the insulator takes 1.8 degrees. If the pin and pad are correctly aligned, the number of readings at each conducted or insulated segments can be expressed as

$$\begin{aligned} N_8 &= (\theta \pm \theta_{bias}) r / v \\ &= (1.5 \pm 0.3) 10 / 2, \end{aligned} \quad (3.1)$$

where θ is the angle for one-bit number, θ_{bias} is the biased angle, r is the reading rate, v is the rotation speed. Figure 3.29(a) shows the difference between the calculated number of

readings and the tested results. The difference is bouncing between positive and negative values. This result may be caused by the over biasing of the bit angle. Figure 3.29(b) shows the test results when we decrease the bias angle from 0.3 degrees to 0.15 degrees. The differences have vastly decreased. The maximum difference is limited in the range of ± 3 , which could be caused by some system errors, such as the rotation speed and reading rate were not precisely equal to the assigned value. Considering one digit should have a 7.5 number of readings, ± 3 should be an acceptable alignment error.

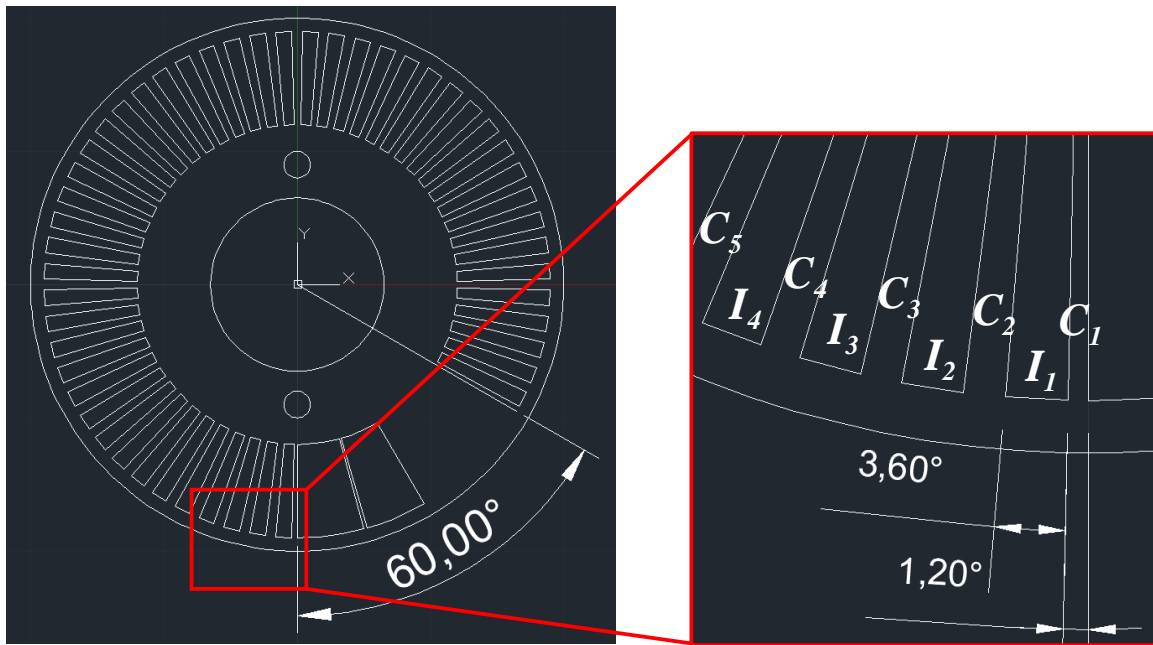
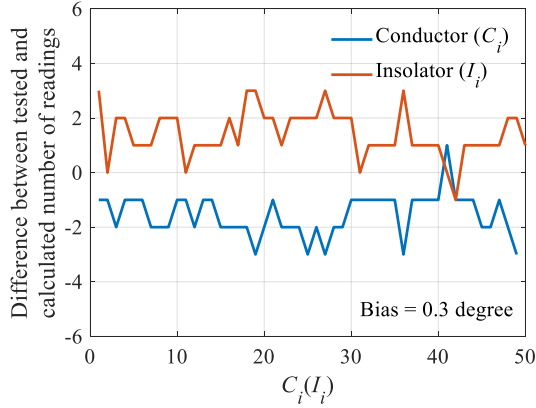
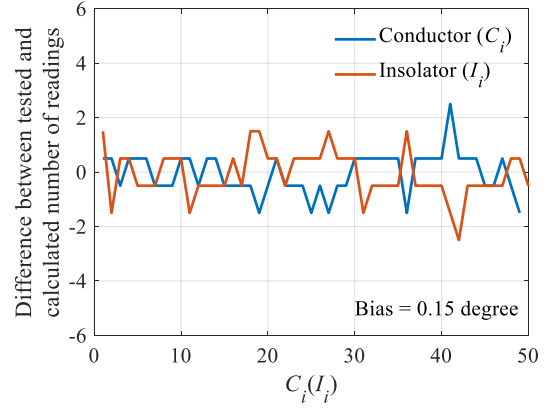


Figure 3.28 The dimension of the 8th-bit encoding pad.



(a)



(b)

Figure 3.29 Test results of the 8th-bit channel with a bias angle of (a) 0.3° and (b) 0.15°.

Figure 3.30(a) shows the testing results of the 7th-bit channel. The curve for the conductor is above the curve for the insulator when the indexes are lower than 10 and higher than 15. Two curves are around zero when the indexes are within the range of 10 to 15. This phenomenon can be explained using the two extreme cases shown in Figure 3.30(b). In case 1, when the rotation angle is perpendicular with the misalignment direction, the number of readings at the conductor segments are much larger than at the insulator segments. However, in case 2, when the rotation angle is parallel with the misalignment direction, the number of readings at both segments should be approximately the same. As such, the angle that two curves are around zero should be the angle that points to the misalignment direction.

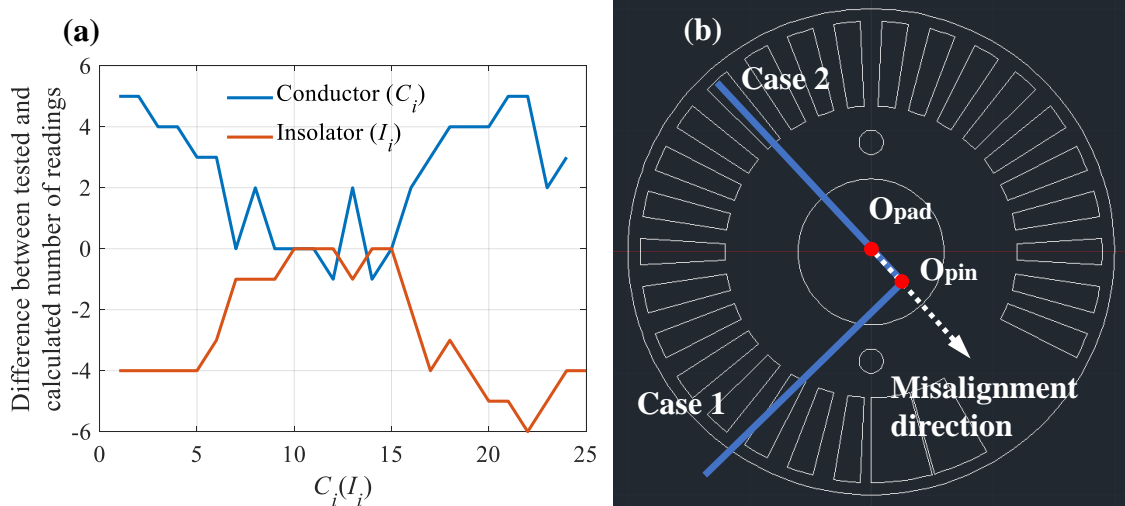


Figure 3.30 (a) Test results of the 7th-bit channel. (b) Two extreme cases when the centers of pad and pin are not aligned. O_{pad} is the rotation center of the pad, and O_{pin} is the rotation center of the pin.

3.3.3.8 Testing of the assembled digitizer

Angle resolution test. The test results of the digitizer after alignment are shown in Figure 3.31, where the digital outputs (i.e., the bit numbers) follow linearly with the increase of the rotation angle. The maximum deviation between the test data and the ideal value is 1.67. The root-mean-square error (RMSE) of the test data is 0.51.

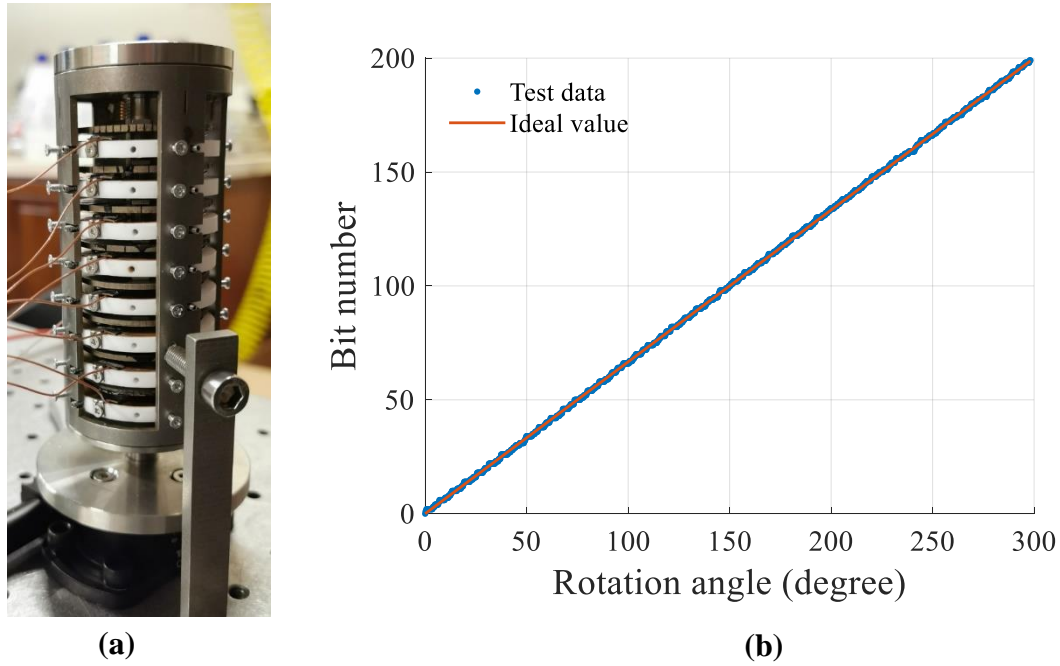


Figure 3.31 Calibration of the digitizer. (a) Picture of the experiment setup, (b) Digitizer outputs as a function of the rotation angle.

Long-term stability test. The long-term stability of the digitizer was tested under simulated conditions. As shown in Figure 3.32 (a), (b), and (c), the digitizer was sealed inside a pressure vessel and then placed in an environmental chamber to conduct the long-term stability test. The temperature of the environmental chamber was set at 150°C. Figure 3.32(d) shows the long-term stability test results of the digitizer. The test duration was 580 hours, which exceeds the required duration of 400 hours. The contacting resistance of each bit channel was measured every minute. The threshold of separating digital states “0” and “1” was set to be 8 k Ω . The output was digital “0” if the contact resistance is below 8 k Ω , while the digital state was “1” if the contact resistance is above 8 k Ω . As shown in Figure 3, the contact resistances of all bits have been about 8 Ω all the

time, which is a thousand times below the threshold of 8 k Ω . There were no erroneous readings for the test duration of 580 hours, which proves the digitizer has excellent long-term stability at high temperatures.

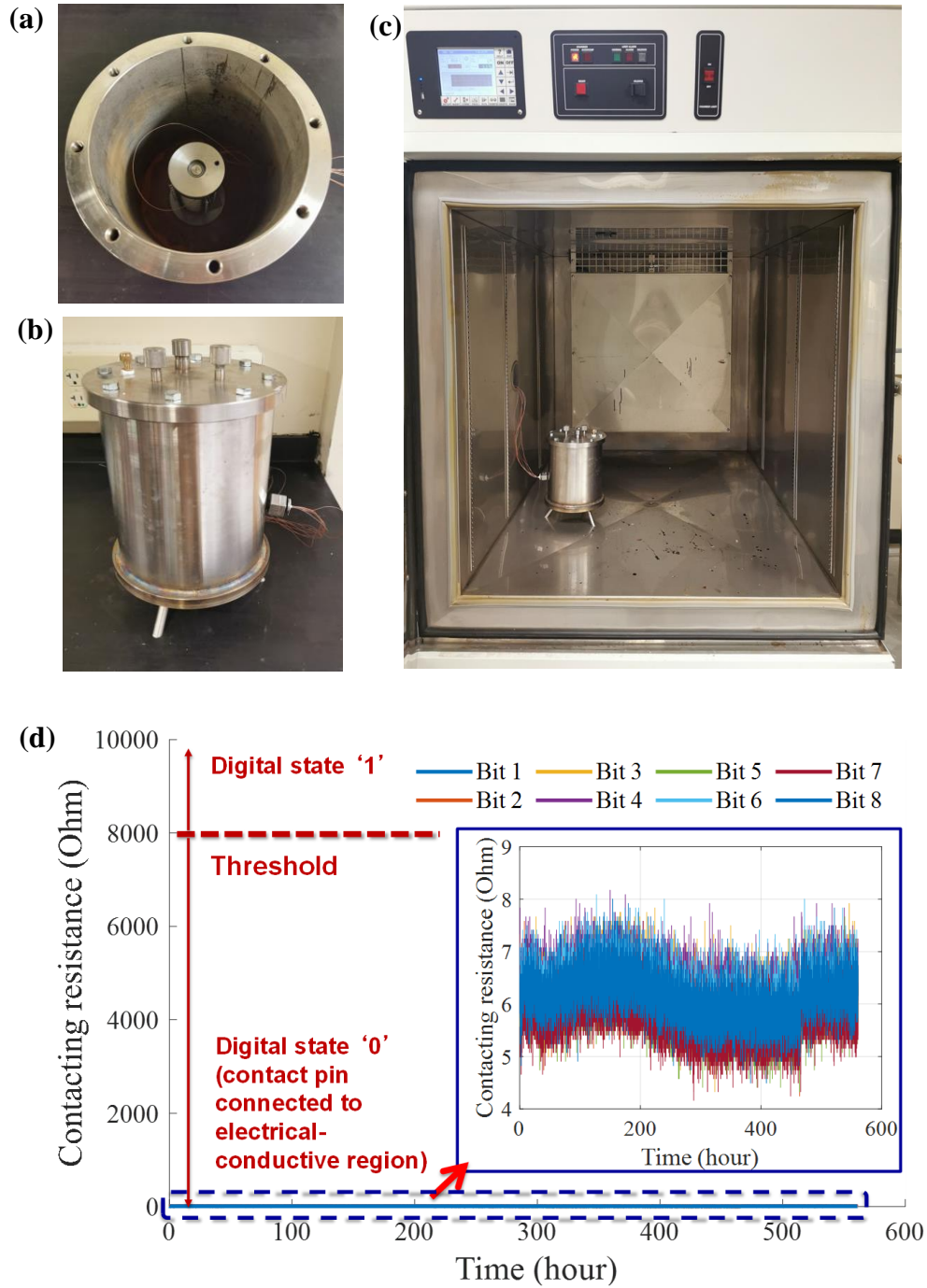
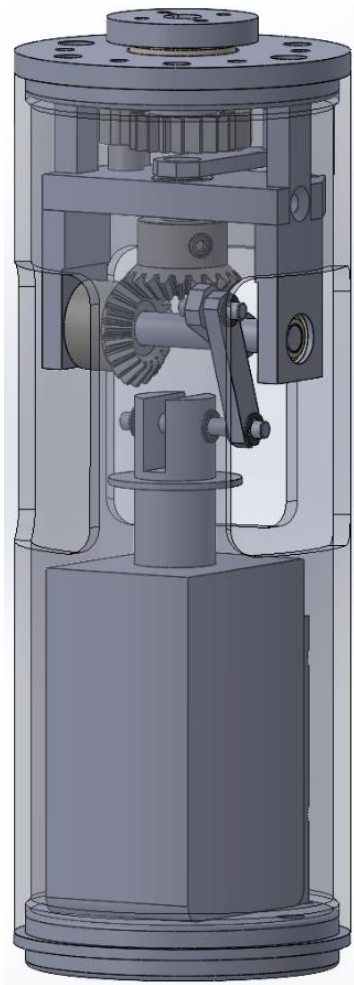


Figure 3.32 Long-term stability test of the digitizer. (a), (b) and (c) pictures of the test setup showing the digitizer placed inside an environmental chamber; (d) Contacting resistances between contact pins and encoding pads of the 8-bit digitizer as a function of time.

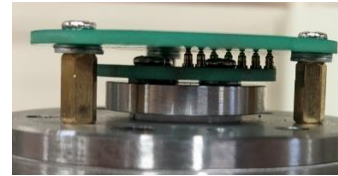
3.3.4 Multiplexing module



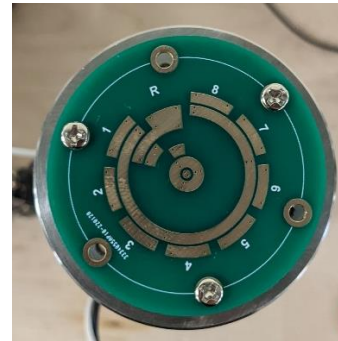
(a)



(b)



(c)



(d)



(e)

Figure 3.33 (a) Solidworks design model of the multiplexing module. (b) Fully assembled multiplexing module. (c) Details of the contacting pins. (d) Details of the encoding patterns. (e) Details of the miter gears and the ratcheting gear.

The sensor multiplexing function is achieved by an electromagnet-based multiplexing module. Figure 3.33(a) shows the 3D model of the multiplexing module. Figure 3.33(b) and (e) show the pictures of the fully assembled multiplexing module. The electromagnet is powered by a constant current source and controlled by a relay switching array. Two 90-degree miter gears and a ratcheting gear are used to convert the linear motions to unidirectional rotation movements. By powering on and off the electromagnet, the contacting pins can rotate to different encoded positions on the pad, as shown in Figure 3.33(c). Figure 3.33(d) shows the encoding pattern of the pad. Positions 1 through 8 are connected to the 8-bit digitizer. Position “R” is used to connect the power supply to the next cascaded sensor module so that multiple sensors can be multiplexed. Once the reading of all sensors is completed, a reset command will be issued to move all the contacting pins to their initial status. To ensure the multiplexing module is working properly, it’s essential to rotate the contacting pins $360/9 = 40$ degrees per operation (powering on and off the electromagnet). As such, the contacting points are positioned at the center of each encoded bit. The use of ratcheting gear plays a vital role in eliminating accumulated errors. The rotation angle of each operation is independent of the previous operation.

Figure 3.34 shows the wiring of the multiplexing module to the surface instrument. There are 3 wires coming in and 4 wires coming out of the first sensor. Begin from the

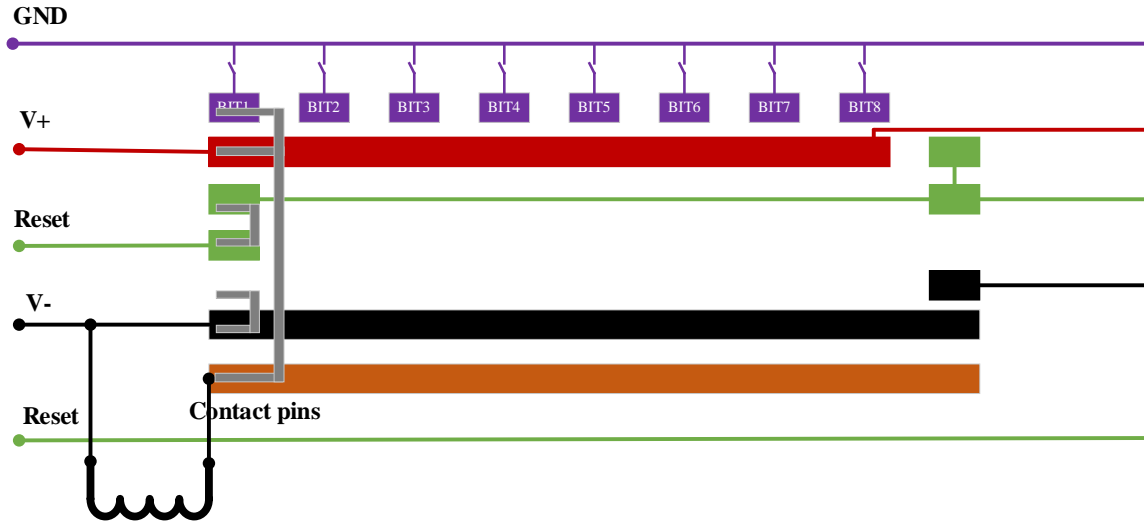
second sensor, there are 4 wires coming in and out of each sensor. There is a “Reset” wire coming out of the last sensor and the “Reset” wire is directly connected to the controller on the surface.



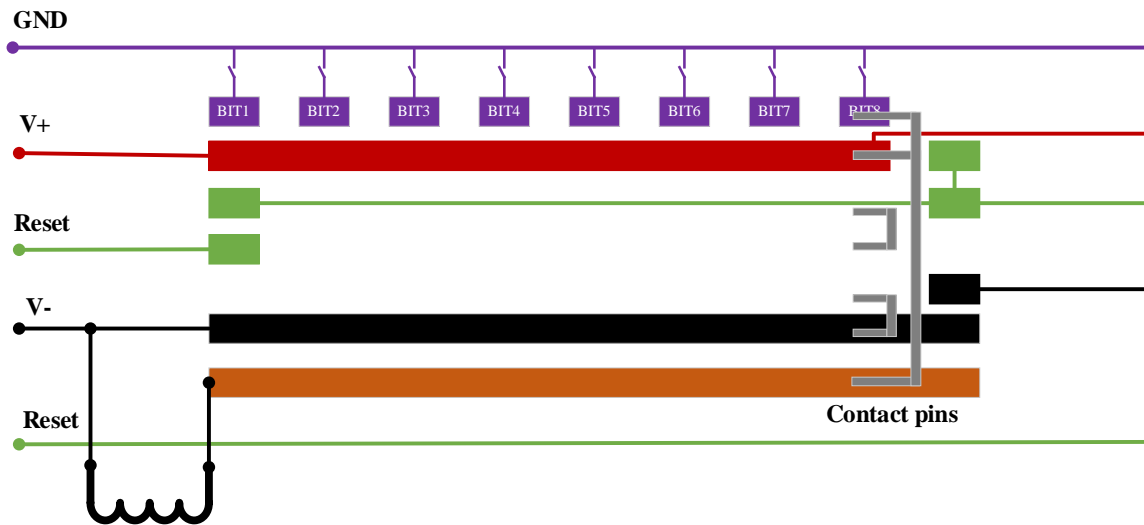
Figure 3.34 Wiring of downhole pressure sensors.

Figure 3.35 shows the working principle of the multiplexing module. The outermost channel on the encoding pad is connected to the sensor output. By testing the connectivity between wire “V+” and “GND”, we can obtain the binary readings of the 8-bit channels of the sensor. The two electrodes of the electromagnet are connected to the black and brown channels (the innermost two channels). When the sensor is at the initial state (Figure 3.35(a)), by powering the electromagnet via “V+” and “V-”, the electromagnet will drive the contact pin to rotate through the 8-bits, one-by-one. Figure 3.35(b) shows the situation where the contact pin is reading the last bit of the sensor, i.e., the 8th bit. Upon finishing reading the last bit, the contact pin moves to the next position (Figure 3.35(c), reset state), where the “V+” wire is disengaged from the current sensor but is connected to the next sensor. At this state, the connectivity between “V+” and “GND” represents the first bit of data of the next sensor. Because the “V-” wire is also connected to the next sensor, when we power on the “V+” and “V-” wires, the contact pin of the next sensor will rotate. After we read the last serially connected sensors, all the sensors will reach the reset state. From the last sensor, by applying a voltage between the “Reset” and

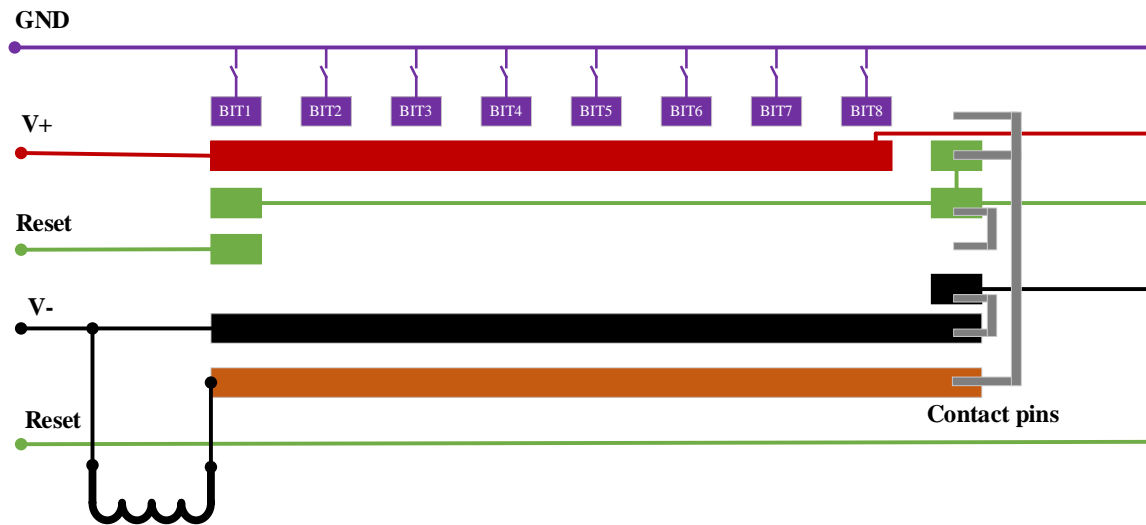
“V-” wires, all the contact pins will return to the initial state. After resetting all the sensors, the reading sequence is ready to engage a new reading circle.



(a) Initial state of reading the i -th sensor.

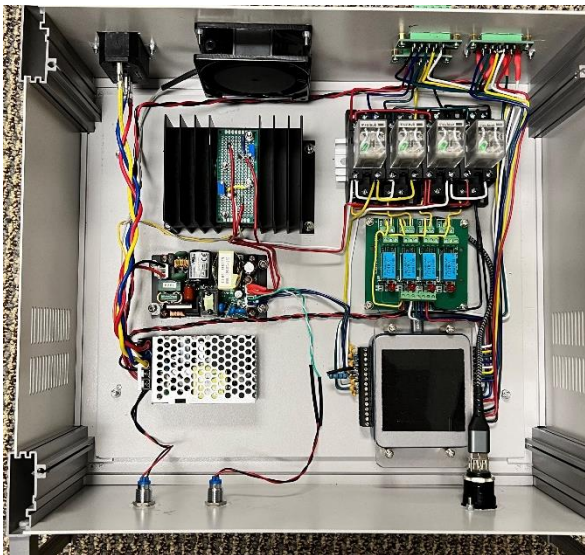


(b) Reading the 8th bit of the i -th sensor.



(c) Reset state of the i_{th} sensor and initial state of the $(i+1)_{th}$ sensor.

Figure 3.35 Working principle of multiplexing module.



(a)



(b)

Figure 3.36 Pictures of the inside (a) and outside (b) of the developed surface instrument to drive the multiplexing module.

Figure 3.36 shows the portable surface instrument to drive and read the multiplexing module. The instrument is composed of a power supply, a constant current source, a data acquisition (DAQ) module, and a relay-based switching array. The constant current source is used to power the electromagnet. The DAQ is used to control the switching array so that the reading, multiplexing, and resetting commands can be issued and executed. Figure 3.37 shows the GUI of the sensor reading software. The main operations include a) selecting the DAQ device, b) setting the number of sensors, c) reading the sensors automatically or manually, d) displaying the system status, and e) reading data displaying and saving.

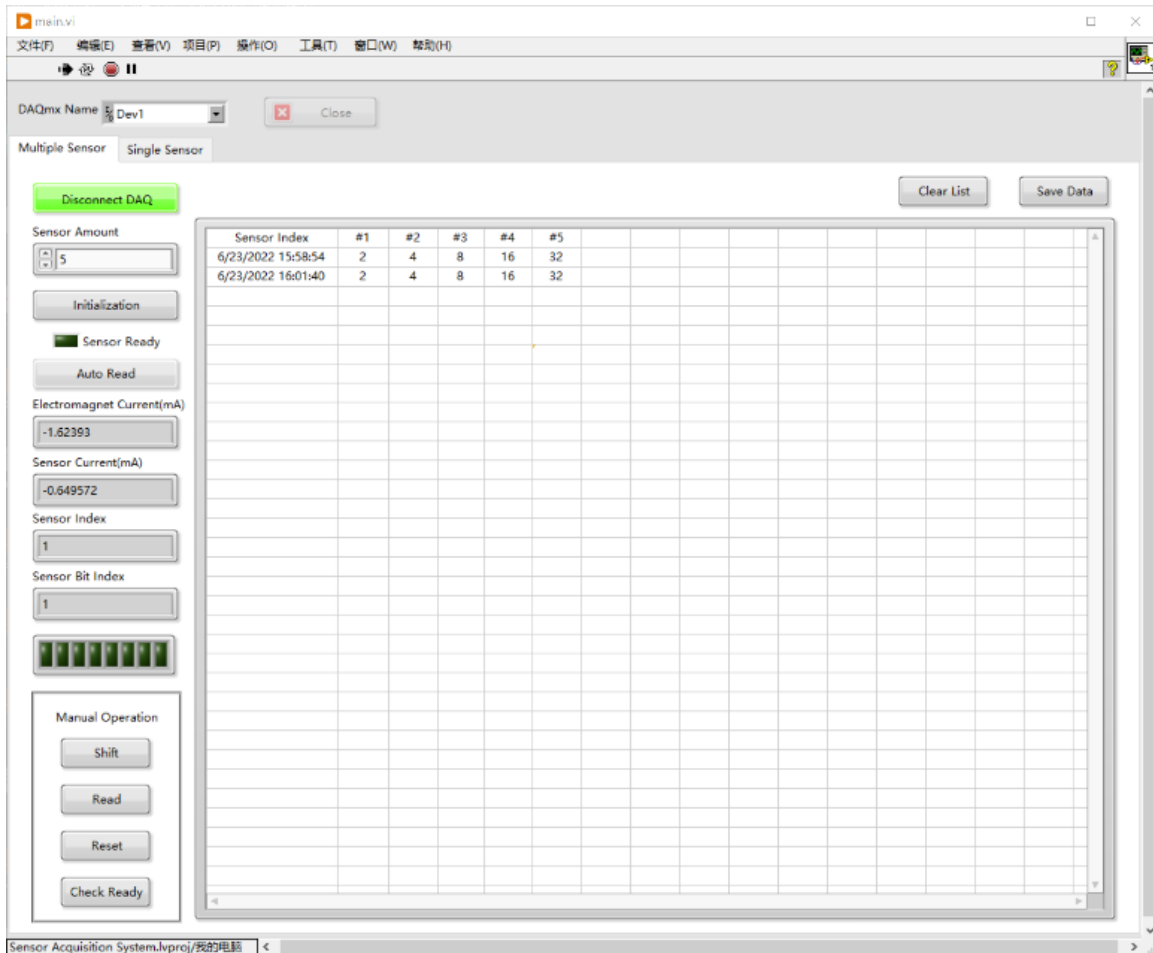


Figure 3.37 Graphic user interface (GUI) of the control software.

Figure 3.38 shows the experimental setup to test the multiplexing modules and the sensor reading instrument. A laptop was used to communicate and control the instrument. Five multiplexing modules were connected in serial and interrogated by the instrument. A breadboard circuit was used to simulate the 8-bit binary inputs from the sensor digitizers. The test results are shown in Figure 3.37. Five sets of 8-bit binary codes from the five cascaded sensors were successfully read by the sensing instrument. The multiplexing capability of the all-digital sensing system and instrument was experimentally validated.

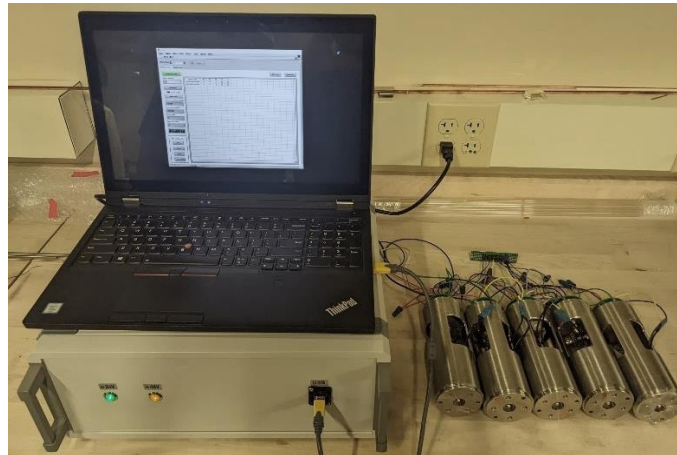


Figure 3.38 Picture of five multiplexing modules interrogated by the portable instrument.

3.3.5 Surface instrument development

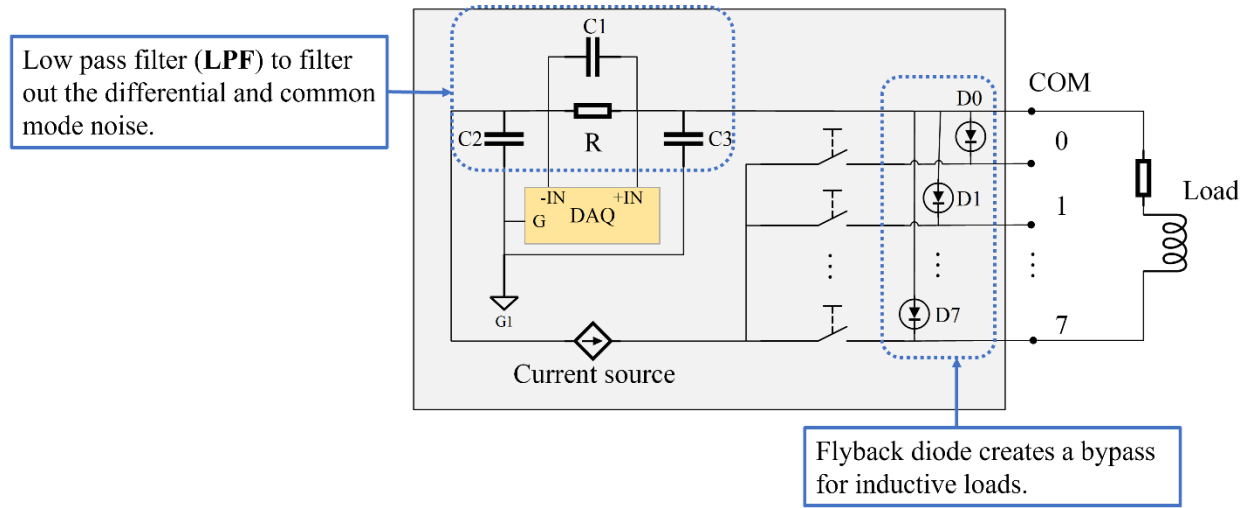


Figure 3.39 Circuit schematic of the surface sensor reading instrument.

The instrument is designed to read a single 8-bit digital pressure sensor using a constant current source. It has an 8-channel relay array, and a data acquisition module (DAQ) to read multiple multiplexed sensors. The circuit schematic is shown in Figure 3.39. The relay array is controlled by the digital output ports of the DAQ. By switching the current source to the bit channels 0 through 7, the DAQ can obtain the voltage across the sampling resistor. The output of the current source was set to be 22.3 mA, and the sampling resistor was 220 ohms. As such, the input signal of the DAQ should be about 0 V for open circuit and 4.9 V for short circuit. Figure 2 shows the inside picture of the fully assembled instrument. About 500-ft 28-AWG and 1000-ft 32-AWG wires were connected to the instrument for testing its performance. Figure 3.41 shows the test results. The y-axis is the input voltage, and the x-axis is the number of samples. The results indicate that the instrument has a signal-to-noise ratio of about $52 \text{ dB} = 20 \log_{10} 4.895/0.012$.



Figure 3.40 Picture of the surface sensor reading instrument.

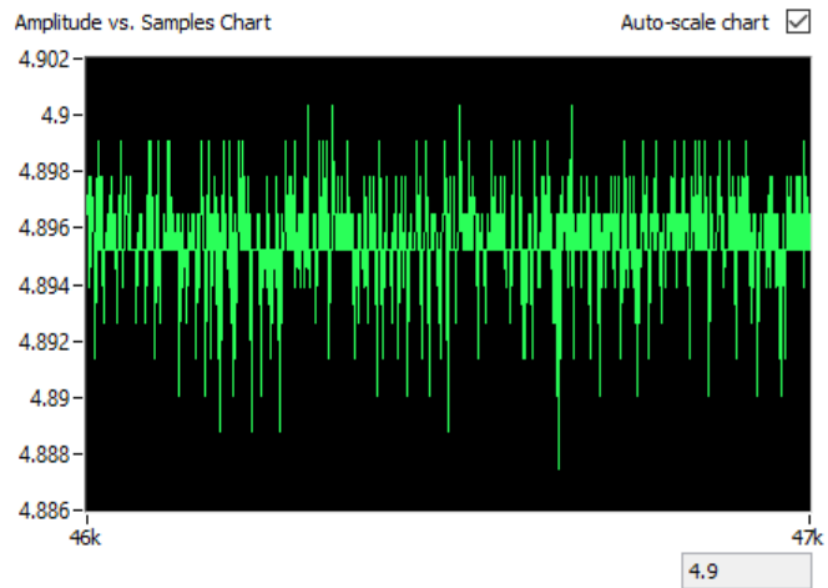


Figure 3.41 SNR test results of instrument.

3.4 Laboratory test of the fully assembled downhole pressure sensor

Figure 3.42 shows the welding results among the shaft, beam, and the encoding pad. Figure 3.43 shows the assembled downhole sensor.



Figure 3.42 Arc welding among beam, shaft, and the encoding pad.

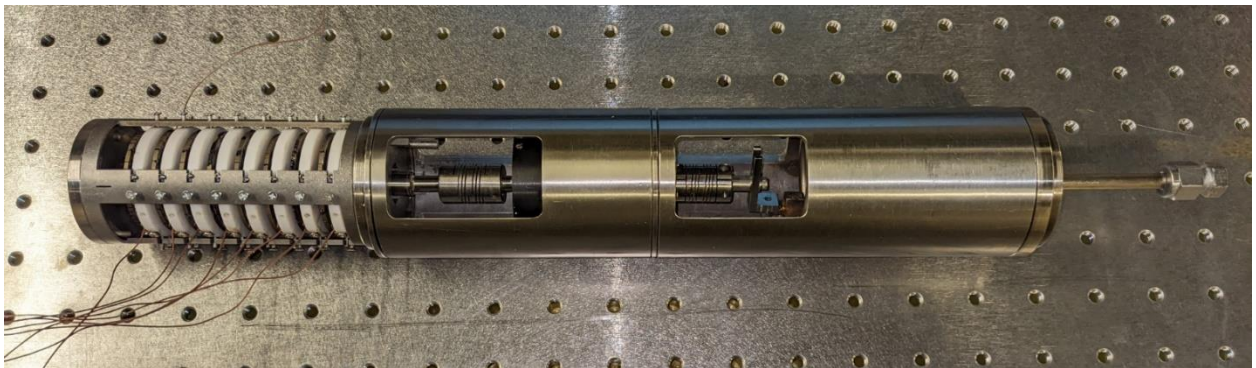


Figure 3.43 The assembled downhole sensor.

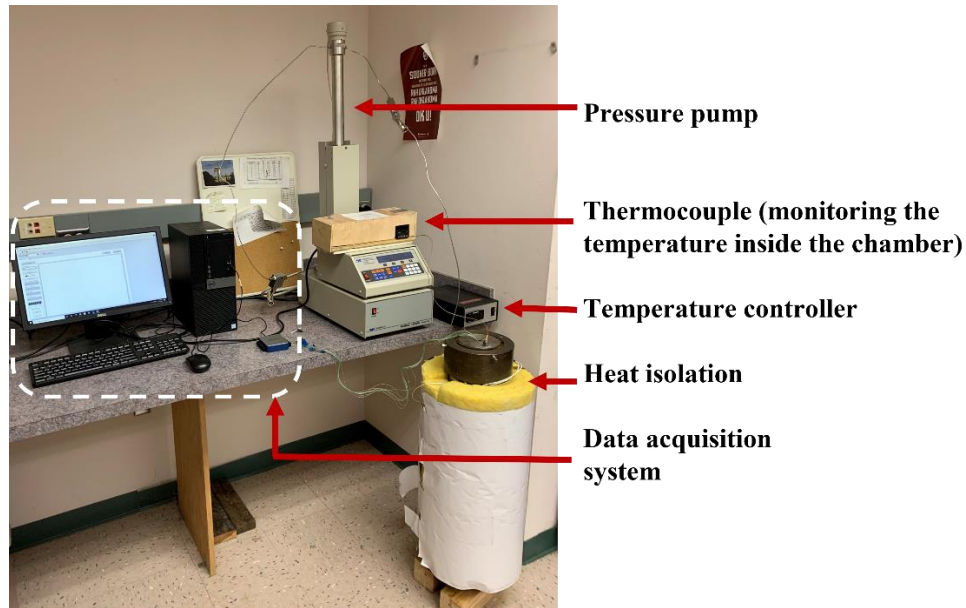


Figure 3.44 In-lab sensor test setup at OU.

The in-lab test setup is shown in Figure 3.44. A Teledyne-ISCO 100DX syringe pump generated pressures of up to 2,000 psi. The pump was connected to the chamber through a 1/8-inch inner diameter tubing with two pressure valves from Swagelok. The heating tape was rolled outside of the testing chamber to control the testing temperature. A DAQ was used to read the sensor. Figure 3.45(a) shows the all-digital sensor was assembled with the hematic housing and the chamber lid. Figure 3.45(b) shows the sensor's wires were coming out of the chamber lid through its center hole. And a thermal coupler was used to monitor the inner temperature of the testing chamber. The sensor was tested at 23 °C and 50 °C. The input pressure was increased from 0 to 2000 psi and then decreased back to 0 psi with an increment/decrement step of about 100 psi. The test results are shown in Figure 3.46. The pressure responses were similar at two testing temperatures. And the sensor was tested to have a linear response in the range of 0 to 2,000 psi. The sensor had

about 100 psi hysteresis (difference between pressure-increase and pressure-decrease response lines). This could be caused by the friction force between contact pins and encoding pads. One possible solution is to replace the contact pins with small bearings, which could neglect friction force while rolling on the encoding pad.

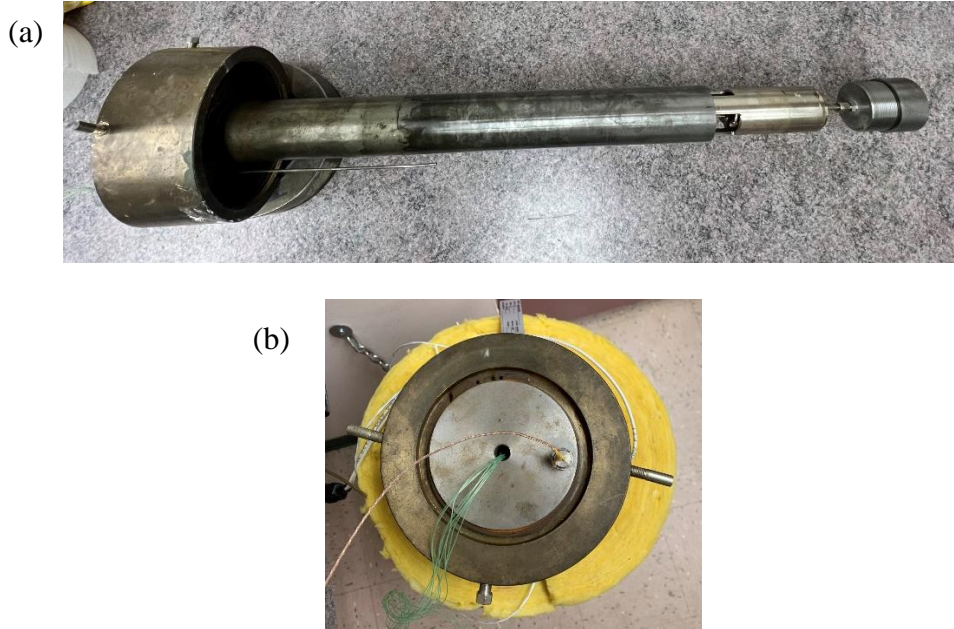


Figure 3.45 (a) All-digital sensor assembled with housing and testing chamber lid. (b)

Top view of the testing chamber.

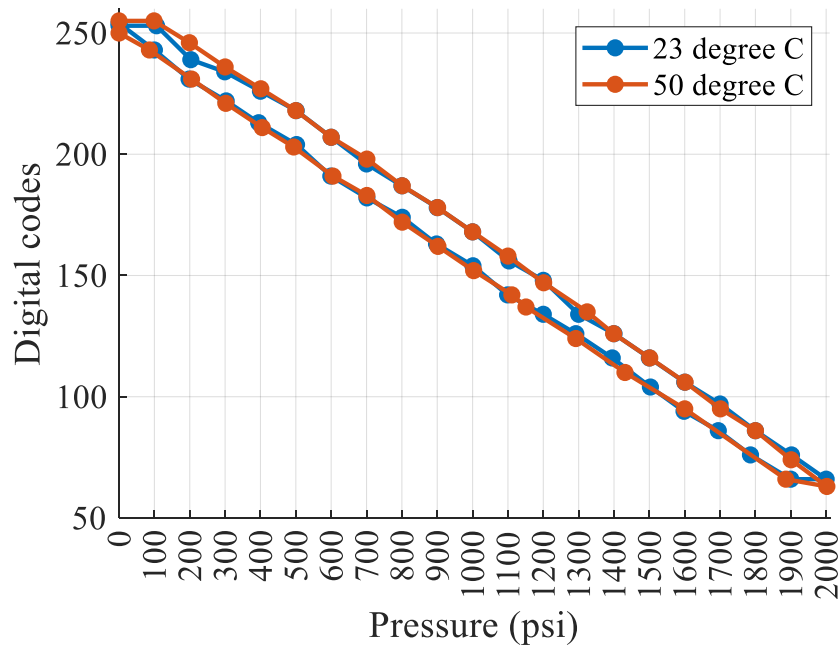


Figure 3.46 In-lab pressure testing results at different temperatures.

3.5 Field test of downhole pressure sensor at research wellbore

3.5.1 Sensor installation



Figure 3.47 The all-digital sensor and reference sensor were connected to their cables.

Figure 3.47 shows the sensor was connected to the cables and ready to be tested. The all-digital sensor and reference gauge were strapped to the second sucker rod inserted

into the wellbore. Zip-ties and metal band clamps were used to tie the sensor and the cable onto the rods. Figure 3.48 describes the sensor lowering process. We put 3 band clamps to fix the all-digital sensor, while we used 4 band clamps for the reference sensor. After putting on the band clamps, we also put the waterproofed tape to cover the outside of the sensor. The cables were attached to the rod using at least three zip-ties per rod. Each rod is about 25-ft long.

We measured the pressure when every 10 rods were lowered. Because the downhole environment was unstable, we could only put 104 sucker rods downhole. We decided to take out the last 2 rods for the tubing that we needed to place on the top of sucker rods. Thus, the depth of the sensor was about 2550 ft. The top end of sucker rod was connected to a capped piece of production tubing. And the cables were passing into the tube through two holes drilled on the side wall of the tubing. J-B Weld was then used to seal the tubing cap, as shown in Figure 3.49. And a 24-hour cure time was taken before the pressure tests. Two cables were then connected to the surface instruments placed in the doghouse. The setup is showing in Figure 3.50. The surface instrument was able to read the sensor during the entire process of sensor installation and lowering into the research wellbore.

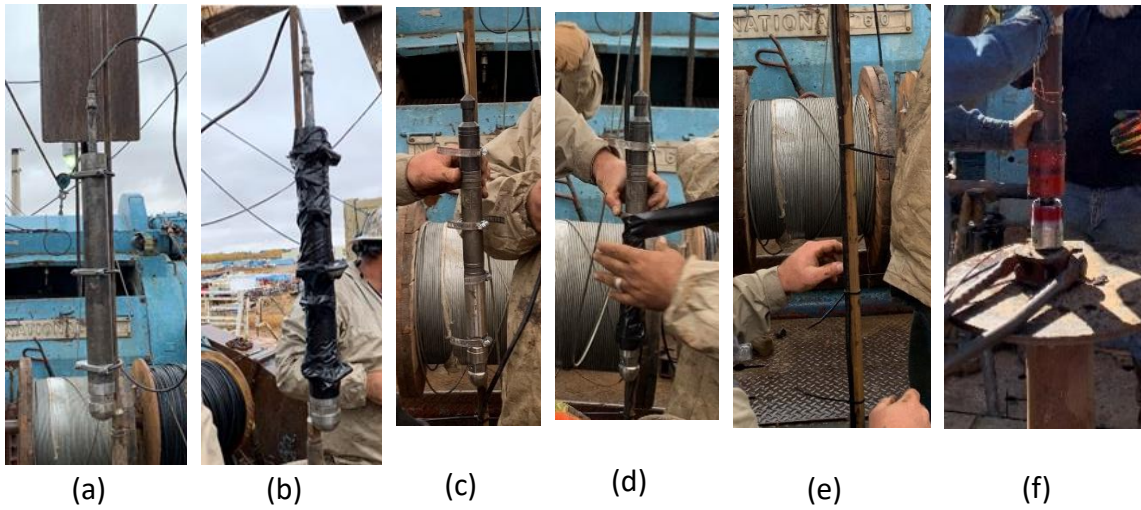


Figure 3.48 (a) The all-digital sensor was attached to the suck rods by three band clamps. (b) and covered by waterproofed tape. (c) The reference sensor was attached to the suck rods by four band clamps and (d) covered by the waterproofed tape. (e) Two cables were fixed to the sucker rods using zip-ties. (f) A production tubing was placed on the last rod.



Figure 3.49 Tubing cap with the cable pass through.



Figure 3.50 Surface sensor reading instruments setup.

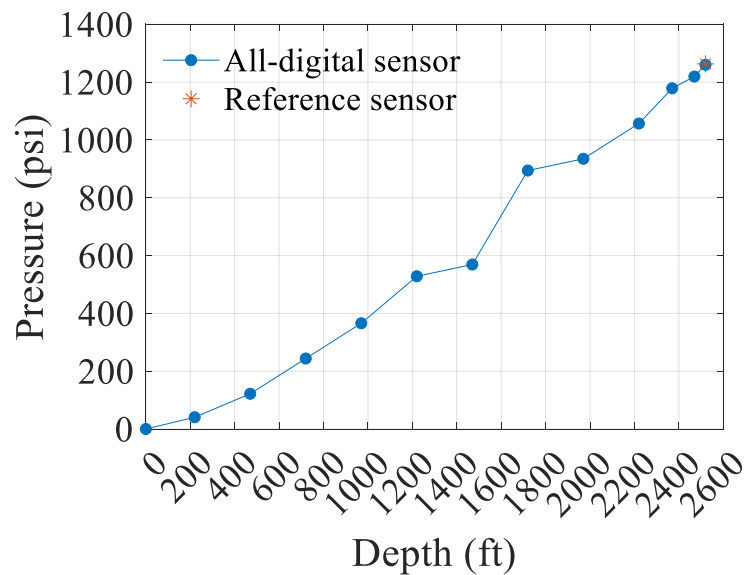


Figure 3.51 Testing data when all-digital sensor was lowering downhole.

The testing results when sensor was lowering downhole are shown in Figure 3.51. The pressure is linearly increased when the depth of the sensor increased. The measured pressure experienced an abrupt increasing around 1500 ft. This could be cause by the uneven distribution of the downhole fluid density. We stopped circulating the downhole

fluid after the drilling completed. During the time between the drilling and the sensor testing (about two weeks), the fluid may precipitate towards the bottom of the hole. Or some sands or rock may also be fallen from the side wall of the reservoir. All of those would cause the uneven distribution of the downhole fluid density. At 2550 ft, the measured data from the all-digital sensor matched well with the data from reference sensor. Figure 3.52 shows the test results of the long-term stability test. After sensor was installed, we used a pump to pressurize the reservoir at the surface and monitor the downhole sensor readings. The all-digital sensor responded correctly to the applied pump pressures. Over the two weeks long-term test, the sensor worked properly. Overall, the field test results proved that the developed downhole pressure sensing system worked properly and is capable to monitoring the downhole pressure variations.

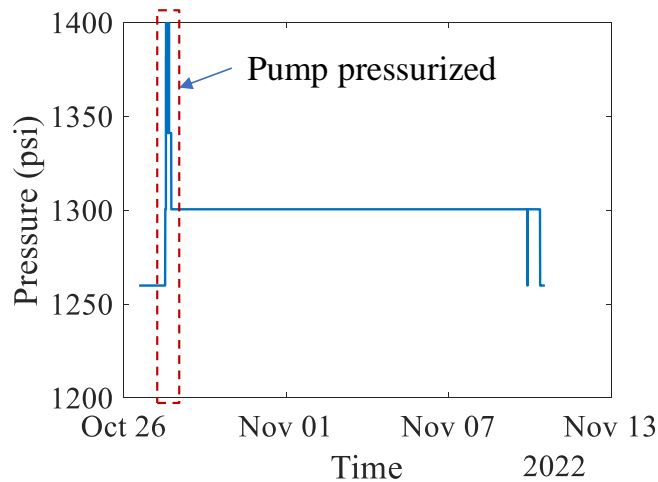


Figure 3.52 Long-term stability test.

CHAPTER FOUR

GLASS ADDITIVE AND SUBTRACTIVE MANUFACTURING OF A FIBER OPTIC ROTARY ENCODER FOR DOWNHOLE PRESSURE SENSING

4.1 Introduction

In the previous chapter, the all-digital sensing method and its implementation based on an electrical encoder was presented. One of the challenges that the system faced is the hysteresis problem induced by the electrical encoder. Hence, in this chapter, a noncontact-type optical encoder is developed to solve the hysteresis problem.

The Fiber optic sensors are competitive candidates for downhole pressure sensing because of their advantages of miniature in size, electromagnetic interference (EMI) immunity, high sensitivity, high-temperature resistance, and long reaching distance. Various optical fiber sensors have been proposed and successfully demonstrated for downhole pressure sensing, such as capillary encapsulated fiber extrinsic Fabry-Perot interferometric (EFPI) sensors [60]–[62], high birefringence fiber based Sagnac interferometer sensors [35], [63], FBG based temperature and pressure sensors [34], [64] and polarization modulation based high birefringence fiber sensors[36]. Because the optical fiber serves as both the measurement means and the telemetry channel, one of the challenges for the fiber optic sensor is to minimize the temperature-pressure cross-sensitivity and reduce the long-time drift. Several methods have been reported to compensate for the temperature influence by employing an in-line Fabry-Perot gratings (FBG) sensor[33], [60] or using the Raman scattering-based distributed sensor [62] for temperature sensing.

When using passive all-digital sensing method, a rotary encoder was connected to a bimetallic spiral to locally convert the analog temperature to a digital binary code [65]. As such, the data can be directly sent out in a digital format without using an analog-to-digital converter. By implementing this digital sensing approach to the downhole pressure sensor, the optical fiber is used merely as the telemetry channel to transmit the digital signals rather than active sensing elements. Therefore, the environmental variations (e.g., temperature and strain) caused long-term drifts of the optical fiber become negligible. Furthermore, compared to the analog signal, the nature of high SNR of the digital signal makes it suitable for long-distance telemetry.

Another challenge for optical fiber sensors is the packaging technique that can bond the fiber to the transducer and protect the fiber from breaking. Traditional methods, including using high-temperature epoxy or ceramic adhesive, have the problem of thermal expansion mismatching, which could lead to large signal drift or even structural failure at an elevated temperature. Fused silica, which has similar material properties to optical fiber, becomes an ideal choice for fabricating the fiber optic sensor's packaging structures. Recently, glass additive manufacturing utilizing the direct laser melting method has been demonstrated [66]. By integrating the picosecond laser-based subtractive manufacturing technique, the machining system offers great flexibility and simplicity to produce desired 3D structures with no post-treatment and high-temperature resistance. All-glass FPI sensor has been reported using this glass additive and subtractive manufacturing method for temperature [67] and pressure [68], [69] sensing.

The pressure change is first converted to the rotation angle of a Bourdon tube, which is then mechanically sampled by an optical rotary encoder. A stainless-steel encoding pad is fabricated by the picosecond laser blackening technique [70], [71]. The high fabrication precision of the picosecond laser enables micrometer-level code writing. The additive and subtractive manufacturing system is employed to embed optical fiber tips into a bulk fused silica glass to interrogate the encoding pad. The picosecond laser is used to fabricate the optical fiber embedded channels. Glass 3D printing technique is then used to seal the sensing fiber inside the channels. The integrated all-glass sensing head is finished by polishing the fiber tip surface to the design inclination angles to minimize the fiber tip reflection and maximize the SNR. The SNR, pressure response, and long-term drift of the fabricated prototype sensor will be experimentally tested.

4.2 Operational Principle

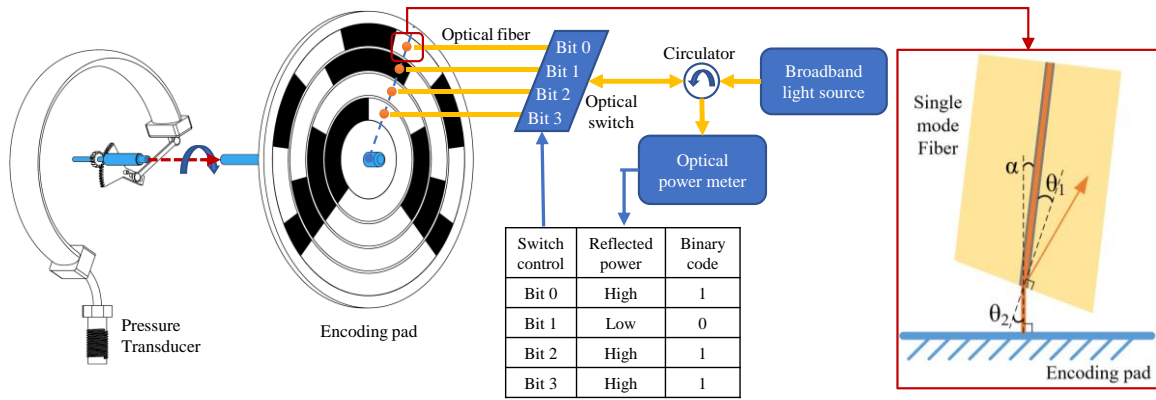


Figure 4.1 Operational principle of optical encoder based downhole pressure sensor. A Bourdon tube transduces the pressure to the rotation angle. The optical encoder transform the rotation angle into binary code. The black region on the encoding pad represents the low reflectivity region, while the white region has high reflectivity. Enlarged figure on the right: Optical path at fiber tip. The fiber end was polished to have an inclination angle of θ_1 .

The proposed pressure sensor consists of three parts: a Bourdon tube pressure transducer, an encoding pad, and a fiber optic interrogation system. Given different pressure, the Bourdon tube generates different rotation angles. The rotation angle is then transferred to the encoding pad, which connects to the center shaft of the Bourdon tube. Four optical fibers embedded in the sensing head are aligned to the center shaft but do not rotate. As shown in Figure 4.1, a 4-bit Gray coding is used to code the upper 3/4 part of the pad. The black area has low reflectivity, while the white area has high reflectivity. Four optical fiber end tips are aligned to four encoding channels, accordingly. A broadband light source is used to prevent light interference. The laser light passes through a circulator to an optical fiber switch. The optical switch connects to the optical fiber sensing head. The light is then reflected back from the encoding pad. The reflected light transmits through the optical switch and the circulator, and is received by an optical power meter. If the sensing head is pointed to the high reflection area (white area), we will receive high reflected power, which corresponds to digital state “1”. If the optical fiber pin is pointed to the low reflection area (black), we will receive low reflected

power, which corresponds to digital state “0”. For example, the rotated position, shown in Figure 4.1, would generate a binary code of “1101”.

Because the digital state is determined by the intensity of the reflected light, we need to increase the amount of the reflected light from the air-to-encoding pad interface and decrease the reflected light from the optical fiber-to-air interface. As such, the SNR can be maximized. The enlarged figure in Fig. 1 shows the diagram of optical path at the designed fiber tip. The fiber tip is polished to have an inclination angle θ_1 . The angle of the refractive light, which is the light emitted into the air, can be calculated using Snell’s law,

$$\theta_2 = \sin^{-1} \left(\frac{n_{fiber}}{n_{air}} \sin \theta_1 \right), \quad (4.1)$$

where n_{fiber} is the refractive index of optical fiber and n_{air} is the refractive index of air. In order to have the light vertically emitting to the encoding pad, the optical fiber should have an inclination angle of

$$\alpha = \theta_2 - \theta_1. \quad (4.2)$$

4.3 Sensor manufacturing

4.3.1 Optical fiber embedded all-glass sensing head

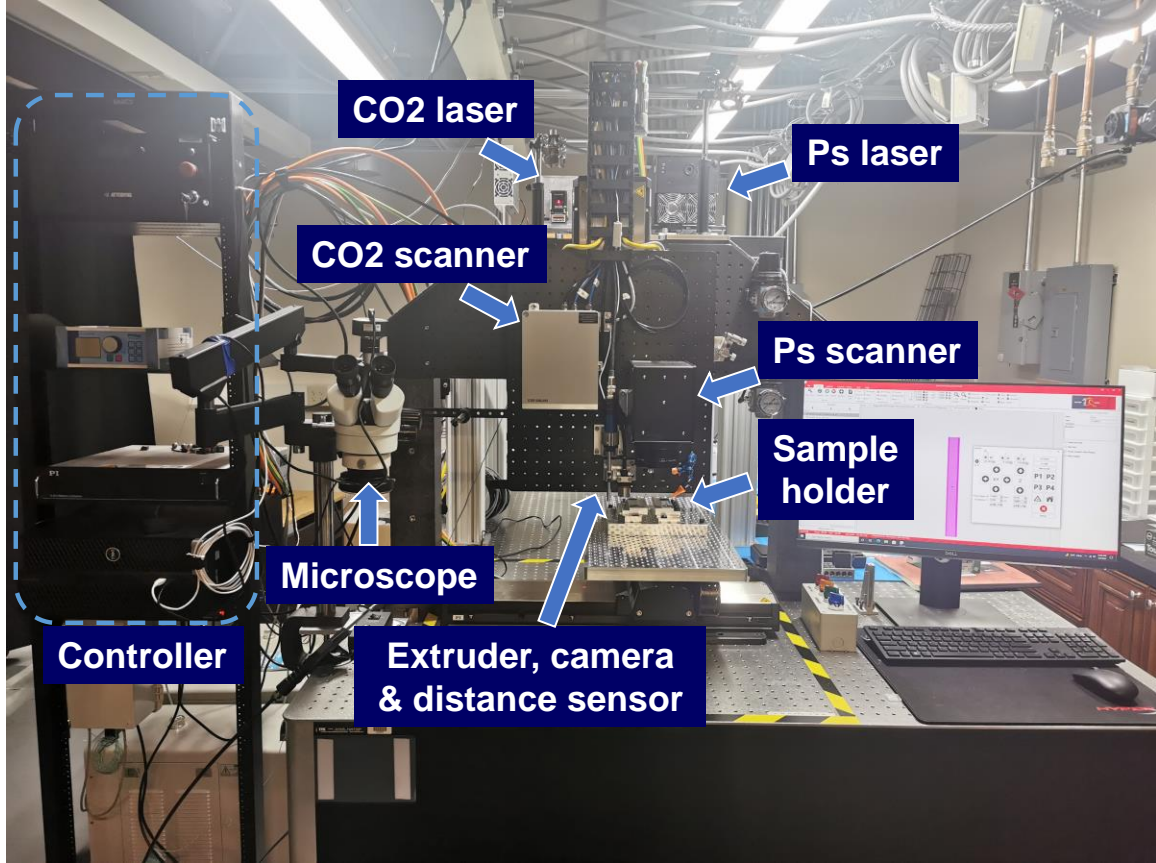


Figure 4.2 Glass additive and subtractive manufacturing system.

To realize the design shown in Figure 4.1, we plan to seal the optical fiber in a fused silica substrate using glass additive and subtractive manufacturing techniques. And then polish the bulk all-glass sensing head to the designed angles.

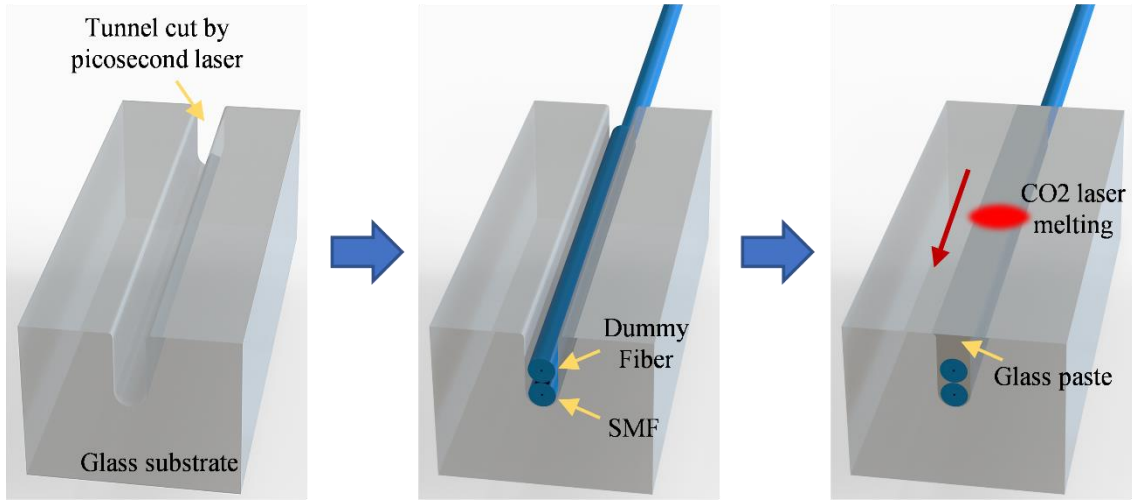


Figure 4.3 Procedure of packaging the sensing fiber into a bulk fused silica glass.

Table 4.1 Processing parameters for additive and subtractive manufacturing.

Parameters	Glass substrate	Glass paste melting	Stainless-steel laser
	cutting		blackening
Laser type	Ps laser	CO2 laser	Ps laser
Laser power	4W	10W	1.6W
Laser pulse repetition frequency	200kHz	-	100kHz
Laser spot scanning speed	300 mm/s	0.5 mm/s	15 mm/s
Hatching line spacing	0.025 mm	-	0.015 mm

As showing in Figure 4.2, the manufacturing system is mainly composed of a CO2 laser (Firestar ti100, SYNRAD Inc., with a wavelength of 1064 nm), a ps laser (APL-4000-1064, ATTODYNE Inc., with a wavelength of 1064 nm and a pulse width of 5 ps), and a paste dispersion system [66], [72]. The fabrication procedure is shown in

Figure 4.3. The fused silica glass substrate is first cut by the ps laser with the processing parameters shown in Table 4.1. Two single mode fibers (SMFs) are vertically placed inside the tunnel. The glass pastes [66] are extruded on top of the fiber through an extruder (eco-Pen300, Preeflow). The excess paste is then manually removed through a blade. CO₂ laser irradiation is conducted with optimized output power, scanning speed, and spot size to melt the glass paste with the substrate to seal the sensing fiber [67].

The fabricated tunnel has a width of 0.3 mm and a depth of 0.5 mm. The tunnel width is smaller than the CO₂ laser spot size (about 0.5-mm-diameter), so the laser can melt the glass paste and the substrate simultaneously to obtain better bonding results. The depth of the tunnel is large enough to bury two SMFs and prevent the sensing fiber from being melted. The dummy fiber, placed on top of the sensing fiber, is used to provide extra protection for the sensing fiber [72]. In addition, because the melting depth of the glass paste is influenced by laser power and scanning speed, the existence of dummy fiber also released the control requirements of the CO₂ laser parameters.

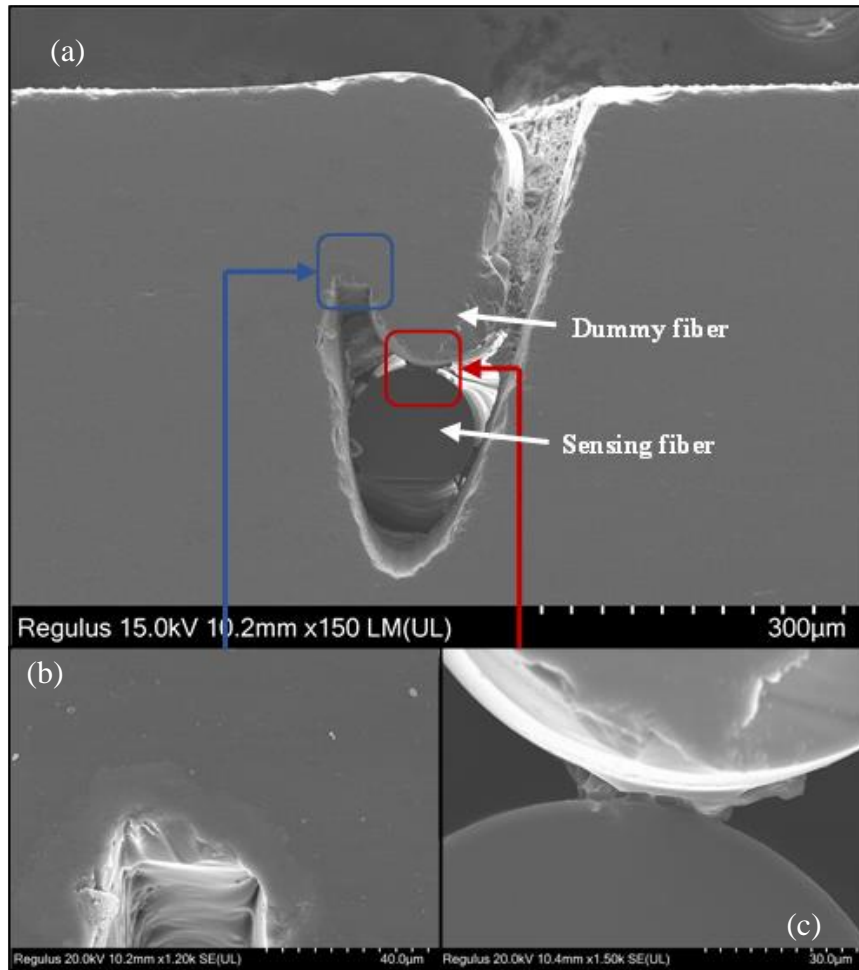


Figure 4.4 SEM images of the polished cross-section viewed 3D printed all-glass fiber head. (a) Overview. (b) Connection between the substate and the glass paste. (c) interface between the dummy fiber and the sensing fiber.

Figure 4.4 shows SEM images of the polished cross-section view of the all-glass sensing head. The dummy fiber was melted with the glass substrate. At the connection area, there is no micro crack. Therefore, the sensing fiber remains intact, which can be seen at the interface between the dummy fiber and the sensing fiber.

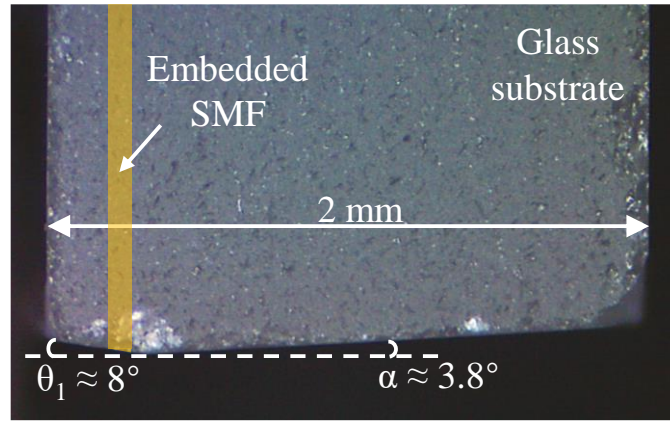


Figure 4.5 Side view of the polished all-glass sensing head.

After the optical fiber was sealed inside the glass substrate, we polished the fiber end surface. Two 3D-printed plastic polishing holders are fabricated using Formlab 2. The holder fixed the sensing head to the designed angle of $\theta_1 = 8^\circ$ and $\alpha = 3.8^\circ$ based on equations (1) and (2). Here we choose the fiber tip angle equal to 8° , which is similar to the FC/APC optical fiber connection. As such, an expected return loss should be around -60dB. The polished result is shown in Figure 4.5. The encoding pad should parallel the 3.8° polished surface.

4.3.2 Encoding pad

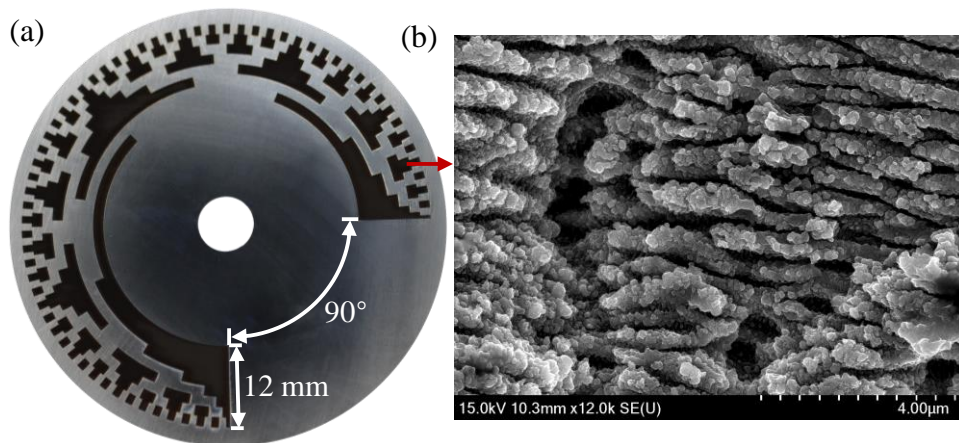


Figure 4.6 (a) Polished stainless-steel disc coded using picosecond laser. (b) SEM image of the blackened region.

The encoding pad is made of stainless steel. An 8-bit Gray code is fabricated using the ps laser blackening technique [70], [71]. The processing parameters are shown in Table 4.1. Figure 4.6(a) shows the fabricated encoding pad. The whole coding area occupied 270° with a single bit corresponding to $270/256 = 1.0547^\circ$. Each bit channel has a width of 1.5 mm. The outer diameter of the encoding area is 60 mm. Figure 4.6(b) is the SEM image of the laser blackened region. Generated ripples and valleys in the sub-micro scale increase the surface roughness and reduce the amount of light reflected back to the same angle as the incident direction.

4.4 Experiments

We conducted three experiments to demonstrate the proposed pressure sensor and verify its performance, including the SNR, pressure response, and long-time stability. We used a broadband light source (BBS 1550 A-TS, AFC TECHNOLOGIES Inc.) as the laser light source. The emitted light has a center wavelength of 1550 nm and a bandwidth of about 50 nm. The estimated coherent length is 15.3 μm . The optical fiber tip is about 200 μm to the encoding pad. As such, the reflected light from the fiber tip and from the encoding pad would not interfere with each other. We used a lightwave multimeter (Agilent 8163A with HP 81533B optical head interface) as the optical receiver.

4.4.1 SNR test

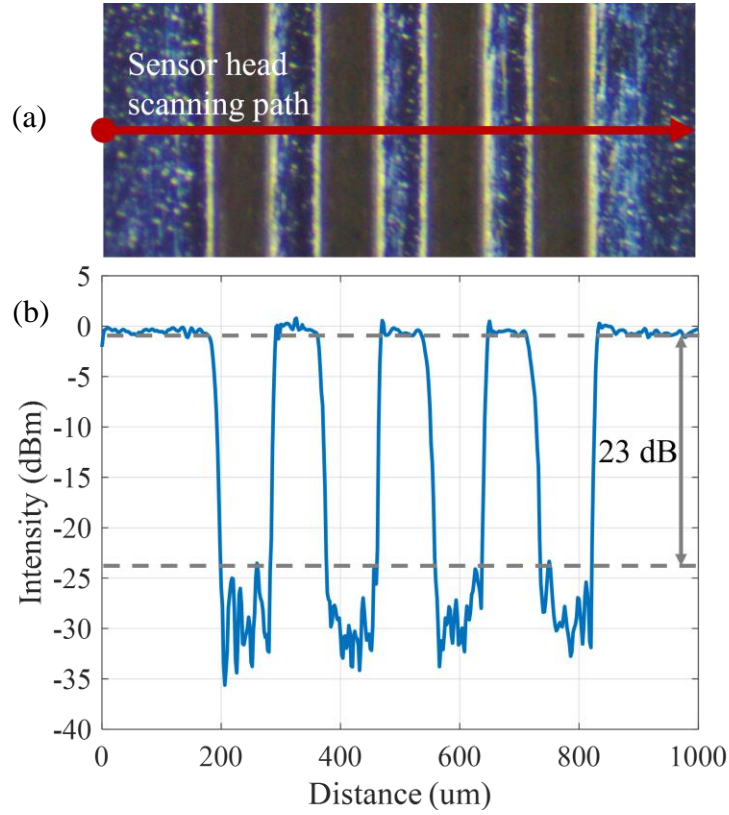


Figure 4.7 SNR test results. The optical fiber sensor head was scanning through four evenly distributed blackened region.

The proposed sensing system is first demonstrated using a single bit channel test. Four rectangular areas with a width of 100 um and an interval of 80 um were laser blackened using the same laser parameter listed in Table 4.1. The microscope picture of the pad is shown in Figure 4.7(a). The optical fiber sensing head was fixed on a motorized stage with an inclination angle of 3.8° . The sensing head scanned across the fabricated pad with a speed of 0.01 mm/s, while the optical power meter recorded the optical intensity readings with a sampling period of 0.2s. The test results are shown in Figure 7(b). When the sensing head moved on top of the un-blackened area, we received

high reflected light intensities larger than -1 dBm. When the sensing head moved on top of the blackened area, we received low reflected light intensities smaller than -24 dBm. Therefore, the system's SNR is around 23 dB. The average transition length, which is the distance from 10% to 90% of -1 dBm light intensities, is 8.5 μm .

4.4.2 Pressure Response

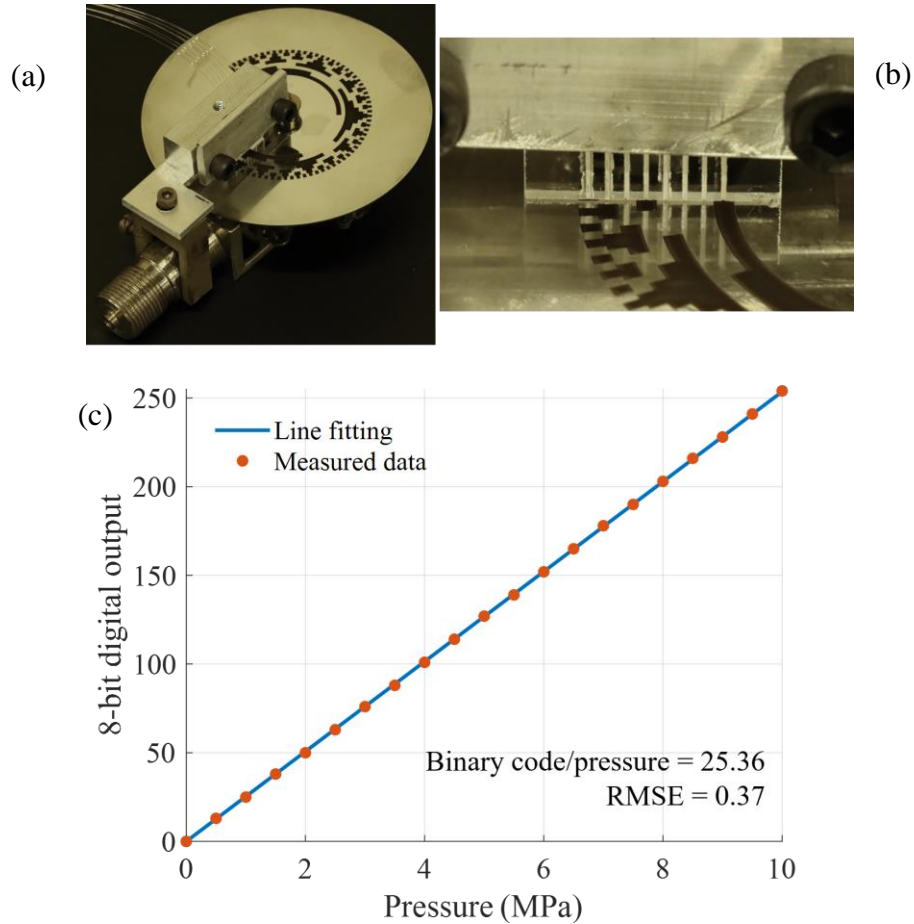


Figure 4.8 (a) Assembled pressure sensor. (b) Alignment between the optical fiber head and the encoding pad. (c) Pressure response test results.

Figure 4.8(a) shows the assembled pressure sensor. A commercially available Bourdon tube with a measurement range of 10MPa was assembled with the encoding pad

and the sensing head using aluminum structural pieces. Figure 4.8(b) shows the detailed view of the sensing head aligned to the encoding pad. A 1x8 bidirectional optical fiber switch was used to multiplex the eight sensing fibers. A deadweight tester (1305D, ASHCROFT) with a reference sensor (700G31, FLUKE) was used to test the proposed pressure sensor. An incremental of 0.5 MPa was applied to the pressure sensor from 0 MPa (atmospheric pressure) to 10 MPa. The measured data has an RMSE of 0.37 and a nonlinearity of 0.76 compared to the linear fitted line. In addition, there were no erroneous readings between the digital state “0” and “1”.

4.4.3 Long-Term Stability Test

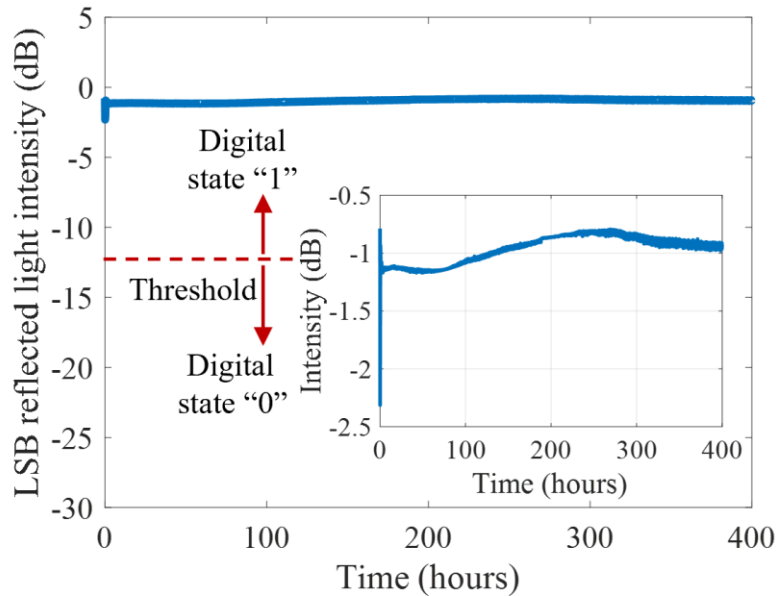


Figure 4.9 Pressure sensor test at 250°C for 400 hours.

The pressure sensor was placed inside the temperature chamber (DX 300, Yamato) to test its long-time and high-temperature drift. Figure 4.9 shows the test results of the last significant bit (LSB) of the optical fiber sensor head. The pressure sensor was tested at 250°C for 400 hours. At the beginning of the test, the received light intensity

experienced a 1.5 dBm fluctuation. Because the temperature is rapidly increased from room temperature to 250°C at the beginning of the test, the sensor head fixing structure could have a small distortion caused by the thermal expansion. The received light intensity tends to go back to its original value during the test. After being tested for about 250 hours, the reflected light gradually reduced. This could be caused by the oxidation of the encoding pad. The oxidation layer might deteriorate the encoding pad's surface reflectivity. However, the intensity fluctuations during the entire test are relatively small compared to the SNR. And the digital output code did not change during the 400-hour-test.

This long-time intensity fluctuations can be reduced by applying a layer of protective coating (e.g., gold coating) on the encoding pad. Because the coated material also can be ablated by the ps laser with high precision [73], we can use a similar method to fabricate the encoding pad. Moreover, the gold coating could improve the reflectivity of the pad, which can further improve the sensor's SNR.

4.5 Discussion

A prototype sensor has been demonstrated to prove the feasibility of the proposed sensing method. However, the sensor's performances, such as size and resolution, have not reached to their limitations. Here, we will establish a mathematical model to study the relationships between the sensor's performances and corresponding fabrication requirements, such as alignment accuracy, minimum bit width, and bit channel width, and evaluate the tradeoffs between the rotary encoder's size and resolution.

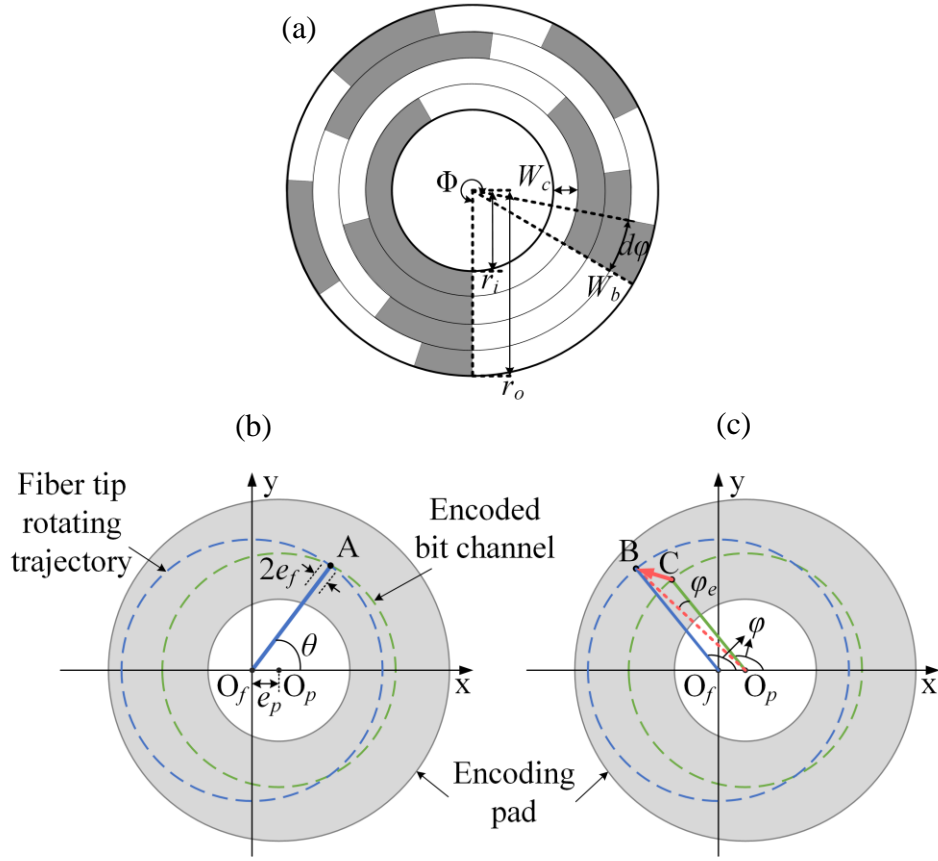


Figure 4.10 (a) Schematic of the encoding pad. (b) Initial alignment state. The fiber tip (blue solid line) is aligned to the encoding pad at point A. (b) Testing state. When the fiber tip rotates to point B, a misalignment angle of ϕ_e is generated. Φ , angles of the full encoded region; $d\phi$, angles of a single bit; r_i , inner radius of the encoding pad; r_o , outer radius of the encoding pad; W_c , bit channel width; W_b , minimum arc length of a single bit; O_f , rotation center and coordinate origin; O_p , encoding pad center; θ , initial alignment angle between fiber head and encoding pad; ϕ , rotation angle; e_f , the maximum misaligned distance at fiber tips; e_p , the misaligned distance between the rotation center and encoding pad center.

The schematic of the encoding pad and the relationship between the pad and fiber head are shown in Figure 4.10. Five boundary conditions need to be satisfied in designing the rotary encoder. First, the misaligned angle between the fiber head and encoding pad, φ_e , should be limited within the range of a single-bit code, $d\varphi$, so there will be no erroneous digital outputs. Second, the overall encoding angle, Φ , should be smaller than 2π . Third, the bit channel width, W_c , is equal to the interval of fiber tips. And the fiber tips need to have a separation distance that is larger than the CO₂ laser spot size, W_L . As such, W_c should be larger than W_L . Fourth, the minimum arc length of a single-bit code, W_b , should be larger than the transition length, W_T . Fifth, the outer radius, r_o , should be large enough to encode n-bit codes. So that we have

$$\begin{cases} d\varphi \geq |\varphi_e|S_e \\ 0 < \Phi = d\varphi \cdot 2^n \leq 2\pi \\ W_c \geq W_L S_L \\ W_b = d\varphi(r_o - W_c) \geq W_T S_T \\ r_o \geq nW_c \end{cases} \quad (4.3)$$

where S_e , S_L , and S_T are the safety factors.

First, we will calculate φ_e . As shown in Figure 4.10(b), there are two misalignments, including e_p , the distance between the encoding pad center and the rotation center, and e_f , the maximum misaligned distance at fiber tips. Because the bit channel width is much larger than the misaligned distance, the fiber tip will not move to the other bit channels. Hence, we ignore the misalignment in the radial direction. θ is the initial alignment angle between the fiber head and the pad. Different θ represents different relative positions between the fiber head and encoding pad.

As shown in Figure 4.10(c), when the fiber head rotates to an angle φ , it should turn to point C,

$$(X_C, Y_C) = (r \cos(\varphi) + e_p, r \sin(\varphi)), \quad (4.4)$$

where r is the radius of the encoded bit channel (green dash circle). However, due to the misalignment e_p , the fiber head rotates to point B,

$$(X_B, Y_B) = \left(R(\theta) \cos\left(\varphi \pm \frac{e_f}{R(\theta)}\right), R(\theta) \sin\left(\varphi \pm \frac{e_f}{R(\theta)}\right) \right), \quad (4.5)$$

where R is the radius of the fiber head rotating trajectory (blue dash circle). Because the arc length of φ_e is much smaller than the radius ($\varphi_e r \ll r$), it can be approximated as the tangential projection of vector \overrightarrow{CB} at point C. Therefore,

$$\varphi_e \approx \frac{\overrightarrow{CB} \cdot \overrightarrow{I_C}}{r} = \frac{e_p \sin(\varphi) + R(\theta) \sin\left(\pm \frac{e_f}{R(\theta)}\right)}{r}, \quad (4.6)$$

where $\overrightarrow{I_C} = (\cos(\varphi + \pi/2), \sin(\varphi + \pi/2))$ is the unit tangent vector at point C. Because $e_f \ll R(\theta)$, we have $\sin\left(\frac{e_f}{R(\theta)}\right) \approx \frac{e_f}{R(\theta)}$. As such

$$\varphi_e \approx \frac{e_p \sin(\varphi) \pm e_f}{r}. \quad (4.7)$$

According to Equation (4.7), φ_e is negatively proportional to the encoding radius, r . And θ has an ignorable influence on φ_e if the approximation conditions are valid. The maximum absolute value of φ_e should be obtained when $r = r_i$ and $\varphi = 90^\circ$ or 180° . By simplifying Equation (4.3) and substituting Equation (4.7), we have

$$\begin{cases} r_o \geq \frac{(e_p + e_f)S_e}{\Phi} 2^n + W_L S_L n, & \text{Cond. (a)} \\ r_o \geq \frac{W_T S_T}{\Phi} 2^n + W_L S_L, & \text{Cond. (b)} \\ 0 < \Phi \leq 2\pi, & \text{Cond. (c)} \end{cases} \quad (4.8)$$

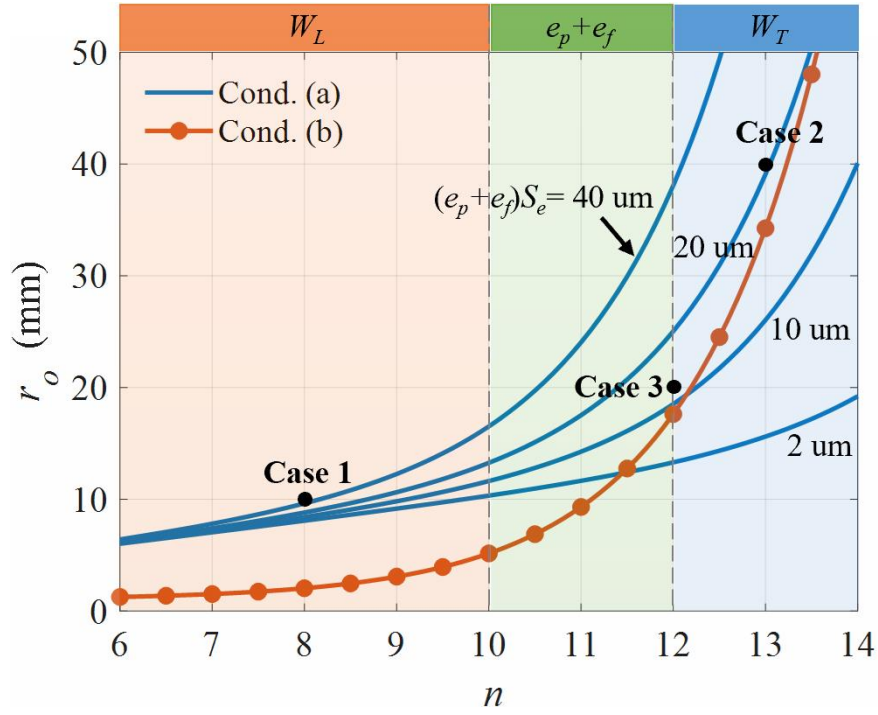


Figure 4.11 Relationship between encoding pad outer radius, r_o , and the number of encoded bits, n , at $(e_p+e_f)S_e$ equals to 2 μm , 10 μm , 20 μm , and 40 μm .

From the experiment results, we have $W_T = 8.5 \mu\text{m}$ and $W_L = 500 \mu\text{m}$. Given $\Phi = 2\pi$, $S_L = 2$, and $S_T = 3$, the relationship between r_o and n at different $(e_p+e_f)S_e$ is shown in Figure 4.11. The achievable performances combination of r_o and n are located at the region above the condition curves (a) and (b). Obtaining smaller size and higher resolution are a tradeoff in the proposed sensor designs. As for the applications that require small size ($r_o \leq 10 \text{ mm}$), the sensor's performances are mainly determined by the term, $W_L S_L n$, in Cond. (a). The requirements for alignment accuracy and transition area length are relatively low. The minimum size of the encoder is mainly determined by W_L . Case 1 is a typical point in this region, where $n = 8$ and $r_o = 10 \text{ mm}$ can be achieved with $(e_p+e_f)S_e = 40 \mu\text{m}$. As for

the applications that require high resolution ($n \geq 12$), the exponential term, $\frac{W_T S_T}{\Phi} 2^n$, dominates the tradeoff between r_o and n . The requirement for bit channel width is released. Considering current system settings, reducing the transition area length, W_T , is an efficient way to achieve high resolution in a relatively small size. Case 2 is a typical point in this region, where $n = 13$ and $r_o = 40$ mm can be achieved with $(e_p + e_f)S_e = 20$ μ m. As for the application requires both small size and high resolution ($10 \leq n \leq 12$), the sensor's performances are mainly determined by the exponential term, $\frac{(e_p + e_f)S_e}{\Phi} 2^n$. The alignment accuracy has the most important influence on the sensor's performance. Case 3 is a balanced decision-making point to obtain high resolution ($n = 12$) and small size ($r_o = 20$ mm) simultaneously.

CHAPTER FIVE

CONCLUSION

5.1 Conclusion

An MPLCI system has been proposed for fully distributed optical fiber sensing with high sensitivity and high spatial resolution. A strain resolution of better than 100 ne with a 10 cm spatial resolution has been experimentally demonstrated. The proposed system is demonstrated to interrogate the cascaded IFPI sensors along the optical fiber. And it has the potential to be used for UOG downhole pressure monitoring.

A passive all-digital sensing method is proposed for downhole pressure sensing. The downhole pressure sensor composed of helical coil Bourdon tube, gearbox, digital rotary encoder was designed, fabricated, and tested. The multiplexing module together with its surface instrument were developed and experimentally demonstrated. The fully assembled all-digital downhole sensing system was tested at both laboratory and research wellbore. The field test results match well with the theoretical value calculated from the mud weight.

Take advantages of both optical fiber and all-digital sensing technique, a fiber optic rotary encoder-based pressure sensor is presented for downhole applications. A glass additive and subtractive manufacturing system was used to fabricate the optical fiber sensing head and encoding pad with high accuracy. The prototype sensor has an SNR of 23 dB and a linear pressure response with an RMSE of 0.37. During the 400-hour high-temperature (250°C) test, the sensor's digital readings remain the same. The

reflected light intensity has a small fluctuation of about 1.5 dBm, which is ignorable compared to the digital state threshold. According to the mathematic model between fabrication requirements and sensor performances, the pressure sensitivity of $1/2^{12} \times 100\% = 0.02\%$ can be achieved with an outer radius of 20 mm. The features of high SNR, low drift, and high working temperature make the proposed sensing system suitable for downhole applications. Corporate with other types of transducers, like temperature or displacement, the sensing system can also be used to measure other physical quantities in harsh environments.

5.2 Future works

1. Assembly the multiplexing module to the main sensor and the test the multiplexed all-digital pressure sensor at production well.
2. Develop a new generation of all-digital downhole pressure sensor with minimum size.
3. Optimize the contact pins. For example, using mini bearings to replace the current bronze pins. As such the friction force of the digitizer can be reduced, and the hysteresis of the sensor can be further minimized.
4. Develop new sensor interrogation method so that the optical encoder based all-digital pressure sensor can be multiplexed.

5.3 Innovations and contributions

The innovations and contributions of the thesis are listed below.

1. A novel microwave-photonic low-coherence interferometry system has been proposed. A local unbalanced Michelson interferometer was in-line connected with the

sensing fiber to realize the low-coherence interferometry (LCI). The dark zone has been eliminated, and the requirement of the laser source was also relieved.

2. The mathematic model of the proposed MPLCI system was established. The model match well with the experiment test results.

3. The proposed MPLCI system was experimentally verified to have a strain resolution of better than 100 $\mu\epsilon$ and a spatial resolution of 10 cm.

4. A downhole pressure monitoring system based on all-digital sensing method was developed. The design, fabrication, assembly, optimization, and testing of sensor modules, including helical coil Bourdon tube, gear box, digitizer, multiplexing module, and surface instrument, were conducted. The sensor has the advantages of low cost, low drift, high working temperature, high measurement pressure, long telemetry distance, and capable of multiplexing.

5. The fully assembled all-digital downhole sensor was tested at both laboratory and research wellbore. The developed sensor worked properly at downhole with a depth of about 2550ft.

6. The proposed downhole pressure sensor uses an optical rotary encoder to convert the output of a pressure transducer to digital codes. It has the feature of high operating temperature since there are no downhole electronics and high SNR (long telemetry range) because the sensor directly transmits the digital signal.

7. Optical fiber only works as the telemetry channel, not the sensing unit. The environmental temperature influence on the optical fiber can be ignored.

8. An advanced glass additive and subtractive manufacturing (ASM) system is used to fabricate the all-glass optical fiber sensing head and the digital code on the encoding pad. The optical fiber and packaging material have a similar thermal expansion coefficient, so the fiber will still be well-sealed and fixed at elevated temperatures. The code is printed using the picosecond laser blackening technique, which features high resolution and high contrast.

9. A mathematical model to study the sensor's performance and fabrication requirements was established. The performances' tradeoffs and their limitations were discussed based on the model. The model can be used in designing and optimizing the proposed optical rotary encoder.

APPENDICES

Appendix A

Publication list

1. **Zhu, X.**, Hua, L., Lei, J., Tang, J., Murdoch, L., & Xiao, H. (2021). Microwave–photonic low-coherence interferometry for dark zone free distributed optical fiber sensing. *Optics Letters*, 46(5), 1173-1176.
2. **Zhu, X.**, Zhang, Q., Matlin, M., Chen, Y., Yang, Y., Li, T., ... & Xiao, H. (in press). All-digital Plug and Play Passive RFID Sensors for Indoor Temperature and Humidity Monitoring. 2022 IEEE Sensors.
3. **Zhu, X.**, Tang, J., Wu, J., Jiao, X., Nygaard, R., & Xiao, H. (2022, **under review**). Glass Additive and Subtractive Manufacturing of a Fiber Optic Rotary Encoder for Downhole Pressure Sensing. *IEEE Sensors Journal*.
4. Hua, L., **Zhu, X.**, DeWolf, S., Lei, J., Zhang, Q., Murdoch, L., & Xiao, H. (2020). Phase Demodulation by Frequency Chirping in Coherence Microwave Photonic Interferometry. *IEEE Journal of Selected Topics in Quantum Electronics*.
5. Hua, L., **Zhu, X.**, Cheng, B., Song, Y., Zhang, Q., Wu, Y., ... & Xiao, H. (2021). Distributed Acoustic Sensing Based on Coherent Microwave Photonics Interferometry. *Sensors*, 21(20), 6784.
6. Zhu, W., Zhang, Q., Matlin, M., Chen, Y., Wu, Y., **Zhu, X.**, ... & Xiao, H. (2020). Passive digital sensing method and its implementation on passive RFID temperature sensors. *IEEE Sensors Journal*.

7. Jiao, X., Wu, Y., **Zhu, X.**, Rahman, M., Gupta, T., Gravley D., Houston D., ... Xiao, H. (2022, in press). Distributed Coaxial Cable Sensors for in-situ Condition Based Monitoring of Coal-Fired Boiler Tubes. *39th annual international Pittsburgh coal conference*.
8. Zhang, Q., Lei, J., Hua, L., Wu, Y., **Zhu, X.**, & Xiao, H. (2020, February). Reflection-mode fiber-optic temperature sensing probe based on quantum dots filled micro-cavity. In Optical Fibers and Sensors for Medical Diagnostics and Treatment Applications XX (Vol. 11233, p. 112331F). International Society for Optics and Photonics.

REFERENCE

- [1] S. Nalley and A. LaRose, “Annual energy outlook 2022 (AEO2022),” *Energy Information Agency*, p. 23, 2022.
- [2] “Everyday Products & Uses.” <https://www.coga.org/factsheets/everyday-products-uses> (accessed Nov. 10, 2022).
- [3] “Unconventional oil - Wikipedia.” https://en.wikipedia.org/wiki/Unconventional_oil (accessed Nov. 10, 2022).
- [4] “Tight oil - Wikipedia.” https://en.wikipedia.org/wiki/Tight_oil (accessed Nov. 10, 2022).
- [5] “Independent Petroleum Association of America | Hydraulic Fracturing.” <https://www.ipaa.org/fracking/#studies> (accessed Nov. 10, 2022).
- [6] L. Weijers, C. Wright, M. Mayerhofer, M. Pearson, L. Griffin, and P. Weddle, “Trends in the North American frac industry: Invention through the shale revolution,” in *SPE Hydraulic Fracturing Technology Conference and Exhibition*, 2019.
- [7] J. Burwen and J. Flegal, “Case studies on the government’s role in energy technology innovation: unconventional gas exploration & production,” 2013.
- [8] “DOE/NETL funding opportunity announcement, DE-FOA-0001990: Advanced Technologies for Recovery of Unconventional Oil and Gas Resources,” 2018.

- [9] J. v Herwanger*, A. D. Bottrill, and S. D. Mildren, “Uses and abuses of the brittleness index with applications to hydraulic stimulation,” in *Unconventional Resources Technology Conference, San Antonio, Texas, 20-22 July 2015*, 2015, pp. 1215–1223.
- [10] J. Xu and S. Sonnenberg, “Brittleness and rock strength of the Bakken formation, Williston basin, North Dakota,” in *SPE/AAPG/SEG Unconventional Resources Technology Conference*, 2016.
- [11] T. Wilson *et al.*, “Relationships of $\lambda\rho$, $\mu\rho$, brittleness index, Young’s modulus, Poisson’s ratio, and high total organic carbon for the Marcellus Shale, Morgantown, West Virginia,” in *2017 SEG International Exposition and Annual Meeting*, 2017.
- [12] X. Zhang, Y. Lu, J. Tang, Z. Zhou, and Y. Liao, “Experimental study on fracture initiation and propagation in shale using supercritical carbon dioxide fracturing,” *Fuel*, vol. 190, pp. 370–378, 2017.
- [13] A. Ghanizadeh *et al.*, “Controls on liquid hydrocarbon permeability of tight oil and liquid-rich gas reservoirs: Examples from Bakken and Montney formations (Canada),” in *Unconventional Resources Technology Conference, Houston, Texas, 23-25 July 2018*, 2018, pp. 3316–3341.
- [14] J. Ramos, W. Wang, M. S. Bruno, K. Lao, and N. Oliver, “Development and Testing of Advanced Inter-Well Pressure Pulse Analysis for Fracture Diagnostics in Tight Gas Reservoirs,” in *52nd US Rock Mechanics/Geomechanics Symposium*, 2018.

- [15] Y. Li and Y. Han, “Decline curve analysis for production forecasting based on machine learning,” in *SPE Symposium: Production Enhancement and Cost Optimisation*, 2017.
- [16] D. Yang, T. Denney, O. Bello, S. Lazarus, and C. Vettical, “Enabling Real-Time Distributed Sensor Data for Broader Use by the Big Data Infrastructures,” in *SPE Intelligent Energy International Conference and Exhibition*, 2016.
- [17] S. Wodin-Schwartz, M. W. Chan, K. R. Mansukhani, A. P. Pisano, and D. G. Senesky, “MEMS sensors for down-hole monitoring of geothermal energy systems,” *Energy Sustainability*, vol. 54686, pp. 965–972, 2011.
- [18] B. W. Abegaz, T. Datta, and S. M. Mahajan, “Sensor technologies for the energy-water nexus—A review,” *Appl Energy*, vol. 210, pp. 451–466, 2018.
- [19] I. Ahmad *et al.*, “Reliable technology for drilling operations in a high-pressure/high-temperature environment,” in *IADC/SPE Drilling Conference and Exhibition*, 2014.
- [20] L. Zheng, Y. U. Jiaqing, Y. Qinghai, G. Yang, and S. Fuchao, “Vibration wave downhole communication technique,” *Petroleum Exploration and Development*, vol. 44, no. 2, pp. 321–327, 2017.
- [21] N. G. Franconi, A. P. Bungler, E. Sejdić, and M. H. Mickle, “Wireless communication in oil and gas wells,” *Energy Technology*, vol. 2, no. 12, pp. 996–1005, 2014.

- [22] R. Mijarez-Castro, H. J. Rodríguez-Rodríguez, D. Pascasio-Maldonado, and R. Guevara-Gordillo, “Communications system for down-hole measurements,” *Journal of applied research and technology*, vol. 11, no. 6, pp. 903–911, 2013.
- [23] R. Nygaard, S. Salehi, B. Weideman, and R. G. Lavoie, “Effect of dynamic loading on wellbore leakage for the wabamun area CO₂-sequestration project,” *Journal of Canadian Petroleum Technology*, vol. 53, no. 01, pp. 69–82, 2014.
- [24] U. S. S. Gas and S. O. Plays, “Review of Emerging Resources,” 2011.
- [25] T. Reinsch and J. Henningsen, “Temperature-dependent characterization of optical fibres for distributed temperature sensing in hot geothermal wells,” *Meas Sci Technol*, vol. 21, no. 9, p. 094022, 2010.
- [26] H.-D. Ngo, B. Mukhopadhyay, O. Ehrmann, and K.-D. Lang, “Advanced liquid-free, piezoresistive, SOI-based pressure sensors for measurements in harsh environments,” *Sensors*, vol. 15, no. 8, pp. 20305–20315, 2015.
- [27] E. Chan, D. Lin, L. Lu, H. L. Chau, and M. Wong, “Trench-isolated bulk-type pressure sensor on silicon-on-insulator for high-temperature and high-pressure downhole applications,” in *2018 Solid-State Sensors, Actuators and Microsystems Workshop, Hilton Head 2018*, 2018.
- [28] H.-D. Ngo, O. Ehrmann, M. Schneider-Ramelow, and K.-D. Lang, “Piezoresistive Pressure Sensors for Applications in Harsh Environments—A Roadmap,” in *Modern Sensing Technologies*, Springer, 2019, pp. 231–251.
- [29] E. P. EerNisse, “Quartz resonators vs their environment: Time base or sensor?,” *Jpn J Appl Phys*, vol. 40, no. 5S, p. 3479, 2001.

- [30] S. M. M. Quintero, S. W. O. Figueiredo, V. L. Takahashi, R. A. W. Llerena, and A. M. B. Braga, "Passive downhole pressure sensor based on surface acoustic wave technology," *Sensors*, vol. 17, no. 7, p. 1635, 2017.
- [31] E. H. Holley and N. Kalia, "Fiber-optic monitoring: Stimulation results from unconventional reservoirs," in *Unconventional Resources Technology Conference, San Antonio, Texas, 20-22 July 2015*, 2015, pp. 300–315.
- [32] L. Schenato, "A review of distributed fibre optic sensors for geo-hydrological applications," *Applied Sciences*, vol. 7, no. 9, p. 896, 2017.
- [33] X. Zhou, Q. Yu, and W. Peng, "Fiber-optic Fabry–Perot pressure sensor for downhole application," *Opt Lasers Eng*, vol. 121, pp. 289–299, 2019.
- [34] P. M. Nellen *et al.*, "Reliability of fiber Bragg grating based sensors for downhole applications," *Sens Actuators A Phys*, vol. 103, no. 3, pp. 364–376, 2003.
- [35] Z. Liu, L. Htein, K.-K. Lee, K.-T. Lau, and H.-Y. Tam, "Large dynamic range pressure sensor based on two semicircle-holes microstructured fiber," *Sci Rep*, vol. 8, no. 1, pp. 1–9, 2018.
- [36] X. Li, H. Zhang, C. Qian, Y. Ou, R. Shen, and H. Xiao, "A new type of structure of optical fiber pressure sensor based on polarization modulation," *Opt Lasers Eng*, vol. 130, p. 106095, 2020.
- [37] H. Y. Fu *et al.*, "Pressure sensor realized with polarization-maintaining photonic crystal fiber-based Sagnac interferometer," *Appl Opt*, vol. 47, no. 15, pp. 2835–2839, 2008.

- [38] Z. N. Wang *et al.*, “Ultra-long phase-sensitive OTDR with hybrid distributed amplification,” *Opt Lett*, vol. 39, no. 20, p. 5866, 2014, doi: 10.1364/ol.39.005866.
- [39] S. Liehr, S. Münzenberger, and K. Krebber, “Wavelength-scanning coherent OTDR for dynamic high strain resolution sensing,” *Opt Express*, vol. 26, no. 8, p. 10573, 2018, doi: 10.1364/OE.26.010573.
- [40] H. F. Martins, K. Shi, B. C. Thomsen, S. Martin-Lopez, M. Gonzalez-Herraez, and S. J. Savory, “Real time dynamic strain monitoring of optical links using the backreflection of live PSK data,” *Opt Express*, vol. 24, no. 19, p. 22303, 2016, doi: 10.1364/oe.24.022303.
- [41] B. Lu *et al.*, “High spatial resolution phase-sensitive optical time domain reflectometer with a frequency-swept pulse,” *Opt Lett*, vol. 42, no. 3, p. 391, 2017, doi: 10.1364/ol.42.000391.
- [42] F. Calliari, M. M. Correia, G. P. Temporao, G. C. Amaral, and J. P. von der Weid, “Fast Acquisition Tunable High-Resolution Photon-Counting OTDR,” *Journal of Lightwave Technology*, vol. 8724, no. c, pp. 1–1, 2020, doi: 10.1109/jlt.2020.2990872.
- [43] J. Li *et al.*, “High spatial resolution distributed fiber strain sensor based on phase-OFDR,” *Opt Express*, vol. 25, no. 22, p. 27913, 2017, doi: 10.1364/oe.25.027913.
- [44] D. Chen, Q. Liu, and Z. He, “High-fidelity distributed fiber-optic acoustic sensor with fading noise suppressed and sub-meter spatial resolution,” *Opt Express*, vol. 26, no. 13, p. 16138, 2018, doi: 10.1364/oe.26.016138.

- [45] H. Li, Q. Liu, D. Chen, Y. Deng, and Z. He, “High-spatial-resolution fiber-optic distributed acoustic sensor based on Φ -OFDR with enhanced crosstalk suppression,” *Opt Lett*, vol. 45, no. 2, p. 563, 2020, doi: 10.1364/ol.380442.
- [46] J. Clement, H. Maestre, G. Torregrosa, and C. R. Fernández-Pousa, “Incoherent optical frequency-domain reflectometry based on homodyne electro-optic downconversion for fiber-optic sensor interrogation,” *Sensors (Switzerland)*, vol. 19, no. 9, 2019, doi: 10.3390/s19092075.
- [47] S. Liehr, N. Nöther, and K. Krebber, “Incoherent optical frequency domain reflectometry and distributed strain detection in polymer optical fibers,” *Meas Sci Technol*, vol. 21, no. 1, 2010, doi: 10.1088/0957-0233/21/1/017001.
- [48] S. Werzinger, D. Zibar, M. Köppel, and B. Schmauss, “Model-based position and reflectivity estimation of fiber bragg grating sensor arrays,” *Sensors (Switzerland)*, vol. 18, no. 7, pp. 1–22, 2018, doi: 10.3390/s18072268.
- [49] J. Wang *et al.*, “Interrogation of a large-capacity densely spaced fiber Bragg grating array using chaos-based incoherent-optical frequency domain reflectometry,” *Opt Lett*, vol. 44, no. 21, p. 5202, 2019, doi: 10.1364/ol.44.005202.
- [50] T. Kissinger, E. Chehura, S. E. Staines, S. W. James, and R. P. Tatam, “Dynamic Fiber-Optic Shape Sensing Using Fiber Segment Interferometry,” *Journal of Lightwave Technology*, vol. 36, no. 4, pp. 917–925, 2018, doi: 10.1109/JLT.2017.2750759.

- [51] J. Huang, X. Lan, M. Luo, and H. Xiao, “Spatially continuous distributed fiber optic sensing using optical carrier based microwave interferometry,” *Opt Express*, vol. 22, no. 15, p. 18757, 2014, doi: 10.1364/oe.22.018757.
- [52] L. Hua *et al.*, “Coherence-length-gated distributed optical fiber sensing based on microwave-photonic interferometry,” *Opt Express*, vol. 25, no. 25, pp. 31362–31376, 2017.
- [53] L. Hua *et al.*, “Phase demodulation by Frequency Chirping in Coherence Microwave Photonic Interferometry,” *IEEE Journal of Selected Topics in Quantum Electronics*, no. c, pp. 1–1, 2020, doi: 10.1109/jstqe.2020.2975575.
- [54] Y. J. Rao and D. A. Jackson, “Recent progress in fibre optic low-coherence interferometry,” *Meas Sci Technol*, vol. 7, no. 7, pp. 981–999, 1996, doi: 10.1088/0957-0233/7/7/001.
- [55] Y. Song *et al.*, “An IFPI Temperature Sensor Fabricated in an Unstriped Optical Fiber with Self-Strain-Compensation Function,” *J Sens*, vol. 2016, 2016, doi: 10.1155/2016/6419623.
- [56] Z. Chen, G. Heffernan, L. Yuan, Y. Song, and T. Wei, “Ultraweak Waveguide Modification with Intact Buffer Coating Using Femtosecond Laser Pulses,” *IEEE Photonics Technology Letters*, vol. 27, no. 16, pp. 1705–1708, 2015, doi: 10.1109/LPT.2015.2438078.

- [57] A. M. Rollins and J. A. Izatt, “SNR analysis of conventional and optimal fiber optic low-coherence interferometer topologies,” *Coherence Domain Optical Methods in Biomedical Science and Clinical Applications IV*, vol. 3915, no. April 2000, p. 60, 2000, doi: 10.1117/12.384175.
- [58] F. P. Beer, E. R. Johnston, J. T. DeWolf, and D. F. Mazurek, *Mechanics of Materials (Sixth Edition)*. 2012.
- [59] V. F. Bense *et al.*, “Distributed Temperature Sensing as a downhole tool in hydrogeology,” *Water Resour Res*, vol. 52, no. 12, pp. 9259–9273, 2016.
- [60] Q. Zhao *et al.*, “Adhesive-free bonding fiber optic Fabry–Perot pressure sensor based on oxy-hydrogen flame welding and spiral tube,” *Opt Commun*, vol. 476, p. 126307, 2020.
- [61] S. H. Aref, M. I. Zibaii, and H. Latifi, “An improved fiber optic pressure and temperature sensor for downhole application,” *Meas Sci Technol*, vol. 20, no. 3, p. 34009, 2009.
- [62] K. Chen, X. Zhou, B. Yang, W. Peng, and Q. Yu, “A hybrid fiber-optic sensing system for down-hole pressure and distributed temperature measurements,” *Opt Laser Technol*, vol. 73, pp. 82–87, 2015.
- [63] H. Y. Fu *et al.*, “High pressure sensor based on photonic crystal fiber for downhole application,” *Appl Opt*, vol. 49, no. 14, pp. 2639–2643, 2010.
- [64] J. Wang, X. Fu, H. Gao, X. Gui, H. Wang, and Z. Li, “FPGA-Based Dynamic Wavelength Interrogation System for Thousands of Identical FBG Sensors,” in *Photonics*, 2022, vol. 9, no. 2, p. 79.

- [65] W. Zhu *et al.*, “Passive digital sensing method and its implementation on passive RFID temperature sensors,” *IEEE Sens J*, vol. 21, no. 4, pp. 4793–4800, 2020.
- [66] J. Lei, Y. Hong, Q. Zhang, F. Peng, and H. Xiao, “Additive manufacturing of fused silica glass using direct laser melting,” in *CLEO: Applications and Technology*, 2019, pp. AW3I-4.
- [67] Q. Zhang *et al.*, “Information integrated glass module fabricated by integrated additive and subtractive manufacturing,” *Opt Lett*, vol. 45, no. 7, pp. 1663–1666, 2020.
- [68] Q. Zhang, J. Lei, Y. Chen, Y. Wu, C. Chen, and H. Xiao, “3D printing of all-glass fiber-optic pressure sensor for high temperature applications,” *IEEE Sens J*, vol. 19, no. 23, pp. 11242–11246, 2019.
- [69] Q. Zhang, J. Lei, Y. Chen, Y. Wu, and H. Xiao, “Glass 3D printing of microfluidic pressure sensor interrogated by fiber-optic refractometry,” *IEEE Photonics Technology Letters*, vol. 32, no. 7, pp. 414–417, 2020.
- [70] H. Huang, L.-M. Yang, S. Bai, and J. Liu, “Blackening of metals using femtosecond fiber laser,” *Appl Opt*, vol. 54, no. 2, pp. 324–333, 2015.
- [71] B. Liu *et al.*, “Porous microstructures induced by picosecond laser scanning irradiation on stainless steel surface,” *Opt Lasers Eng*, vol. 78, pp. 55–63, 2016.
- [72] J. Lei *et al.*, “Laser-assisted embedding of all-glass optical fiber sensors into bulk ceramics for high-temperature applications,” *Opt Laser Technol*, vol. 128, p. 106223, 2020.

- [73] J. Lei *et al.*, “One-Step Fabrication of Nanocrystalline Nanonetwork SnO₂ Gas Sensors by Integrated Multilaser Processing,” *Adv Mater Technol*, vol. 5, no. 8, p. 2000281, 2020.